

INTERFEROMETRIC OPTICAL FIBRE SENSOR FOR HIGHWAY PAVEMENTS AND CIVIL STRUCTURES

A Thesis submitted

by

SACHIN RAMCHANDRA SURVE

For the degree of

DOCTOR OF PHILOSOPHY



Optical Technology Research Laboratory
School of Electrical Engineering

VICTORIA UNIVERSITY OF TECHNOLOGY

2003

FTS THESIS
681.25 SUR
30001007903695
Surve, Sachin Ramchandra
Interferometric optical
fibre sensor for highway
pavements and civil



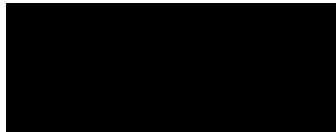
आक्का व आजोबा
यांना समर्पित

DECLARATION

I, Sachin Ramchandra Surve, declare that the thesis entitled,

“Interferometric optical fibre sensor for highway pavements and civil structures”

is my own work and has not been submitted previously, in whole or in part, in respect of any other academic award.



Sachin R. Surve
Date: August 29, 2003

ACKNOWLEDGMENTS

I firstly would like to thank Prof. David Booth and the Department of Applied Physics for providing me a scholarship.

I would like to thank my supervisors Dr. Andrew Stevenson and Associate Prof. Stephen Collins for their valuable guidance during this research. I am very grateful to Future Fibre Technologies Pty. Ltd. (FFT) and Australian Road Research Board (ARRB) for providing sensor installation facilities.

I am very grateful to Mr. Vincent Rouillard and Mr. Laszlo Kovacs for providing the sensor testing facility. I also would like to thank Associate Prof. Peter Farrell, Associate Prof. Gregory Baxter Mr. Robert Taylor and Dr. Anthony Ash for their assistance in proof reading and valuable discussions during the final months.

Of the technical staff, I would like to thank Mr. Alex Shelamoff, Mr. Hayrettin Arisoy and Mr. Abdurrahman Kuzucu for their helpful assistance with the design of electronic apparatus. From the mechanical workshop, I would like to thank Mr. Donald Ermel for his useful consultation and construction of necessary equipment.

I wish to express my appreciation for my friends Dr. Valentin Bogdanov, Dr. Darol Garchev, Dr. Ian Mitchell, Ms Cristina Vergara, Mr. Selvarajah Sathiyakumar, Mrs. Nicoleta Dragomir, Ms. Corinna Sullivan, Mr. Thinh Nguyen, Dr. Mikhail Vasiliev and the Administrative Officer Ms. Maria Benka for their timely help.

My sincerest thanks to Mr. Sanjeev Matkar, Mrs. Preeti Matkar, Mr. Alban Pereira, Mrs. Brenda Pereira, Mr. Giuliano Ardis, Mrs. Giliola Ardis, Mr. Armando Aprile and Mrs. Maria Aprile for their moral support during the hard times of this project.

I would like to thank from the bottom of my heart to my father, Mr. Ramchandra R. Surve and mother, Mrs. Suhasini R. Surve who provided me the opportunity to continue my academic studies. Lastly, I wish to express my truthful regards to my wife, Bharati and my daughter, Sayalee for all help, love and patience.

ABSTRACT

Optical fibres have been used for developing variety of sensing configurations for monitoring a wide range of parameters. This thesis presents the design, construction and characterisation of a new type of single-transducer optical fibre Weigh-In-Motion (WIM) sensor. The sensor is based on an extended (long) fibre optic Fabry-Pérot interferometer. The Fabry-Pérot arrangement was chosen for its simplicity, sensitivity, low cost and ease of installation.

A Fabry-Pérot interferometer with sensing length of 300 mm was constructed using an in-fibre Bragg grating as a launching end reflector and gold coating as a far end reflector. The sensing length was configured to operate in the reflection mode. The laboratory characterisation of this system was carried out by embedding the sensing element into an aluminium beam and subjecting it to a variety of periodic central deformation functions, such as sinusoidal and triangular using a non-destructive structural testing machine. The sensor performance was assessed under a controlled environment and the system was analyzed for its repeatability, sensitivity, accuracy, linearity and dynamic sensing limitations.

The viability of this configuration for WIM applications was investigated by installing 4 m long sensors under highway pavements and comparing the sensor outputs with vehicular loads recorded by commercially available WIM system, CULWAY.

This vehicle induced lateral distortion in the pavement-sublayer stretches the embedded sensing segment and produces optical phase shifts in the sensing fibre. The sensor outputs optical phase shifts in terms of intensity modulations known as interferometric fringes. This sensor responds to changes in the strain fields of the pavement sublayers, rather than absolute axle loads. Thus to a gross level, the overall fringe counts are linearly proportional with the aggregate axle load for each vehicle.

This single-transducer fibre optic WIM sensor is capable of estimating truck weights within error margins of 10 to 15% for all types of axle configurations. Systematic errors arise in the “fringe-per-tonne” calibration factor due to the variety of axle configurations. A method of correcting the gross fringe counts based on the differences in the FFPI response to the pavement compression and relaxation is discussed and offers the potential of reducing these uncertainties to ~ 6 to 8%.

This performance is comparable to other commercially available fibre and non-fibre WIM systems based on a single-transducer design. However, this sensor is simple to fabricate, easy to install, and economic for mass production. This preliminary study shows its potential for WIM sensing. Also, additional investigation of the responses of single-transducer and multiple-transducer sensor configurations embedded into pavements and other structures would reveal suitability of this system for other generic applications.

TABLE OF CONTENTS

DECLARATION	II
ACKNOWLEDGMENTS	III
ABSTRACT	IV
TABLE OF CONTENTS	VI
CHAPTER 1 INTRODUCTION	1
1.1 Motivation	2
1.2 Aims and Objectives	5
1.3 Overview of Thesis	6
CHAPTER 2 OPTICAL FIBRES FOR WEIGH-IN-MOTION: A REVIEW	9
2.1. Introduction	10
2.2. Fibre Optic Sensing Technology	10
2.2.1. Advantages of Optical Fibres for Sensing Technology	11
2.2.2. Optical Fibres for Structural Sensing Applications	12
2.2.3. Optical Fibre Sensing Configurations	14
2.3. Interferometers	16
2.3.1. Bulk Optic Interferometers	16
2.3.2. Multiple Beam Configurations	18
2.3.3. Two Beam Configurations	19
2.3.4. Phase Shift Detection Methods	21
2.3.5. Fibre Fabry-Pérot Interferometer (FFPI) Construction	22
2.3.6. FFPI Theory	24
2.4. In-Fibre Bragg Gratings (IFBG)	28
2.4.1. Introduction	28
2.4.2. Writing Mechanism	29
2.4.3. Fabrication Technology – A Review	29

2.5.	Weigh-In-Motion (WIM) Technology	31
2.5.1.	Introduction to WIM Sensing	31
2.5.2.	Classification of WIM Sensors	32
2.5.3.	WIM Accuracy Limitations based on Pavement and Vehicle Dynamics	33
2.5.4.	Capabilities of Conventional WIM Technology	34
2.6.	Review of Existing Fibre Optic WIM Technology	35
2.6.1.	Polarisation based Fibre Optic WIM Sensors	36
2.6.2.	Interferometric Fibre Optic WIM Sensors	37
2.6.3.	Fibre Optic WIM Sensors based on Speckle Pattern Analysis	37
2.7.	Summary	38
CHAPTER 3	DEVELOPMENT OF FIBRE FABRY-PÉROT SINGLE-TRANSDUCER WEIGH-IN-MOTION SYSTEM	40
3.1.	Introduction	41
3.2.	Theoretical Strain Transfer Function	41
3.3.	Source Considerations	45
3.4.	Sensing Configuration	47
3.5.	Optimisation of FFPI Output	49
3.6.	IFBG Fabrication	54
3.7.	Estimation of the Sensor Output	58
3.7.1	Fringe Count Estimation based on the Bending Mechanism	58
3.7.2	Effect of Loading Trends on the Sensor Output	60
3.7.3	Pavement-Vehicle Dynamics	62
3.7.4	Fringe Count Estimation based on Pavement Response	63
3.7.5	Fringe Frequency Estimation	68
3.7.6	Method of Calculating Fringe Frequency	71
3.8.	Summary	73

CHAPTER 4	LABORATORY SENSOR: DESIGN, CONSTRUCTION AND CHARACTERISATION	75
4.1	Introduction	76
4.2	Sensor Design	77
4.2.1	Transducer Construction and Sensor Assembly	79
4.2.2	Laser Source	78
4.2.3	Detector Circuit	81
4.3	Software Development	83
4.3.1	Introduction	83
4.3.2	Explanation of the Method	85
4.3.3	Instantaneous Fringe Frequency Calculations	87
4.3.4	Limitations	88
4.4	Sensor Characterisation	89
4.4.1	Test System Description	89
4.4.2	Calibration	91
4.4.3	Sensor Repeatability and Linearity	97
4.4.4	Effect of Sinusoidal and Triangular Deformation Profiles on the Output Fringe Patterns	101
4.4.5	Estimation of Applied Deformation Profile using Fringe Frequency	103
4.4.6	Strain Sensing Limitations of the Laboratory Experiments	107
4.5	Summary	109
CHAPTER 5	RESULTS AND DISCUSSION	110
5.1	Introduction	111
5.2	CULWAY System Verification	112
5.2.1	Introduction	112
5.2.2	Analysis of CULWAY Reliability	113
5.3	Field Sensor Installations	114
5.4	Error Sources	116
5.4.1	Effect of Change in Poisson's Ratio on Total Fringe Counts	117
5.4.2	Fringe Frequency Noise	119

5.4.3	Amplitude Noise	121
5.5	Assessing Viability for WIM Sensing	122
5.5.1	Output Fringe Patterns	122
5.5.2	Formation of Fringe Groups	125
5.5.3	FFPI Calibration using CULWAY Sensor	128
5.5.4	Tests of Repeatability of FFPI Calibration Procedure	131
5.5.5	FFPI Calibration using EMU Sensor	134
5.5.6	Analysis of the FFPI Calibration based on the Axle Configurations	137
5.6	Analysis of Single Axle Pavement Deformation Function	138
5.6.1	Introduction	138
5.6.2	Method for Estimating a Single-Axle Pavement Deformation Function	140
5.6.3	Estimation of the Type of Single-Axle Pavement Deformation Function	142
5.7	Estimation of Fringe Count Errors based on Axle Separations and Loading Trends	143
5.7.1	Load Distribution of 1-2-3 Axle Configuration	143
5.7.2	Matrix Method for Compensating Axle-Group Dependent Calibration Factor	147
5.7.3	Fringe Count Correction	149
5.8	Summary	155
CHAPTER 6	CONCLUSIONS AND FUTURE DIRECTIONS	157
6.1	Conclusions	158
6.1.1	Introduction	158
6.1.2	Monitoring Dynamic Structural Strains	158
6.1.3	Viability for WIM Sensing	159
6.1.4	Estimation of Pavement Deformation Profile	160
6.2	Future Directions	161
6.2.1.	Multiple Transducer FFPI WIM System	161

REFERENCES	162
PUBLICATION	178
LIST OF SYMBOLS	179

CHAPTER 1

INTRODUCTION

1.1 Motivation

The increasing reliance by national economies around the world on road-based heavy freight transportation has spurred the development of ground-breaking technologies for road, vehicle and traffic management systems¹⁻⁴. Various internationally coordinated efforts, such as 'WAVE' (Weigh-in-motion of Axles and Vehicles for Europe)⁵ and COST323 (European Co-operation in the Field of Scientific and Technical Research)⁶ undertaken by CORDIS (Community Research and Development Information Service), are developing integrated and “intelligent” freight transport networks. The new technologies, such as systems for weighing vehicles in motion (Weigh-In-Motion), automatic traffic monitoring, real-time assessment of damage to pavement and road infrastructure, law enforcement and safety, may lead to appropriate cost recovery from heavy transportation.

This thesis addresses particular applications of optical fibre strain sensing technology which may play a critical role in implementing these new “intelligent” transportation systems. In particular, this investigation seeks to evaluate the viability and applicability of a single-transducer fibre optic Fabry-Pérot sensor in two specific applications expected to be of prime importance in intelligent highway systems:

(a) Weigh-In-Motion (WIM) sensing - The real-time automated measurement of the weight of a vehicle travelling at various speeds (75– 100 km/h) along a section of carriageway overlying the sensor. This approach contrasts with cumbersome and labour-intensive static vehicular weighing systems such as weigh-bridges and wheel-pads, which currently dominate vehicular testing sites.

(b) Embedded strain sensing - The use of fibre optic sensors strategically placed within large civil structures such as highway bridges, tunnels and road pavements to monitor their physical state in real-time. This is expected to provide significant safety, economic and engineering advantages over current approaches such as periodic visual inspection and external mechanical testing.

WIM sensors may also find applications elsewhere in the transport industry. WIM data helps to estimate traffic loads on pavements (e.g. tonnes/day)⁷, design pavements⁸ and analyse the role of dynamic forces in road damage mechanisms^{9,10}. In various geographical regions, WIM research facilitates the creation of appropriate transport policies to manage the performance of highway systems¹¹, regulate the design of vehicles and permissible loads¹² and implement safety¹³ and legal¹⁴ standards.

WIM sensors have been available in one form or another for approximately 30 years. Most currently available WIM systems operate automatically and return instantaneous vehicular data collected either by surface-mounted or embedded transducers within the road structures. They have the ability to provide information regarding axle configuration, axle group weights, vehicle speed and the weight of moving vehicles. The majority of WIM sensors rely on electrical transducers, which experience problems inherent in most electrical sensors, such as susceptibility to humidity and water, corrosion, electromagnetic interference and resistance losses due to long cable lengths. For these reasons, and because of advances in optical fibre technology in recent years¹⁵, several studies¹⁶⁻¹⁸ have recognised that optical fibre WIM sensors may perform better than electrical WIM sensors, both economically (installation, reliability and maintenance) and physically (sensitivity, accuracy, precision and consistency). Therefore the current project adopts this novel approach of using an optical fibre sensing configuration for WIM applications.

All WIM systems, except those employing surface-mounted transducers, monitor vehicle-induced changes in pavement materials using transducers embedded into the pavement infrastructure. Embedded transducers are a key enabling technology that permits the development of advanced traffic monitoring systems and other structural sensing applications. Structural sensing is an important technology in its own right with significant benefits in the transport arena; for example, early warning of internal damage to a bridge or tunnel is possible by appropriate instrumentation¹⁹⁻²¹. Economic benefits are gained by reducing the frequency of detailed periodic inspections of these structures. For example, in the USA, there are presently over

four million highway bridges that require periodic inspection²². Remote and automated monitoring systems will reduce the enormous amount of resources required for examining structural integrity. This research will also assist others who employ embedded sensing technology to instrument large deformable civil and mechanical structures such as bridges, aircraft and buildings.

An embedded sensor can also return useful indirect measurements of other parameters, such as temperature or strain, that affect the host structure. In other words, embedded sensors provide certain “intelligence” to the structure and allow detection of any structural variations. Prevention of non-restorable structural damage is possible by applying an equivalent force to oppose the induced variations. This counteractive force can be generated with the help of an appropriate sensor-actuator feedback mechanism. These structures can react to the applied perturbations and are known as "Smart Structures"²³⁻²⁶. The embedded WIM sensor developed during this study has gathered information about pavement deformations. The same sensor may also be utilised to acquire data related to deformations in other structures.

In all dynamic sensing systems, including the systems to be evaluated in this project, the issue of dynamic *calibration* is of significant interest to researchers^{10,27}. Unlike static vehicular weight sensors, which are calibrated regularly with static weights, WIM sensors respond differently to the same gross vehicular weight under different dynamic loading conditions. The main reason is that most WIM sensors, including those in this project, are embedded in road sublayers so that the pavement, compacted clay and gravel are integral components of the transducer. One important consequence of this is that the sublayer deformations due to each axle extend for some distance in front of, and behind the axle, depending on installation depth, so that the embedded sensing element interacts with multiple axles simultaneously as they pass over the sensor. For this reason alone, even in the absence of other nonlinear or inelastic pavement characteristics, this device is likely to be sensitive to variations in axle load configurations, vehicular speeds, tyre and suspension characteristics, vehicle bouncing, and sub-pavement conditions near the sensor element. These characteristics complicate the task of sensor calibration and have the

potential to impact negatively on the repeatability of the sensor and hence the accuracy of its calibration.

Since optical fibre WIM sensing is a gradually developing technology, investigations of interactions between various pavement materials, dynamic forces and transducer configurations are required. A full understanding of new sensors will aid in the design and installation of future WIM systems, both electrical and optical. Therefore, the design, construction and characterisation of a new type of optical fibre WIM sensing system are of interest.

1.2 Aims and Objectives

In this project, the primary aim is to design and construct a single-transducer fibre optic sensor, and assess its viability and applicability for Weigh-in-Motion applications. These aims required investigation of each of the following issues and objectives.

(a) Sensor Design and Construction

The present research adopts a well-studied interferometric configuration - the Fibre Fabry-Pérot Interferometer.

- Literature review of WIM and optical fibre sensors.
- Review of Fibre Fabry-Pérot Interferometer (FFPI) configurations.
- Fabrication of the FFPI.
- Construction of the sensing element.
- Assembly of optical to electrical conversion circuitry.
- Automation of the sensor and design of data analysis software.

(b) Intrinsic Performance and Limitations of the Sensor

This stage of the research assessed the viability of the sensor under controlled laboratory conditions.

- Embedding of the sensing element into a test structure (aluminium beam).

- Design and perform a series of experiments in the laboratory using a universal testing machine.
- Assessment of the potential of the sensor for structural sensing applications.

(c) Performance and Calibration of Fibre Optic WIM Sensors

This phase of the research assessed the viability of the sensor for WIM applications.

- Modification of the sensing system for field trials.
- Installation of the sensor into pavement structures.
- Recording of truck data.
- Calibration of the sensor.
- Estimation of the pavement response.

1.3 Overview of the Thesis

This project involves study of various technologies such as optical fibre sensors, in-fibre Bragg grating fabrication processes, conventional weigh-in-motion configurations, newly-evolved fibre optic weigh-in-motion systems and pavement dynamics.

The proposed sensing system employs a fibre Fabry-Pérot sensing configuration in reflection mode. The background literature of optical fibre sensing technology and a theoretical overview of fibre Fabry-Pérot interferometers is described in Chapter 2. Commercial WIM sensing techniques, their performance and emerging optical fibre technology for WIM are also described. The intrinsic optical Fabry-Pérot cavity was constructed by fabricating an in-fibre Bragg grating at the launching-end and a metal coating at the far-end of an optical fibre. A brief review of various fabrication processes for writing in-fibre Bragg gratings is also presented. The reflectivities of the fibre grating and the mirror were specially chosen, on the basis of a Fourier analysis described in Chapter 2, so that the Fabry-Pérot interferometer would produce quasi-sinusoidal output fringes with maximal amplitude of the fundamental harmonic.

The gratings employed during this project were fabricated using a prism interferometry technique (Chapter 3). The optical output obtained from the sensor was converted to an electrical signal using a photodiode circuit including a transimpedance amplifier and filtering components. Sensor theory and estimation of the total fringe counts have also been discussed.

The sensor data were collected using a general purpose PC data acquisition card and was processed and saved by a dedicated program written in National Instrument's LabView 4.1. The construction details of the laboratory and field sensing systems were discussed in Chapter 4. This chapter also explains the theoretical sensor behaviour of the laboratory and field versions.

An optical fibre Fabry-Pérot strain sensor was embedded into an aluminium beam structure which was subjected to lateral bending with controlled waveforms using an Instron 8501 Universal Testing Machine. By monitoring the sensor output under different deformations, the frequency limitations, linearity and repeatability were mapped over a useful operating range. From this information, an assessment of the viability of this sensor has been made for general embedded structural sensing (described in Chapter 4).

Optical fibre Fabry-Pérot strain sensors were embedded in the sub-pavement layers beneath a single traffic lane of a highway, enabling the outputs to be monitored as heavy vehicles passed over the sensing region. The field version of the sensing system was calibrated by comparing its output with commercially available WIM systems such as CULWAY²⁸ and static weight bridge Electronic Mass Unit (EMU). Primarily, performance aspects such as linearity and repeatability were assessed. Investigation of the non-linear calibration artefacts that depend on axle configuration, arising in the response of a distributed pavement to applied loads is also of importance (Chapter 5).

The major outcomes of this project, the concluding remarks and future directions are presented in Chapter 6. The proposed WIM system is based on a single sensing element (single-transducer). It is possible to construct a system with multiple sensing

elements (multiple-transducer) that averages the errors due to vehicle bouncing and improve the sensor accuracy. In this concluding chapter, the multiplexing scheme for two or more sensing elements is proposed as future work.

CHAPTER – 2

**OPTICAL FIBRES
FOR
WEIGH-IN-MOTION:
A REVIEW**

2.1. Introduction

Given the numerous advantages and inherent adaptability of fibre optic sensors, it is logical to use fibre optic technology in the development of weigh-in-motion (WIM) sensors. Surprisingly, perhaps, given the established nature of fibre optic technology in general and fibre optic sensors in particular, relatively few papers have been published specifically on the subject of fibre optic WIM sensors.

A brief overview of fibre optic sensing technology is presented in Section 2.2. Section 2.3 describes various fibre optic interferometric configurations employed for sensing applications. The theoretical and design considerations of various fibre Fabry-Pérot configurations are also discussed. An introduction to in-fibre Bragg gratings, an essential component used during the construction of the Fabry-Pérot sensing element in this project, is presented in Section 2.4. Recent research on conventional WIM technologies, their limitations and efforts to overcome these limitations by adopting innovative approaches to manufacture a new type of fibre optic WIM system, is reviewed in Sections 2.5 and 2.6. To date, the major optical fibre properties that have been explored for WIM applications are polarisation, optical phase variations and modal power distribution. Section 2.7 highlights the need for new types of WIM sensing principles and proposes the improved configuration which is investigated in this thesis.

2.2. Fibre Optic Sensing Technology

Fibre optic sensing systems have been developed to monitor various measurands like, strain, temperature, pressure, flow, proximity and level. Sensing devices have been deployed for industrial process control or in non-industrial situations such as automobiles, medicine, aeronautics and consumer electronics. The development and demand of a sensing system depends on the nature of the application and the measurand to be sensed. The overlapping boundaries of industrial requirements and the evolution in sensing technique decides the market trend in the sensor industry²⁹. The initial interest in the development of fibre optic sensing technology was restricted by the nature of the worldwide sensor market. However, the fibre sensor

market has grown gradually for non-specific sensing solutions. The current market for optical fibre based sensing systems has been reported to be in the region of US\$ 550 million and is expected to reach more than US\$ 50 billion by 2008³⁰.

Many fibre optic sensing principles were adopted from advancements in telecommunications³¹. Indeed the components used for developing fibre optic sensors are also from telecommunications. For example, in-fibre Bragg gratings were initially deployed in optical telecommunication networks due to their wavelength-coded multiplexing potential. However, by monitoring the measurand-induced shift in the Bragg wavelength, a grating can serve as a sensing element³². Couplers³³, utilised mainly for dividing or combining optical signals for optical fibre information systems, may be used in interferometric sensors for splitting and combining optical beams. Single mode optical fibres are ideal for interferometric sensors³⁴ as they allow guidance of an interference pattern directly along a fibre. Doped optical fibres were developed for amplifying communication signals in the optical domain thereby overcoming bottlenecks introduced from the conversion of optical signals into electrical signals and vice versa. These doped fibres have a temperature dependence of absorption or fluorescence³⁵ that may be used for temperature sensing applications³⁶. Moreover, there are technologies developed explicitly for sensor applications, such as small diameter fibre for fibre gyroscopes, silicone-rubber fibres for weigh-in-motion³⁷, high-Verdet constant (magnetic glass) for magnetic field sensing³⁸, and special doped fibres for temperature sensing³⁵. The main advantages of optical fibres, for use as sensors, are discussed in the next section.

2.2.1. Advantages of Optical Fibres for Sensing Technology

An overview of fibre optic sensing technology¹⁵ documents the steady growth of the field in the past few decades, which has resulted in several hundreds of sensors and working principles/configurations^{34,39}. Optical fibre sensors offer the following advantages over conventional electrical sensing systems.

- Immunity to electromagnetic interference
- Chemically inert - useful in medical and chemical applications

- Capability to be multiplexed
- Non-intrusive nature (non-electrical, negligible ignition risk)
- Low attenuation, allowing the instrumentation to be situated possibly many kilometres from the sensor.
- Small size, light weight and geometrical flexibility
- Convenient for distributed sensing as well as point sensing
- Ability to perform a wide range of measurements via optical fibre
- Ruggedness and corrosion resistance
- Highly specific and direct nature of many optical measurements, and high speed of response

Emerging fibre optic technologies enable new sensing systems not previously possible. The advantages listed above have increased the popularity of fibre optic sensors in fields such as medical⁴⁰, chemical⁴¹ and environmental⁴² sciences to monitor various measurands like temperature⁴³, rotation (gyroscopes)⁴⁴, electric current and magnetic field^{38,45}.

2.2.2. Optical Fibres for Structural Sensing Applications

With the increasing prevalence of large and complex civil and mechanical structures, such as dams, bridges, buildings, tunnels, aircraft, transport infrastructure and heavy plant equipment, there is a corresponding need to establish controlled monitoring and maintenance regimes to ensure their ongoing viability and safety. Periodic engineering inspections of such structures have been the traditional approach to structural integrity monitoring, but these inspections can return limited data only. The risks of insufficient or inadequate information are two-fold. On one hand, problems can be missed or remain undetectable, particularly when they are buried deep within the structure, leading to unexpected structural failures. On the other hand, attempts to avoid such failures in the face of insufficient data can lead to premature abandonment, replacement or unnecessary and expensive modifications to structures, often using statistically-based assumptions such as “mean time to failure”

calculations. More extensive data can prevent costly mistakes and reduce reliance on statistical methods of structural integrity assurance.

The notion of instrumenting large structures to obtain continuous information about the state of the structure is not new, and structural instrumentation is a very large and diverse branch of engineering. In practice, the construction and performance of virtually every structure is sensed and monitored already to a certain extent; this might be a simple visual observation or a very sophisticated electronic or optoelectronic system. Instrumentation of this kind can be either external or internal to the structure.

More recently, there has been a growing movement towards building "intelligence" within civil structures. The idea here is that the structure can sense changes in its internal state due to environmental or other external loading effects. A control system (computer, microcircuit or the like) attached to the structure assesses these changes, and actuators placed within the structure allow it to respond to these changes. These structures known as "Smart Structures"^{23-26,46,47} are enabled by embedded sensors^{48,49}. Presently such smart civil structures are relatively low in number and limited in scope. However, the number of potential applications is great. The major applications of smart structure technologies involve real time or long term health monitoring of structures such as buildings, dams, bridges, aerospace components and highways^{19-21,50-52}.

In addition to monitoring the integrity or state of a structure, embedded sensors can return useful information about the everyday operation or environment of the structure. In so doing, embedded sensors can recover indirectly the state of other parameters affecting the host structure. Examples of instrumented structures include a bridge to measure average traffic loads, a tall building for lateral strain measurements that can return data on local wind conditions, and a road to sense weights of vehicles travelling along it.

2.2.3. Optical Fibre Sensing Configurations

Classification of fibre optic sensors is necessary for understanding the requirements of the sensor market and the enabling technology. As discussed in Section 2.2, most of the sensing market is fragmented, and therefore the market outlook is important for developing new sensors for a particular type of application. Although it is difficult to define the boundaries of fibre optic sensing configurations⁵³, common classifications of fibre optic sensors are based on their functionality, as follows⁵⁴.

(a) The Type of Optical Fibre used in the Sensing Element - Optical fibre sensors can be classified from the type of fibre used, such as multimode, few mode, two mode or single mode sensors. Most commercial fibre optic sensor systems are based on multimode (core diameter 10-50 μm) optical fibres. The large core diameter increases the light gathering capacity of the system allowing the use of low cost light emitting diode (LED) sources and commonly available optical components. These sensing systems offer cost competitiveness with conventional sensors. Few moded and two moded sensors are based on the statistical redistribution of the measurand induced modal interference within the fibre. On the other hand, single mode (fibre core diameter, $\sim 5 \mu\text{m}$) sensors have received considerable attention for developing interferometric systems.

(b) The Construction Mechanism of the Sensing Element - In extrinsic or hybrid sensors the light is modulated outside the fibre by the measurand. However, in the case of intrinsic sensors, light modulation takes place inside the optical fibre. The sensor developed during the present project is intrinsic in nature. In extrinsic sensors, the sensing element assembly is developed using miniaturized conventional optical components that are designed to modulate one/many of the properties of the incident light affected by the environmental perturbation. The optical fibre transmits the light to the sensing element, which modulates the light and couples it back along the fibre to the optical detector. In contrast with this mechanism, an intrinsic⁵⁵ sensor operates through direct modulation by the

measurand of the light guided inside the fibre in which case light only leaves the fibre at the detector.

(c) The Degree of Localisation - A point sensor is capable of sensing the measurand at one point only. On the other hand, a distributed sensor is designed to monitor various or the same parameter(s) at multiple points. Point sensors, by comparison, respond locally to perturbations at one point in an optical fibre. Detection of structural variations over an extended region is possible by multiplexing several point sensors⁵⁶. Multiplexed point sensor systems have a suitable signal processing unit to identify the various responses of each point sensor in the network. Moreover, multiplexed point sensors can also be employed for multi-measurand sensing applications where different measurands at each sensor can be monitored separately, eg. pressure at one point and temperature at another point. In so doing, a self-calibrating sensor array can be created which accounts for “cross-sensitivities” at each sensor (for example, where a strain sensor might respond differently at a different temperature). This type of multiplexing, while returning a wealth of data, can be both complex and expensive. Distributed sensors respond to changes along a length of fibre and may be used to instrument an extended region with uniform sensitivity. Some distributed sensors can resolve the measurand at different distances along the sensing fibres, whereas others act to integrate a measurand along the entire sensing fibre to produce a single valued output at any instant. Distributed sensors are based mainly on the principle of time-domain reflectometry, in which optical radar is used to test the continuity of the fibre by monitoring the time domain back-scattered attenuation of a short light-pulse launched in the fibre⁵⁷. For the present application, it is important that the sensor should detect the passing vehicle irrespective of its lateral position across the width of the road. Therefore, the fibre optic distributed sensing technique, that integrates the effect along the entire sensing length of the fibre, was used. The present sensor may be considered as an *extended point sensor* or *long point sensor*.

(d) Optical Transduction Mechanism – The most common optical effects induced in a sensor are intensity changes and path length changes. Most intensity-based fibre sensors employ multimode fibre for greater optical power and better signal-to-noise ratio, and may be realised by exploiting absorption, scattering⁵⁷, bend loss⁵⁸, or some other power coupling mechanism mediated by the measurand. Optical path changes are most commonly exploited in single mode fibre sensors, and can be detected either through time domain methods (not common), or more usefully through an interferometric approach (details in Section 2.3) which makes use of the large path sensitivity permitted by the short wavelength of light. Fibre optic sensors can also act via changes in the mode distribution of the light. These sensors include polarisation-based sensors (polarimeters), spatial mode sensors, sensors based on frequency or wavelength changes in the light (caused for example by Doppler shifts or non-linear effects in the fibre).

To summarise, the sensor investigated in this thesis employs *single mode* optical fibre as the sensing element and the light is modulated *intrinsically* to develop an *extended/long* point sensor with *distributed* sensing capability. Moreover, the sensor converts optical phase changes induced by the measurand into *intensity modulations* at the detector.

2.3. Interferometers

2.3.1. Bulk Optic Interferometers

An interferometric arrangement consists of a single monochromatic (coherent) light beam that is then split into two signals that traverse different paths. One arm contains the sensing region and the other is the reference arm. An interference pattern can be obtained by superposition of the sensing and reference beams. This output interference pattern reveals information about induced changes in the sensing arm. As interferometric systems require coherent light, the coherence length of the source becomes an important parameter. Coherence length is the maximum path difference that can be introduced between the two arms of an interferometer before

the phase difference between the recombined beams becomes random. The corresponding temporal period is known as the coherence time.

Consider a sensing arm of length L and assume the refractive index in both arms is n . When the sensing arm is unperturbed, the reference and sensing beams have identical phase ($\phi = 2\pi nL/\lambda$) when they recombine and therefore the output intensity is a maximum. When the sensing arm undergoes perturbation, the length mismatch between the reference and sensing arm produces a phase difference ($\Delta\phi$) between the reference and sensing beams, as shown in Figure 2-1, given by

$$\Delta\phi = \frac{2\pi n\Delta L}{\lambda}. \quad (2-1)$$

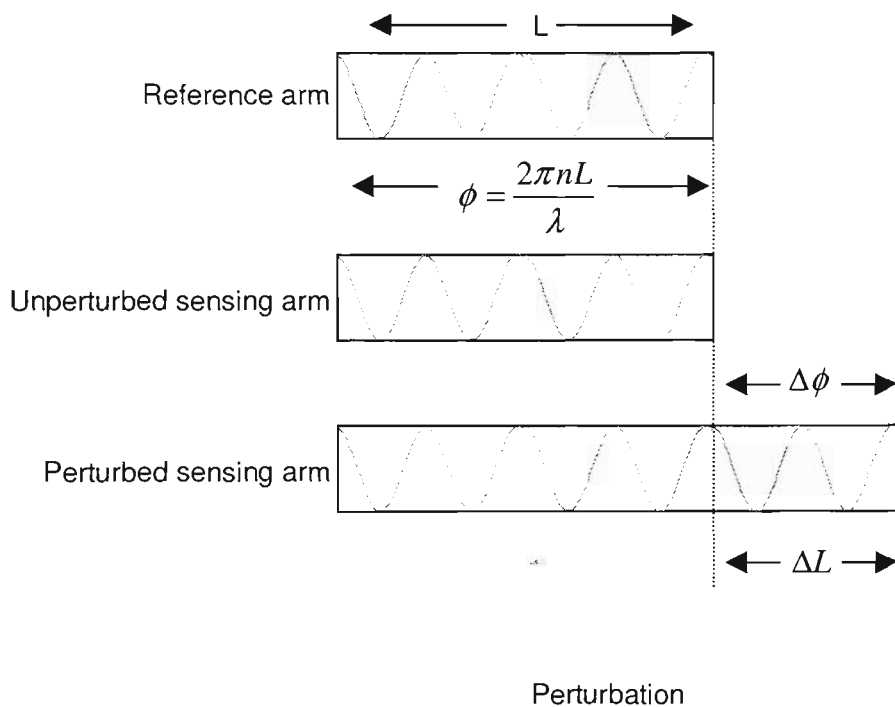


Figure 2-1: Basic concept of interferometry.

The output beams interfere destructively to give minimum intensity at the detector if the phase difference is an odd integer number of π (i.e. $\pi, 3\pi, 5\pi, \dots$). On the other hand, constructive interference occurs when the phase difference is an even integer number of π (i.e. $0, 2\pi, 4\pi, \dots$) to produce maximum intensity at the detector. The sensitivity function is defined as the rate of change of intensity, and is a maximum at

$\pi/2, 3\pi/2, 5\pi/2, \dots$ and known as the quadrature points as shown in Figure 2-2. The sensitivity falls to zero mid-way between these quadrature points.

There are four basic interferometric configurations³⁴ (1) Mach-Zehnder, (2) Michelson, (3) Fabry-Pérot and (4) Sagnac. The first three, Mach-Zehnder, Michelson, and low finesse Fabry-Pérot, are two beam configurations. High finesse Fabry-Pérot and Sagnac configurations are examples of multiple reflection interferometers. The bulk optic interferometric principles and arrangements discussed above can be implemented as fibre optic interferometers.

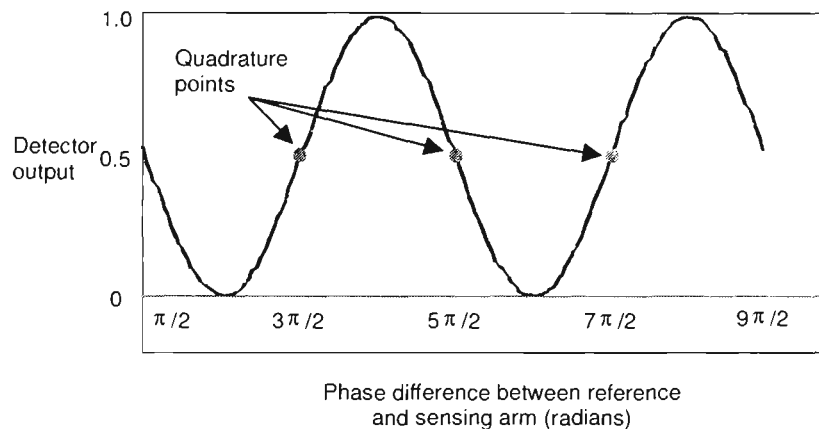


Figure 2-2: Sinusoidal fringe pattern from an interferometer at the detector and the quadrature points. The sensitivity of an interferometer is a maximum at the quadrature points.

2.3.2. Multiple Beam Configurations

Standard optics texts describe the theory of multiple beam interferometers in-depth^{59,60}. In a Sagnac interferometer (Figure 2-3(a)) only one fibre loop is required. One part of an equally split light signal is passed clockwise and the other half of the signal passes counterclockwise through the same fibre loop. When the loop undergoes rotation in either direction, the path length of the signals in the direction of the rotation is elongated and introduces a path difference between the clockwise and counterclockwise signals. This principle is known as the Sagnac effect, and is employed in instruments that detect rotation rate such as gyroscopes⁶¹. The ring

resonator (Figure 2-3(b)) has a similar working principle and relies on the partial recoupling of light to a recirculating optical path and outputs the superposition of the multiple beams. The analysis of a ring resonator arrangement is more complex than a Fabry-Pérot configuration because the coupler and the fibre loop can not be regarded as lossless. A Fabry-Pérot interferometer (Figure 2-3(c)) consists of an optical cavity formed between two mirrors. Multiple reflections occur between the two reflectors. The output fringe quality depends on the reflectances of the end reflectors. The high mirror reflectances of these configurations allow higher order multiple reflections, and so this configuration has the highest phase sensitivity among all the interferometers.

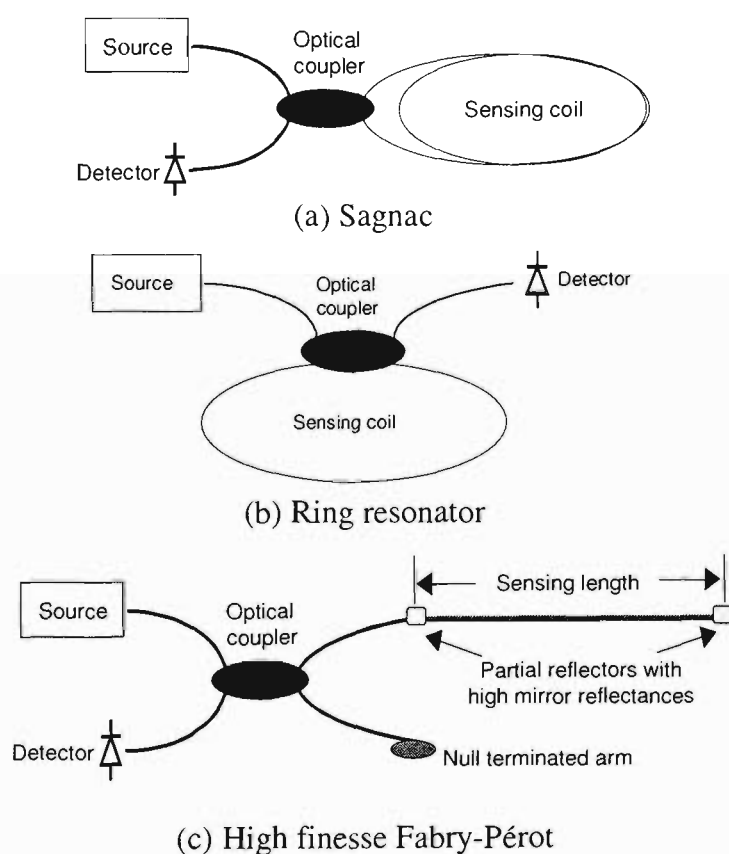


Figure 2-3: Multiple-beam fibre interferometric sensing configurations.

2.3.3. Two Beam Configurations

In two-beam interferometers, the reference and sensing arms are physically different and hence possible random perturbations can be reduced by keeping the reference arm under a controlled environment. A Mach-Zehnder interferometer is more

complex than the Michelson configuration as it uses two optical couplers. However the major advantages of a Mach-Zehnder configuration is a reduction of optical feedback to the source that can induce random changes in its output frequency⁶². On the other hand, two beam configurations based on conventional low-birefringence optical fibres suffer from polarisation-induced fading as a consequence of random fluctuations in the state of polarisation of the two interfering beams⁶³. High-birefringence fibres and fibre components may be used instead, but these increase the cost and complexity of the sensing system.

For the Fabry-Pérot configuration with low mirror reflectances, higher order reflections in the cavity can be neglected. In this case, the Fabry-Pérot optical cavity output can be considered as a double-pass interferometer similar to the Michelson. However, instead of two arms as in a Michelson configuration, a Fabry-Pérot with low mirror reflectances offers similar sensitivity using single arm access to the sensing region and allows the source and detector to be accommodated in a single compact unit. Two-beam fibre interferometric configurations are depicted in Figure 2-4.

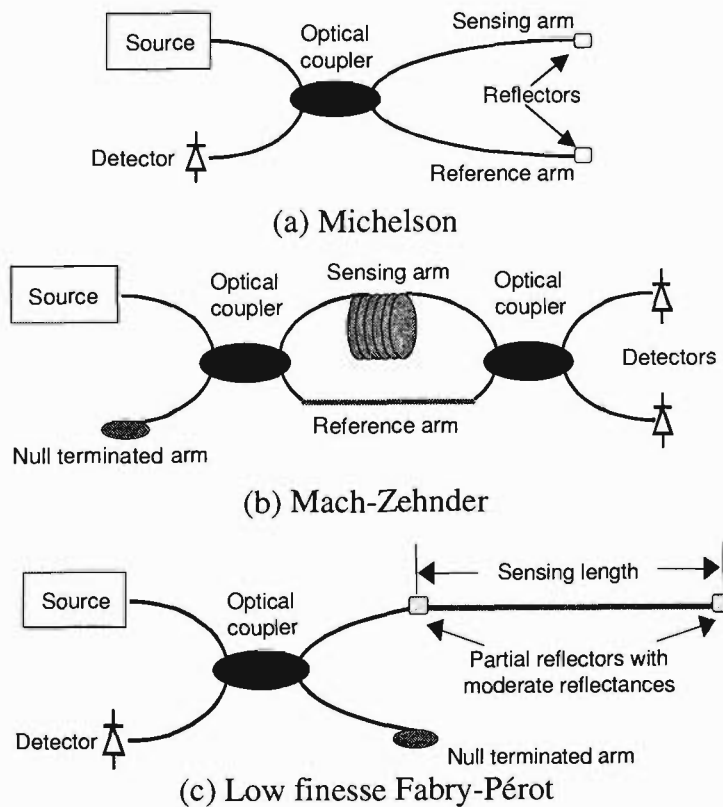


Figure 2-4: Two-beam fibre interferometric sensing configurations.

2.3.4. Phase Shift Detection Methods

As discussed in Section 2.3.1, the relative phase difference between the reference and sensing arm of an interferometer is represented in terms of the number of fringes. Microscopic changes in the measurand are detectable by locking a fringe at a particular phase and monitoring the sub-fringe-level phase shifts.

Interferometers operating on the sub-fringe accuracy level employ one of a number of methods:

(a) Active Homodyne: The quadrature condition is achieved by introducing a phase modulator in the reference arm which adjusts the phase to achieve the maximum sensitivity of the configuration. This correction which drives the modulator becomes a measure of the optical path length change in the sensing arm⁶⁴.

(b) Passive Homodyne^{65,66}: In this type of phase demodulation two signals with relative phase difference of $\pi/2$ are obtained from the interferometer. Mathematical operations like squaring, addition, cross-multiplication or differentiation can be performed on these two signals using appropriate electronics to determine the phase shift between the reference and sensing beams.

(c) Heterodyne Techniques: In this processing system, the frequency of one of the interfering beams is shifted using an acousto-optic modulator, like a Bragg cell⁶⁷. This introduces a beat between the two interfering beams that can be monitored. Fibre optic interferometers employ methods such as (i) synthetic heterodyne⁶⁸, (ii) pseudo-heterodyne⁶⁹ and (iii) quadrature recombination heterodyne⁷⁰.

Interferometers are very sensitive devices and can detect changes of the order of 10^{-14} m in the optical path difference between the reference and the sensing beams⁷¹. The ultimate detectable signal is limited by shot-noise determined by the photodetector. The variation of the minimum detectable displacement and equivalent phase shift as a function of frequency suggests that phase shifts below 10^{-6} rad can be

detected at frequencies above 100 Hz while the signal amplitude falls rapidly at low frequencies⁷².

On the other hand, free-running interferometers are usually employed for large operating ranges where the expected phase excursions are much greater than π . Such interferometers can be used for applications in which the total number of fringes is approximately linear with changes in the measurand. A direct readout technique based on 'fringe counting' can be employed. The accuracy of such a system depends on the fringe detection/counting module that recognises a fringe and determines the total number of fringes that occurred during a particular event. For example, in the case of an embedded structural sensor, the total number of fringes that occurred during deformation is proportional to the induced structural variation.

2.3.5. Fibre Fabry-Pérot Interferometer (FFPI) Construction

The conventional Fabry-Pérot Interferometer (FPI) is a particularly simple configuration consisting of an optical cavity formed between two partially silvered mirrors. A schematic of a bulk optic FPI configuration is shown in Figure 2-5.

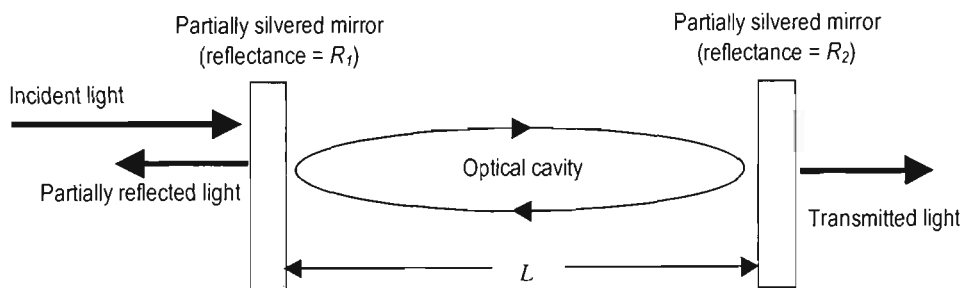


Figure 2-5: Bulk optic Fabry-Pérot Interferometer (FPI).

A fraction of the light, incident on the input mirror, is reflected towards the source while the remainder is transmitted to the second mirror, whereupon multiple reflections can occur between the mirrors. Optical resonance occurs when the round trip optical path is an integer number of wavelengths. The fraction of light transmitted and reflected from the interferometer and the amount of light stored

between the mirrors depend on the individual mirror reflectances and losses and on the ratio of the distance between the mirrors to the optical wavelength.

The fibre optic version of a Fabry-Pérot interferometer (Fibre Fabry-Pérot Interferometer, FFPI) can be designed by constructing partially reflecting mirrors butted to cleaved fibre ends⁷³ or within the fibre core^{74,75} (Figure 2-6).

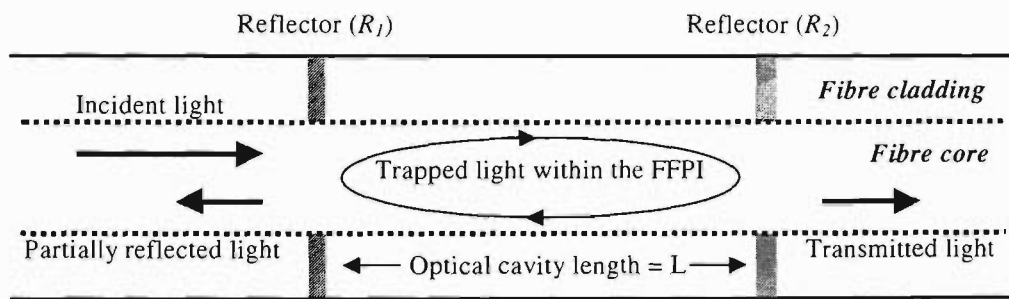


Figure 2-6: Fibre optic Fabry-Pérot Interferometer (FFPI) with in-line reflectors.

Early FFPIs were constructed by butting external mirrors to each end of the fibre. Petuchowski *et al.*⁷³ described an interferometer consisting of a single mode optical fibre of 40 cm length. They used two dielectric mirrors, with transmittances of 2.6 and 8.3% at 632.8 nm, butted at both ends. These FFPI sensors were bulky and difficult to embed in structures. Therefore, to overcome this problem, FFPI sensors with in-fibre mirrors have been investigated by a number of authors. The process of creating in-fibre mirrors involves cleaving of a fibre, depositing a reflective coating on one of the cleaved fibre ends and splicing this (mirrored) end to the other (non-deposited) cleaved fibre end. Various versions of a FFPI have been constructed using in-fibre reflectors created either by dielectric coatings⁷⁴ or metallic coatings⁷⁵. A multilayered dielectric coating⁷⁴ was deposited on the optically polished fibre-end using vacuum evaporation techniques. Another method of creating internal mirrors⁷⁶ involved sputtering a TiO₂ film onto a cleaved fibre-end. However, once the cleaved ends were coated to form internal mirrors, it is difficult to align the fibre cores for splicing without damaging the coating. Hence, complicated splicing techniques were developed⁷⁷. For example, the TiO₂ coated fibre end⁷⁶ was spliced to the other fibre by operating the splicing unit at a much lower arc current. A number of splicing

pulses were used to produce each reflector⁷⁴. A similar splicing method was used to achieve metallic (silver) coatings⁷⁵.

It is possible to avoid complexities in the splicing technique and associated losses within the optical cavity by writing Bragg gratings into the fibre core⁷⁸ (in-fibre Bragg grating, IFBG) instead of using internal mirrors. This is attractive since the Bragg gratings are created within the fibre core without damaging the continuity of the fibre.

The fibre Fabry-Pérot interferometer used in the present studies was constructed by writing an in-fibre Bragg grating near one end of an optical fibre, the other end of which was cleaved and sputtered with gold to create the end mirror. This approach avoids the need to fabricate two gratings in one piece of fibre – a difficult task when each grating has to be monitored transmissively during fabrication to tune its reflection spectrum to the desired central wavelength. It is of course possible to splice together two fibre segments containing individual IFBG's to make the desired optical cavity but the splice introduces potentially serious loss and unwanted reflections.

2.3.6. FFPI Theory

This Section discusses basic FFPI theory necessary for the design of the sensing system. Consider an in-fibre cavity of length L_{FFPI} formed between two reflectors with reflectances R_1 and R_2 . The effective optical cavity length L_{FFPI} , which determines the resonance condition of the FFPI, is given by integrating the refractive index profile $n(z)$ along the actual fibre length L between the reflectors:

$$L_{FFPI} = \int_0^L n(z) dz \quad (2-2)$$

$$L_{FFPI} = n L \quad \text{if } n(z) \text{ is constant.}$$

The resonance of an optical cavity depends on L_{FFPI} and the wavelength (λ) of the incident light. The round trip optical phase ϕ is the key parameter here (Figure 2-1):

$$\phi = \frac{4\pi nL}{\lambda}, \quad (2-3)$$

where n = refractive index of the region between the mirrors (assumed uniform here), and λ = free space optical wavelength.

At resonance, the transmitted light (T_i) is maximised. Moreover, the light emerging towards the source from within the cavity tends to cancel partially the light directly reflected off the input mirror from the light source and minimises the reflected light. Thus, the light reflected or transmitted from the cavity, on or off resonance, depends on the reflectance R_i and transmittance T_i of each mirror ($i = 1, 2$). The fraction A_i of light lost by absorption or scattering at each reflection also influences the amount of light reflected and transmitted from the cavity since it can strongly affect the buildup of light within the cavity. For each reflector, conservation of energy demands that:

$$R_i + T_i + A_i = 1 \quad (i = 1, 2). \quad (2-4)$$

The reflectance (R_{FP}) and the transmittance (T_{FP}) of the optical cavity is given as follows^{79,80}:

$$R_{FP} = \frac{R_1 + R_2(1 - A_1)^2 + 2\sqrt{R_1R_2}(1 - A_1)\cos\phi}{1 + R_1R_2 + 2\sqrt{R_1R_2}\cos\phi}, \quad (2-5)$$

$$T_{FP} = \frac{T_1T_2}{1 + R_1R_2 + 2\sqrt{R_1R_2}\cos\phi}. \quad (2-6)$$

The transfer function of a Fabry-Pérot interferometric configuration is described by the well known Airy function plotted in Figure 2-7 at mirror reflectances 0.1, 0.3, 0.5 and 0.7, in reflection mode.

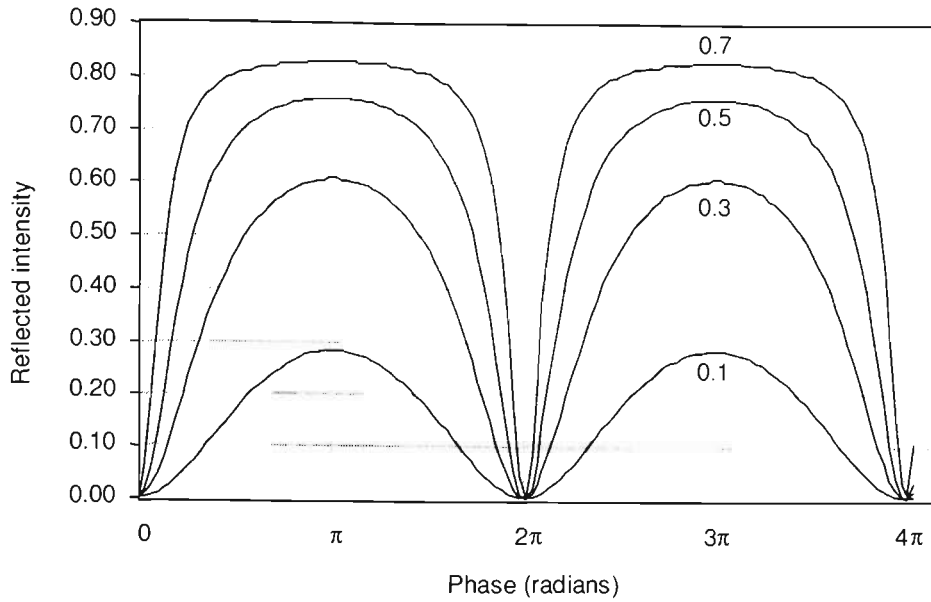


Figure 2-7: Theoretical plot showing variations in the output intensity of a symmetric Fabry-Pérot interferometer in reflection mode as a function of phase difference, for mirror reflectances of 0.7, 0.5, 0.3 and 0.1.

From equations (2-1) and (2-2) it can be shown that the reflectance is a periodic function of the round trip optical phase ϕ with transmission maxima separated by $\Delta\phi = 2\pi$, which corresponds to a change $\Delta(n.L)$ in the FFP optical path length of $\lambda/2$. The sharpness of these maxima is described by the finesse F of the FFP, defined as:

$$\text{Finesse} = \frac{\text{Separation between two consecutive peaks}}{\text{Full width at half maximum}}$$

For the case $R = R_1 = R_2$ (assuming R is close to 1), the finesse is

$$F = \frac{\pi\sqrt{R}}{(1-R)}, \quad (2-7)$$

and therefore F is large. For reflective and lossless mirrors the value of reflectance, R , is very high (~ 0.99). On the other hand, mirrors with low reflectances are particularly popular for sensing applications. Assuming lossless mirrors with equal reflectances ($R = R_1 = R_2$) where $R \ll 1$, equations (2-5) and (2-6) can be written as:

$$R_{FP} \cong 2R(1 + \cos\phi), \quad (2-8)$$

$$T_{FP} \cong 1 - 2R(1 + \cos\phi). \quad (2-9)$$

The value of finesse is undefined for $R < 0.172$, and hence the concept of finesse does not apply for Fabry-Pérot interferometers with $R \ll 1$ ⁸⁰

High finesse interferometers are popular for detecting spectral features located precisely in the output fringe pattern. These configurations operate in the extremely high slope region of the fringe pattern and hence these can detect the smallest change in the measurand. However, a complex feedback system is necessary to lock the fringe at the maximum sensitivity to monitor this phase change⁸¹. On the other hand, low finesse interferometers offer linear operation over a larger measurand range without complex feedback schemes. Figure 2-7 shows the reflected intensity from a Fabry-Pérot interferometer in the symmetric case (equal mirror reflectances) as a function of the phase difference, and shows the periodic variations ("fringes"). Figure 2-7 shows a narrower fringe pattern for the higher mirror reflectances as compared with almost sinusoidal fringes at lower mirror reflectances.

The Fabry-Pérot interferometric configuration has been demonstrated for monitoring parameters such as temperature, mechanical vibration, acoustic waves, magnetic fields and voltage⁷⁴. As discussed in Section 2.2.3, the location of the mirrors in the sensing element determines the *intrinsic* or *extrinsic* nature of the FFPI sensor. In an extrinsic FFPI configuration, the second reflector forming the sensing cavity is positioned outside the fibre at the end of the extended optical path and it may consist of another fibre⁸² or membrane⁸³ enclosed in a protective sensing head assembly. Extrinsic FFPI etalons are used mainly as surface mounted transducers, for monitoring strain, temperature⁸⁴ or acoustic pressure in the structure, and provide better access to the sensing head for repositioning or replacement.

On the other hand, by embedding the sensing element, it is possible to monitor parameters at locations which are not accessible to surface mounted transducers. An intrinsic⁵⁵ FFPI is a compact, in-line sensing element that is readily incorporated into

a structure without affecting its integrity. An embedded intrinsic FFPI has been demonstrated for monitoring the condition of concrete bridges²¹.

A hybrid sensor⁸⁵ has also been demonstrated which combines the best qualities of both intrinsic and extrinsic FFPI sensors. This in-line fibre etalon uses a short segment of silica hollow-core fibre spliced between two sections of single mode fibre to form a mechanically robust optical cavity.

A major problem for all non-fibre conventional embedded sensors is the difficulty of embedding a sensor in the structure itself. To embed a sensor successfully in a concrete, composite or metal, the transducer must withstand the mechanical and thermal stresses experienced during installation. However, silica fibres containing internal dielectric mirrors, to form FFPIs, have excellent mechanical properties and meet such installation requirements⁸⁶. Also, an optical fibre sensing element provides flexible sensing lengths suitable for installation into various structural geometries.

2.4. In-Fibre Bragg Gratings (IFBG)

2.4.1. Introduction

In-fibre Bragg gratings are created by photo-inducing periodic variations in the refractive index along the core of a photosensitive optical fibre. The use of special photosensitive germanium or boron doped silica fibres enables the production of sufficiently high refractive index perturbations. The photosensitivity can also be generated in standard telecommunication fibres by exposing them to a high pressure hydrogen environment for some period of time prior to the IFBG writing process. Photosensitivity is most efficient in the ultraviolet region of the spectrum. In-fibre Bragg gratings have been used as reflectors to replace mirrors or coatings⁸⁷. Bragg gratings have advantages over conventional mirrors because of their integration within the fibre (making them relatively simple to include in a fibre optic system, avoiding weak splices and extra reflecting surfaces). Unlike simple reflecting mirrors, in-fibre Bragg gratings have a wavelength-dependent output and hence they can be used efficiently for multiplexing⁸⁸.

2.4.2. Writing Mechanism

Hill *et al.*⁸⁹ in 1978 first reported an IFBG in a germanium doped optical fibre core by coupling highly intense counter-propagating laser beams from an argon ion laser operated at 488 nm or 514.5 nm. In this case, the writing mechanism was shown to be an interaction of two photons, which combine to produce a single photon with combined energy, known as a two-photon process.

The manufacturing of an optical fibre involves a chemical vapour deposition technique. This technique introduces an oxygen-vacant 'defect' absorption band at around 245 nm in GeO₂ doped silica fibre cores. The photons in the region of 245 nm can readily affect Si-Si, Ge-Ge and Si-Ge bonds resulting in a slight reduction of the refractive index of the fibre core.

2.4.3. Fabrication Technology – A Review

The original IFBG fabrication technique^{89,90} (Section 2.4.2) produced periodic perturbations of the refractive index along the length of germanosilicate optical fibres. Using this method, very narrow-band permanent Bragg reflectors with reflectances approaching 100% were formed.

Subsequently, a 'side writing' technique⁹¹ was discovered which uses a two-beam ultraviolet interference pattern to write the grating from the side of an optical fibre. This technique has improved writing efficiency and demonstrated the possibility of producing gratings with an arbitrarily selected Bragg wavelength simply by altering the angle between the two interfering ultraviolet beams. Ultraviolet irradiation is used, as in the earlier approach, corresponding to the oxygen defect band of Ge.

Thus any process that creates an interference pattern, such as a diffraction phase mask⁹² or a prism interferometer⁹³, can be utilized for 'side writing'. The phase mask technique has the advantage that the Bragg grating periodicity is half that of the phase mask and is insensitive to the angle of incidence of the writing beam. This also

reduces the requirement for mechanical stability of the fibre holding arrangement. However, using a phase mask allows gratings to be written at one Bragg wavelength only defined by the spatial period of the mask and the refractive index. On the other hand, a prism interferometer offers flexibility in producing gratings with an arbitrarily selected Bragg wavelength by adjusting the angle of the incident beam on the prism surface. The present project uses a specially developed prism interferometer method⁹⁴, described in Section 3.2. All these IFBG manufacturing techniques use fibre that had the coating removed. However, recently grating writing through the fibre coating at 244 nm and 248 nm⁹⁵ has been demonstrated.

Initially, fibre gratings were fabricated using Ge-doped fibres⁸⁹. Later, the use of the hydrogen-loading technique⁹⁶ allowed the production of photosensitivity in non-doped fibres, by using elevated temperature and high-pressure hydrogen treatment, which diffuses hydrogen molecules into the fibre.

Various IFBG geometries are illustrated in Figure 2-8

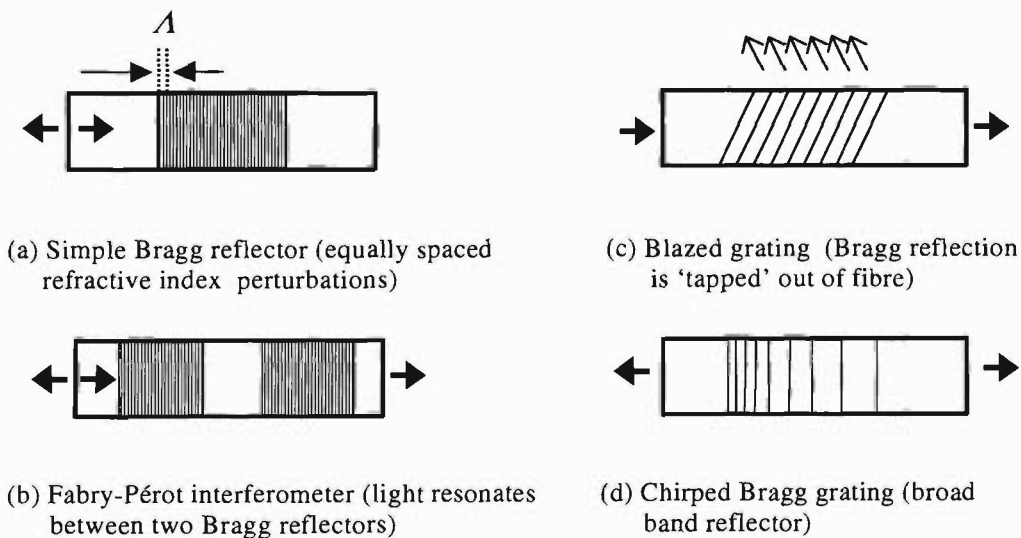


Figure 2-8: Types of Bragg grating geometries.

In the case of the simple Bragg reflector shown in Figure 2-8(a), the relationship between the Bragg wavelength ($\lambda_B = 632.8$ nm in this project) and the periodicity of the interference maxima (Λ) is given by

$$\lambda_B = 2 n_{eff} \Lambda. \quad (2-10)$$

The cavity formed by a pair of such gratings in (Figure 2-8(b)) can be used as a Fabry-Pérot interferometer. The promising future of Bragg gratings and their application in the sensing area is reviewed in detail in recent^{32,97,98}.

2.5. Weigh-In-Motion (WIM) Technology

2.5.1. Introduction to WIM Sensing

Existing WIM sensor systems can be categorised broadly according to their configuration:

(a) Bridge/Culvert Systems²⁸: these take advantage of the deflection in rigid concrete structures under roadways as heavy vehicles pass over them. An existing concrete culvert or bridge is used, or is specially installed under the roadway and instrumented with resistive or capacitive strain gauges, which monitor deflection. On-site data processing allows these systems to distinguish a single axle or groups of axles and spacings and resolve individual axle loads.

(b) Road Surface Sensors⁹⁹: these sensors consist of a transducer element, usually a capacitive strip, placed temporarily across the traffic lane together with some device (eg. an interruptible infrared beam sensor¹⁰⁰) which counts axles and measures their spacings. The overall vehicular weight is the sum of the individual axle weights.

(c) Embedded sensors¹⁰¹: the transducer element for these sensors is embedded within or beneath the solid road pavement to detect pavement and sub-pavement deflection as vehicles pass overhead. It may be configured as a distributed or point-by-point sensor.

WIM sensors offer a convenient and suitable means of gathering statistical and specific vehicular load data, which can be used for¹⁰²⁻¹⁰⁵:

- Planning and programming transportation facilities;
- Vehicle safety and compliance with vehicle weight regulations;
- Development of geometric design standards for pavements;
- Compliance and regulatory policy development of truck dimensions;
- Traffic operation and control and analysis related to highway bridges;
- Identifying road damage mechanisms, pavement design and rehabilitation;
- Determining the response of a road to vehicle load;
- Study of spatial repeatability of dynamic tyre forces.

2.5.2. Classification of WIM Sensors

Existing WIM sensors can be classified as either infrared, capacitive, piezoelectric and fibre optic. These systems monitor rapid load changes when each truck axle passes over the sensing region, which typically is configured as a strip extending across the entire vehicle lane. For surface mounted sensors, the sensing region is a narrow strip, of several centimetres width, perpendicular to the direction of vehicular motion, while sensors embedded at depth respond to vehicular loads over a region which can be many metres wide.

(a) Infrared Axle Detectors

Total vehicular weight is obtained by summing the individual axle weights; in the case of narrow strip sensors this is straightforward as each axle load is easily distinguished. For sensors with a less localised response area, axle weights may be determined by post processing the sensor data by using axle detector data obtained separately, for example, via an interruptable infrared beam. In this manner, it is possible to detect, count, weigh and classify moving heavy vehicles^{100,106,107}. Infrared axle detectors can themselves be quite sophisticated, allowing the lateral position and groupings of tyres as singles or doubles to be determined¹⁰⁸.

(b) Capacitive Sensors

Capacitive sensors^{109,110} generally consist of a pair of metal plates within some kind of extrusion or mat which deflects when a vehicle tyre rolls over it. The deformation

leads to a detectable change in capacitance between the plates and the force exerted by the tyre is determined by measuring the magnitude and duration of this change.

Cambridge University and Golden River Traffic Ltd. developed a low-cost high accuracy capacitive strip WIM sensor, which could also become a multiple sensor system⁹⁹. The calibration in a load measuring mat was independent of the vehicular speed over the temperature range of 15–40 °C. It was concluded that using a multiple-sensor configuration with an array of more than three sensors, it is possible to achieve RMS errors of approximately 5-8% as compared with 12-29% for earlier systems.

(c) Piezoelectric Sensors

Piezoelectric sensors are the most widely employed WIM systems^{111,112}. They respond to changes in the load rather than the actual instantaneous load. The piezoelectric sensing cable generates a charge which is proportional to the induced force. The gross weight is calculated by integrating the generated charge over the tyre contact length in the direction of travel¹¹³. Speed is determined by spacing two sensors with a predetermined separation along the highway. A further improvement in accuracy with this type of sensor is possible by averaging dynamic effects using a multi-sensor array^{114,115}.

2.5.3. WIM Accuracy Limitations based on Pavement and Vehicle Dynamics

The investigation of pavement-vehicle dynamics involves the characteristics of pavement response in terms of stress, strain and deflection under vehicular loads. The research on tyre-pavement interaction under the action of moving vehicular loads comprises mainly (a) road roughness, (b) vehicle speed, and (c) the truck suspension system^{116,117}. Theoretical analysis of tyre-pavement interaction requires either a coupled vehicle-pavement model or independent vehicle and pavement models. A variety of pavement dynamic and vehicle dynamic models have been studied^{118,119}. Various mechanistic procedures and their limitations have been reviewed comprehensively^{120,121}.

In the present project, a major effort was the calibration of the sensor to determine vehicular load. Significant limitations on the accuracy of WIM systems are imposed by the dynamic nature of the loads applied by moving trucks on the pavement.

2.5.4. Capabilities of Conventional WIM Technology

The WIM technologies mentioned above (Section 2.5.2) have one or more disadvantages including high cost, installation difficulties¹²² and the insufficient accuracy for regulation enforcement. The accuracy problems of most available WIM sensors arise because the systems are attempting to compute static vehicular weights from measurements of dynamic forces produced by vehicle axles as they pass over the sensor. (This will be true also for fibre optic WIM sensors.) These dynamic forces may arise from vehicular suspension design, speed, tyre pressures and axle configuration, road surface and subsurface compositions, road roughness, transducer design, and various geographical situations. Some important sources of error in WIM systems, as classified by Muhs *et al.*¹²³, are listed in Table 2-1.

Table 2-1: Sources of error in WIM system¹²³.

Vehicle	Environment	System	Roadway
Tyre characteristics: Mass, Temperature, Pressure, Diameter, Tread Pattern, Width, Balance, Suspension system, Aerodynamic lift, Acceleration.	Temperature gradients, Wind, Ice, Snow, Rain, Humidity.	Transducer design: Overall height, Impulse forces, Non-uniformity, Hysteresis, Repeatability. Signal Processing: A/D conversion, Electronic noise	Pavement design: Rigidity, Smoothness Obstructions: Potholes, Debris, Ice buildup Pavement Contour

These parameters and the dynamic nature of vehicular loads affect the accuracy of a single-sensor WIM system introducing an error factor ranging typically from ± 20 to $\pm 50\%$ ¹²⁴. However, with multiple-sensor^{115,125} WIM systems the error has drastically decreased to 5-8% depending on the number of sensors used in the system. However, as the number of sensing elements in the WIM system increases, the overall assembly becomes complex and expensive.

Table 2-2 shows a comparison of various conventional WIM technologies, based on their advantages and disadvantages as reported by Ali *et al.*¹²⁶.

Table 2-2: Comparison of various WIM technologies¹²⁶.

Technology	Advantages	Disadvantages
Deep-pit, load-cell-based scales	High accuracy; high reliability	High cost; long installation time; vault required
Low-profile, load-cell-based and bending plate scales	High to intermediate accuracy and reliability; no vault required (install in existing pavement)	Medium price
Piezoelectric WIM systems	Low cost; short installation time in existing pavements	Low reliability; low accuracy; strip contact with tyres
Capacitive pad system	No cutting of pavement; shortest in installation time	Low accuracy; low repeatability; bump on road surface.

Recent (1994-1998) large scale efforts towards improving reliability of WIM data involved a group of eleven partners and associate partners from ten European countries through the 'WAVE' (Weigh in motion of Axles and Vehicles for Europe)¹²⁷ project. This group includes research institutions, universities to assure highest scientific standards, private industries for development and commercial exploitation and road authorities to assure the suitability of the end-result to user needs. One of the aims of WAVE was to design WIM sensors using optical technology and to use tests of their viability to develop better techniques for the design of future WIM sensors. Consequently, an optical fibre WIM sensor based on changes in polarisation properties¹⁸ was developed and tested by the consortium. It is discussed in the next section.

2.6. Review of Existing Fibre Optic WIM Technology

As discussed earlier (Section 2.2.2), various fibre optic embedded sensors are now used widely in health-monitoring of civil structures. Initial reports on the use of fibre optic pressure sensors for WIM applications were published in 1989¹²⁸. Variations in

polarization, optical phase and modal power distribution within optical fibre have been investigated for WIM sensing.

2.6.1. Polarisation based Fibre Optic WIM Sensors

Alcatel Alsthom Recherche¹⁸ developed a polarisation-based optical fibre sensor system for direct installation in the road surface. This sensor exploits changes to the birefringence in a single mode fibre caused by transverse compressive forces imparted to the fibre. The optical fibre was sandwiched between two metallic ribbons and the composite transducer was embedded in an elastomer-filled trough in the road pavement. The elastomer seals the sensor from its environment while transmitting forces from vehicle tyres. The birefringence changes were found to be directly proportional to the applied vertical forces on the elastomeric surface strip. Polarimetric intensity fringes were counted to infer changes in the birefringence, and the fringe count was calibrated to allow individual axle loads to be inferred. Téral¹²⁹ has demonstrated the commercial viability of this fibre optic WIM system. It was observed that the output of this polarimetric sensor output was susceptible to hysteresis. For a given static load, the corresponding dynamic load, as inferred from phase shifts, was observed to vary $\pm 15\%$.

A new type of transducer (modulator) was designed¹⁷ (Figure 2-9) to verify the cause of hysteresis or non-linearities by changing the basic transducer mechanism itself. This version of the transducer was used in conjunction with the polarimetric approach for WIM application. However, the accuracy of these measurements were also affected by hysteresis. As the transducer mechanism was totally different in this case, it was concluded that the hysteresis is caused either by the inelastic properties of the fibre-cladding (not confirming to Hooke's law or shear stress) or by shear stress due to non-uniform application of the force on the modulator¹⁷.

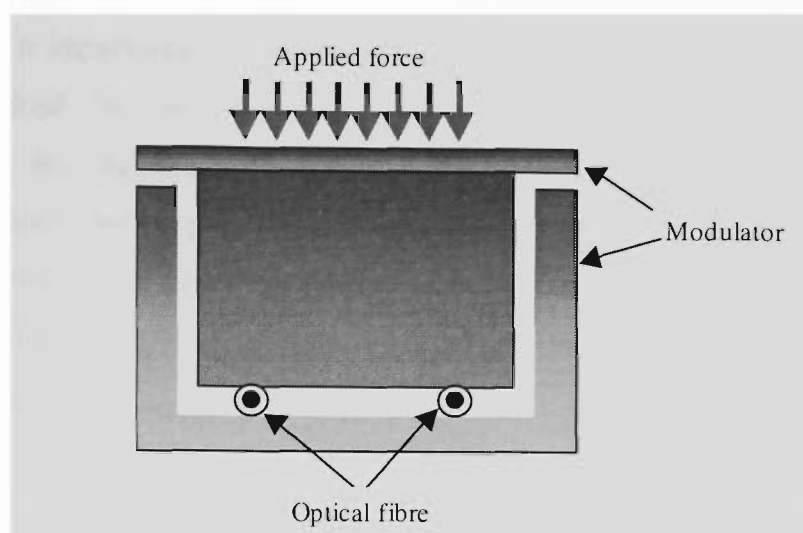


Figure 2-9: Polarization-based WIM sensor¹⁷ with transducer cross-section designed to investigate the source of hysteresis.

2.6.2. Interferometric Fibre Optic WIM Sensors

A multiple fibre optic interferometer, designed by Navarrete *et al.*¹³⁰, uses a dual-loop active homodyne system to lock the phase when the sensing fibre is subject to two simultaneous externally applied perturbations. This allows the sensor to respond to pressure (due to a passing heavy vehicle, for instance) and subtract simultaneous changes due to temperature drifts in the sensing fibre, unrelated to the measurand of interest. This system has the capability of separating induced phase changes produced by two measurands acting simultaneously on the sensing arm. The system has been demonstrated in the laboratory within an applied pressure range of 0.3–3 kPa with an error less than 2%.

2.6.3. Fibre Optic WIM Sensors based on Speckle Pattern Analysis

An intrinsic optical fibre sensor for axle detection using the speckle pattern formed by modal interference has been discussed by Ahmed *et al.*¹³¹. The monochromatic laser modes coupled into the fibre results in a speckle pattern, i.e. randomly distributed interference patterns of dark and bright spots at the output fibre-end. Any perturbations in the fibre alters the statistical distribution of the modal interference pattern and this change can be detected and calibrated using an optoelectronic detection system. The transducer can be constructed by winding a fibre helically

around a supporting deformable tube. Compression of these transducers induces micro-bends into the fibre and results in attenuation of the propagated light by altering the transmission spectrum. This system is insensitive to temperature fluctuations and long term drifts. However, this system does not have the potential for weighing nor does it detect stationary vehicles. Moreover, the system is very susceptible to remote vibrations and hence encapsulation is necessary for good repeatability.

2.7. Summary

This chapter provided a review of advancements in optical fibre sensing technology, conventional WIM sensing and newly evolved optical fibre sensors for WIM applications. Review papers published by several researchers discuss potential applications of optical fibres for WIM sensing; optical properties such as polarisation, optical phase variations (interferometric detection) and modal power distribution have been investigated. A recent paper¹⁶⁻¹⁸, describes the future need of Intelligent Transportation Systems (ITS), with concluding remarks that promote fibre optic sensors for WIM applications. Moreover, the paper also explains the disadvantage of using two arm interferometers, where, any minor perturbations in the reference arm drastically affect the sensing arm, resulting in misinterpretation of the phase change. This possibility is eliminated in the proposed sensing approach, where a reference arm is not required and instead of monitoring the sub-fringe level phase change, the total fringe counts were used for calibration. This investigation proposes a new type of single-transducer optical fibre one-arm interferometric sensing configuration to overcome these barriers for WIM applications. As discussed in Section 2.5.4, it is possible to reduce the error factor of a single-transducer WIM system by employing a multiple-transducer WIM system.

The sensor developed during this project is a single-transducer WIM sensor, with multiplexing capabilities. Like any single-sensor WIM system, the present sensor attempts to compute static vehicular weights from measurements of dynamic forces. Therefore, the accuracy of this sensor is expected to be of similar magnitude to other

single-sensor WIM systems. However, the sensor developed has the following advantages over conventional fibre/non-fibre single-transducer WIM systems:

- Easy to fabricate; suitable for mass production;
- Easy to install; low installation time, flexible sensing length, no specific site requirements such as a culvert, suitable for instrumenting various structural geometries;
- Economic, does not require expensive optical/electrical components;
- Multiplexing capabilities, suitable for configuring as a multiple-transducer sensor system.

The present research adopts a well-studied interferometric configuration - the Fibre Fabry-Pérot Interferometer (FFPI)⁷³ to develop a new type of intrinsic fibre optic single-transducer WIM sensor. Note that an extrinsic small gauge Fabry-Pérot interferometric sensor based on the optical cavity formed between an input/output fibre and a reflector fibre aligned by a hollow core silica tube¹³² has been utilised by others for highway axle detection¹³³ (not for WIM sensing) with errors of $\pm 2\%$.

The resulting intensity fringes of a FFPI can be observed and counted in either reflected or transmitted light. Optical path changes of just half of one optical wavelength (i.e. a few tenths of a micrometre) in the one-way path between the reflectors result in a complete fringe in this interferometer, making it very sensitive to length changes. This configuration has similar length/displacement sensitivity to other two-beam interferometers such as the Michelson or Mach-Zehnder configurations, when operating in “fringe-counting” mode. Other more complex signal processing techniques are also possible, such as servo-locking the interferometer to a particular phase condition. In these approaches, the interferometric phase sensitivity is enhanced by the multiple optical reflections through the sensing region in the Fabry-Pérot configuration. For the application studied in this project, it should not be necessary to develop an active fringe locking technique, as simple fringe counting should prove sufficiently accurate for these purposes.

CHAPTER 3

DEVELOPMENT OF FIBRE FABRY-PÉROT SINGLE-TRANSDUCER WEIGH-IN-MOTION SYSTEM

3.1 Introduction

This chapter describes the development of an in-fibre Bragg grating based fibre Fabry-Pérot system for generic distributed structural sensing applications. The theory of this configuration for WIM sensing and other structural sensing applications is described in Section 3.2. The critical laser parameters and their tolerances essential for qualifying it as a source for this sensing system are discussed in Section 3.3. The basic single-transducer FFPI configuration developed particularly for WIM sensing is discussed in Section 3.4. The shape of FFPI output fringes depends on the reflectances of the end mirrors of an optical cavity. It is therefore important to select appropriate mirror reflectances to obtain fringe shapes that will allow data acquisition hardware to sample each fringe with reasonable resolution. The method for selecting appropriate mirror reflectance values suitable for the fringe-counting regime is discussed in Section 3.5. An in-fibre Bragg grating was used as the launching-end mirror in the sensing elements. The temperature and strain induced changes in the central wavelength of an in-fibre Bragg grating and its effect on the sensor output is also estimated and discussed. The technique used for writing fibre Bragg gratings is discussed in Section 3.6. Models describing how the sensor monitors generic structural strains and vertical pavement strains are explained in Section 3.7.

3.2 Theoretical Strain Transfer Function

This section gives the basic theory for understanding the variations of the interferometric phase change (Section 2.3) with respect to an induced strain in the sensing arm.

A longitudinal strain applied to the sensing element alters the optical path length nL of the interferometer, where n is the refractive index of the fibre mode and L is the length of sensing fibre. As discussed in Section 2.3.1, the sensor output is a coherent summation of the amplitudes reflected by the two semi-reflective elements forming the Fabry-Pérot etalon. Moreover, the sensor output is susceptible to length changes between the two semi-reflective elements only and is insensitive to the fibre in/out leads. A low finesse Fabry-Pérot cavity can be treated as a double-pass

interferometer and therefore its sensitivity is comparable with two arm interferometers such as Michelson and Mach-Zehnder (Section 2.3.3).

In a length L of sensing fibre, the phase variation ($\Delta\phi$) induced by applying axial strain on the fibre length (L) results mainly from the physical length change (ΔL) and the change in the waveguide propagation constant ($\Delta\beta$). $\Delta\phi$ can be given as follows¹³⁴:

$$\Delta\phi = \beta\Delta L + L\Delta\beta. \quad (3-1)$$

The first term ($\beta\Delta L$) corresponds to the physical extension of the sensing fibre length and the second term ($L\Delta\beta$) results from two effects, namely (a) strain-optic effect (dependence of fibre core index, n , on the applied strain) and (b) waveguide dispersion (change in the fibre diameter (D)), i.e.

$$L\Delta\beta = L\frac{\partial\beta}{\partial n}\Delta n + L\frac{\partial\beta}{\partial D}\Delta D. \quad (3-2)$$

Therefore, by substituting Equation (3-2) in Equation (3-1), $\Delta\phi$ can be given as follows:

$$\Delta\phi = \beta\Delta L + \left[L\frac{\partial\beta}{\partial n}\Delta n + L\frac{\partial\beta}{\partial D}\Delta D \right]. \quad (3-3)$$

Here $\beta = n_{eff}k_0$, where n_{eff} is the modal effective index (value is between the core and cladding indices) and k_0 is the free space propagation constant of the mode in the fibre. However, as core and cladding indices typically differ by the order of 1%, $\beta \approx nk_0$. Hence, in Equation (3-3),

$$\frac{\partial\beta}{\partial n} = k_0 = \frac{\beta}{n}. \quad (3-4)$$

Moreover, the strain ($\varepsilon = \Delta L/L$) induced change in the refractive index of the fibre core (Δn), derived using photoelastic calculations is as follows¹³⁴:

$$\Delta n = -\frac{1}{2}n^3 \left[\varepsilon(1-\nu) p_{12} - \nu\varepsilon p_{11} \right], \quad (3-5)$$

where $n_{eff} = n = 1.46$

$\nu = 0.16$ (Poisson's ratio of the fibre material)

$p_{12} = 0.252$ and $p_{11} = 0.113$ are strain-optic coefficients.

The last term in Equation (3-3), represents the change in the waveguide mode propagation constant due to a change in fibre diameter. The change in diameter is

$$\Delta D = \nu\varepsilon D.$$

Furthermore, the term $\left(\frac{\partial \beta}{\partial D} \Delta D \right)$ can be evaluated using the normalised parameters b

and V describing the waveguide mode and equals $\left(\frac{V^3 \nu}{2\beta D^2} \frac{db}{dV} \right)$ ¹³⁵. The normalised

frequency $V = \frac{2\pi}{\lambda} a(NA)$, where a is the radius of the fibre core and NA is the fibre

numerical aperture. The normalised propagation constant, $b \equiv \frac{n_{eff} - n_2}{n_1 - n_2}$, where n_1

and n_2 are refractive indices of fibre core and cladding respectively and must lie

between 0 and 1. In fact, the term $\left(\frac{V^3 \nu}{2\beta D^2} \frac{db}{dV} \right)$ can be shown to be negligible.

Considering all these factors and substituting Equations (3-4) and (3-5) in Equation (3-3) gives the overall strain induced phase change, that can be formulated as follows¹³⁴:

$$\Delta\phi = L\varepsilon\beta \left[1 - \frac{n_{eff}^2}{2} [p_{12} - (p_{12} + p_{11})\nu] \right], \quad (3-6)$$

where $\varepsilon = \Delta L / L$ (strain on fibre)

n_{eff} = Effective refractive index of the fibre. These indices typically differ by the order of 1%, hence we can use $n_{eff} = n = 1.46$.

$\nu = 0.16$ (Poisson's ratio of the fibre material)

$p_{12} = 0.252$ and $p_{11} = 0.113$ are strain-optic coefficients.

$L =$ Sensing length

$$\beta = \frac{2\pi n_{eff}}{\lambda_0}$$

$\lambda_0 =$ Sensing wavelength, (in this case 632.8 nm for He-Ne laser).

By substituting appropriate values, the expression becomes (with $\Delta\phi$ in radians and L in metres):

$$\Delta\phi = L\varepsilon(1.15 \times 10^7). \quad (3-7)$$

By substituting 1 fringe for a phase change $\Delta\phi$ of 2π rad and $\varepsilon = \Delta L/L$ in Equation (3-7), gives

$$1 \text{ fringe} = 2\pi \text{ rad} = L \frac{\Delta L}{L} (1.15 \times 10^7),$$

thus showing the change in sensing length (ΔL) is $\sim 0.273 \mu\text{m}$ per fringe. In other words, approximately $0.273 \mu\text{m}$ of length change in the FFPI sensing fibre produces an output round trip phase change of one fringe.

For a fringe counting approach, in which the minimum resolution is a single fringe, a minimum strain of

$$\varepsilon = (\Delta L / L) = (0.273 \mu\text{m} / L)$$

can be detected, where L is the sensing length.

The sensors designed for laboratory tests consisted of a 0.3 m sensing length and, therefore, theoretically, have the ability to detect a minimum strain of $\sim 0.9 \mu\varepsilon$. On the other hand, the field sensors consisted of longer sensing lengths (4 m) than the

laboratory sensors and have the capability of detecting strains of $\sim 0.07 \mu\epsilon$. Furthermore, the variations in calculated and inferred strain values will depend on the properties of the material of the test structure and the bonding substance.

3.3 Source Considerations

(a) Frequency

Recalling that Equation (3-7) is function of wavelength, minor changes in the laser wavelength will introduce corresponding optical frequency noise. Most lasers exhibit such noise during warm-up and as the ambient operating temperature changes. Due to these frequency instabilities in the laser source, the interfering beams in the sensing arm travel different optical paths and convert optical frequency noise into optical amplitude noise and hence photocurrent noise. This affects the FFPI output by introducing a phase error in the sensing arm.

To estimate the effect, from Equation (3-6), the phase change ($\Delta\phi$ rad) can be rewritten in terms of the optical frequency (ν_o) as

$$\Delta\phi = L \epsilon \nu_o (2.43 \times 10^{-8}), \quad (3-8)$$

where L , is in m and ϵ in $\mu\epsilon$, ν_o in Hz.

A typical frequency stabilised He-Ne laser operating at a nominal frequency of a 473.61 THz has an absolute peak to peak deviation of $\sim \pm 2$ MHz¹³⁶. Hence for a constant strain of $1 \mu\epsilon$ acting on a sensing length of $L = 1$ m, this small variation in the input frequency ($\Delta\nu_o$) of the source laser directly affects the output interferometric phase by approximately ± 0.045 rad. Moreover, from Equation (3-8), for a constant applied strain, laser frequency instability ($\Delta\nu_o$) is proportional to the phase change per unit sensing length ($\Delta\phi / L$). Hence, FFPIs with longer sensing lengths are susceptible to small frequency drifts in the laser source. The acceptable levels of frequency drifts for the sensor configuration developed during this research are discussed in Section 4.2.2.

(b) Amplitude

Another important source of photocurrent noise is known as laser amplitude noise or relative intensity noise (RIN). A 1% RIN in the laser source produces a 1% noise in the output photocurrent. Typical intensity stabilised lasers have absolute intensity deviations of $\sim \pm 0.2\%$ ¹³⁶. For interferometric sensors operating in the fringe counting mode, laser intensity variations affect output fringe amplitudes and hence threshold levels of the fringe detection and counting algorithm. The threshold level in the counting algorithm was adjustable between the noise floor and the minimum fringe amplitude. If the threshold level is adjusted too high, then the algorithm fails to detect any fringes with average amplitude. On the other hand, in the case where threshold levels are adjusted too low, the algorithm detects noise as fringes. The threshold levels were optimised by visually inspecting the fringe patterns. For a typical data set in which amplitude variations are present, the algorithm fails to detect and count ~ 2 to 3 affected fringes even with the optimum adjustment of threshold level. The acceptable levels of RIN for the fringe counting algorithm developed during this research are discussed in Section 4.2.2.

For the field tests, this source dependent noise is expected to occur frequently as compared with those carried out under a controlled laboratory environment.

(c) Coherence

As discussed in Section 2.3.1, for an interferometric sensing system, the coherence length is the most important parameter for the interference condition. Therefore it is important to choose a laser source which maintains a coherence length that is, at least of the order of the sensing length in a fibre. The laboratory version and the field version of this sensor employ 300 mm and 4 m sensing regions respectively. Considering the longer sensing length, namely the 4 m sensing region of the field version operating in reflection mode, means that a source with a coherence length of more than 8 m (by neglecting higher order reflections in the sensing region) is required. As discussed in Section 3.2, the sensitivity of the sensor increases with an increase in the sensing length; the coherence length of the source, however, limits the sensing length.

3.4 Sensing Configuration

In reflection-mode, the source and detection assembly is only at one side of the sensing element enabling the use of the sensing element as a "probe" and is clearly more suitable for remote sensing applications¹³⁷, as illustrated in Figure 3-1. The present sensor adopts this approach which also allows simultaneous alignment of the optical source while monitoring the sensor output.

As discussed in Section 2.3.5, FFPI output can be monitored either in transmission-mode^{74,138} or in reflection-mode⁸⁴. The output fringe patterns of an FFPI operating in both modes at different finesse values are shown in Figure 3-2. The output FFPI fringe shapes depend on the finesse values, which are in turn a function of the cavity mirror reflectances. The method of choosing appropriate mirror reflectivities for this sensor is described in Section 3.5.

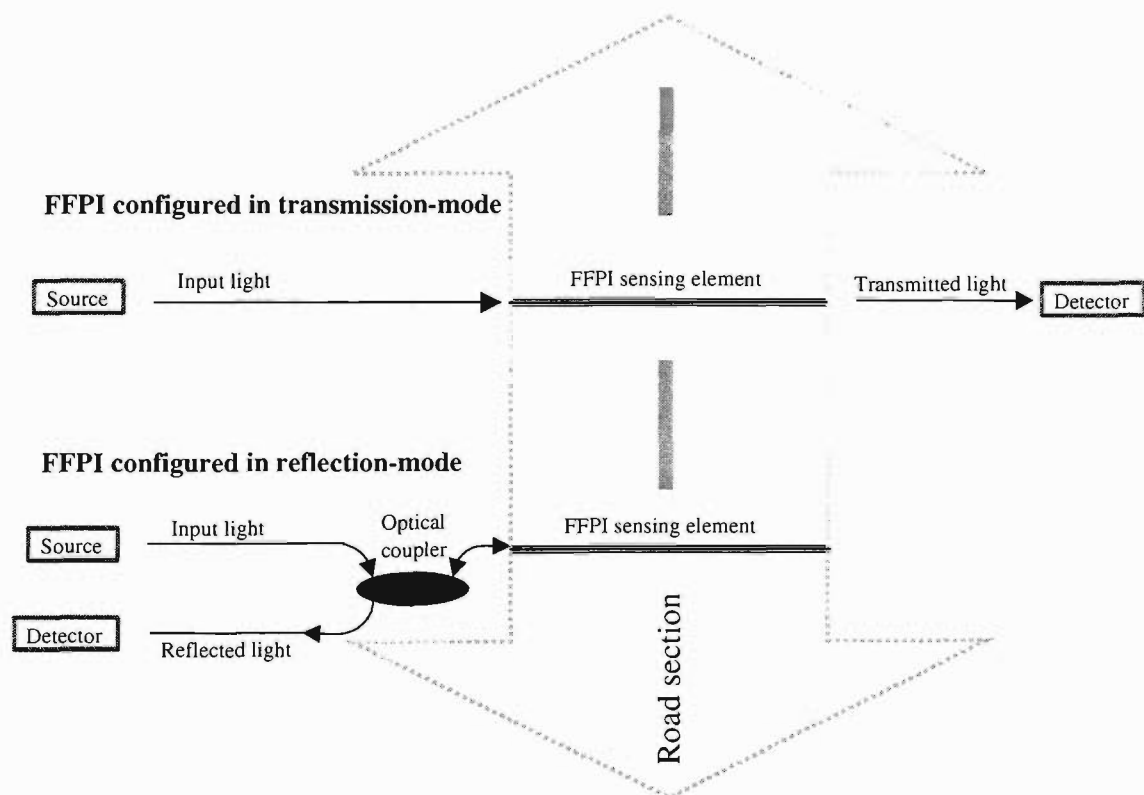
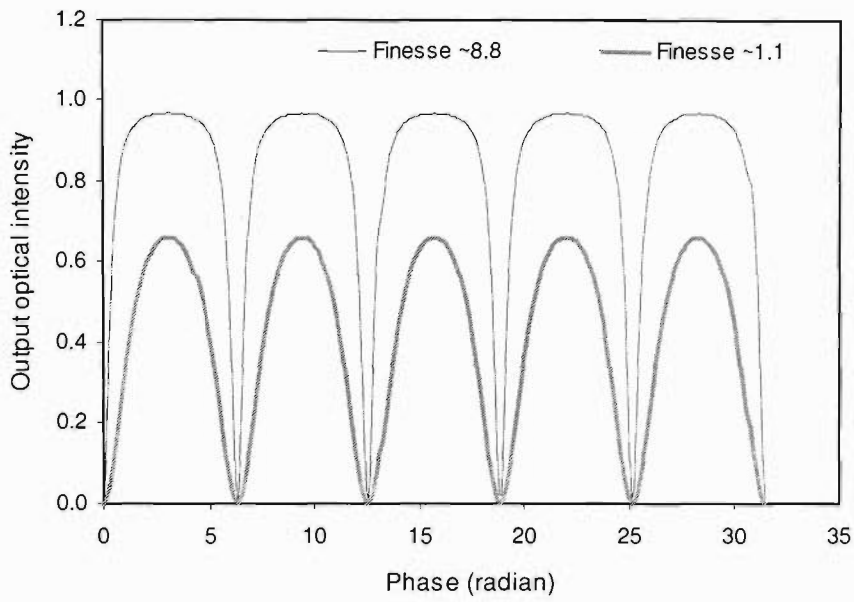
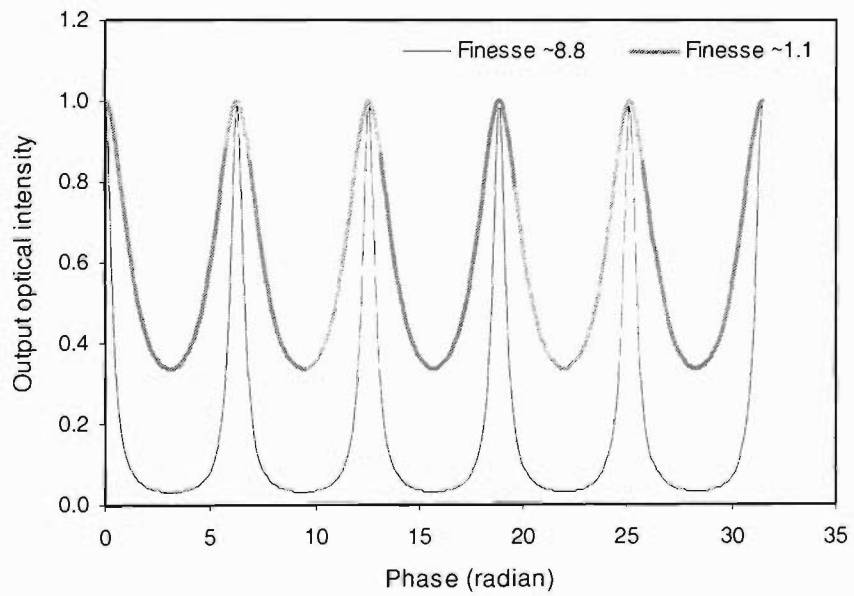


Figure 3-1: FFPI interferometers configured for monitoring output in reflection-mode and in transmission-mode.



(a) reflection mode



(b) transmission mode

Figure 3-2: Theoretical output optical intensity of a Fabry-Pérot interferometer monitored in (a) reflection mode and (b) transmission mode for two different values of finesse.

3.5 Optimisation of FFPI Output

In the fringe counting regime it is important to recognise a set of data points as a fringe. Consider the FFPI reflection fringes shown in Figure 3-2(a). The resolution of each fringe depends on the number of points defining that fringe. Low finesse optical cavities, fabricated with low mirror reflectances, produce fringes with small amplitudes. If the fringe amplitudes are too small, signal to noise ratios are a problem as the fringe amplitude becomes comparable with the electronic noise floor requiring complex fringe recognition logic for fringe-counting. On the other hand, optical cavities with high finesse values constructed using high reflectance mirrors produce fringes that are too narrow. These narrow fringes may be inadequately sampled (under-sampled) by the data acquisition hardware. This latter problem can be overcome but only by using expensive data acquisition hardware with extraordinary sampling rates. Therefore, for this research, the preference of using a FFPI configuration with high mirror reflectances has been ruled out. However, it is necessary to estimate the appropriate range of individual mirror reflectances that will output the desired fringe shape.

This section describes a suitable compromise, which achieves the required fringe resolution by selecting a moderate Fabry-Pérot finesse of the sensing element to produce a reasonable number of points per fringe, with fringes recorded using comparatively inexpensive data acquisition hardware. The range of Bragg grating reflectances required to produce this desired finesse and associated output fringe patterns is also determined in this section. Thus the shape of the output fringes was optimised to achieve necessary fringe resolution in real-time using inexpensive data acquisition hardware. As explained in Section 2.3.3, the sensitivity of a Fabry-Pérot interferometer in such cases is comparable with two arm interferometric systems.

The FFPI sensor (construction details of the FFPI sensor are discussed in chapter 4) requires two reflectors, (1) an in-fibre Bragg grating (fabrication details are provided in Section 3.6) as a launching-end mirror and (2) a gold coating as an end-reflector. The reflectance of a gold coating was calculated as a function of wavelength¹³⁹, and at 632.8 nm the reflectance was ~ 94% (R_2). By neglecting the absorption of the gold coating at 632.8 nm, the theoretical FFPI output fringe patterns were calculated using

Equation (2.5) by substituting various reflectances (R_1) of Bragg gratings, in the range of 30-70%. In each case, the frequency components associated with the fringe patterns were obtained using Fourier analysis¹⁴⁰.

Figure 3-3 shows the plot of the amplitude of the fundamental Fourier component (normalised with respect to the maximum component) as a function of Bragg grating reflectances (R_1). The amplitudes of the calculated fundamental Fourier components were, by comparison, greater than those of higher order components for Bragg grating reflectances in the range of 30-70%. The suppression of higher-order Fourier components was observed for lower Bragg grating reflectances. Hence, ideally, the sensing region (optical cavity) fabricated using a grating reflectance in the range of ~ 30-70% and a gold coating (reflectance ~ 94% at 632.8 nm) will output fringe patterns that can be recorded with reasonable resolution using inexpensive data acquisition hardware. However, the change in Bragg wavelength will affect the grating reflectance at its operating wavelength and therefore also modify the shape of the output fringe patterns. Therefore, it is important to investigate the factors affecting the Bragg wavelength and its effect on the shape of output fringe patterns.

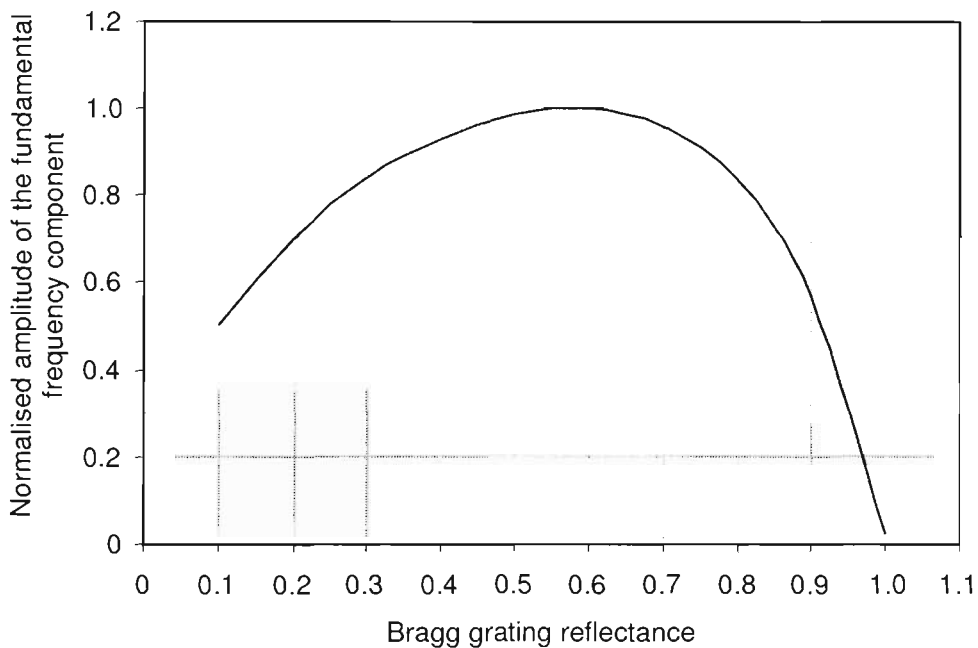


Figure 3-3: Normalised amplitude of fundamental frequency component of the Fabry-Pérot reflectances fringe pattern at various Bragg grating reflectances (R_1) with $R_2 = 0.94$.

A typical strain (ϵ) induced change¹⁴¹ in the Bragg wavelength ($\lambda_B \sim 1550$ nm) of the Bragg reflector (Figure 3-4) is

$$\Delta\lambda_B = \lambda_B \times (1 - \rho) \times \epsilon, \quad (3-9)$$

where

$\Delta\lambda_B$ = wavelength shift,

$\rho = 0.266$ (photoelastic constant).

Also, the temperature induced change in the Bragg wavelength is measured to be ~ 0.0256 nm/ $^{\circ}$ C at 1525 nm as shown in Figure 3-5. Assuming a uniform temperature gradient within a structure, the typical shift in the Bragg wavelength should be ~ 0.5 nm for a 20 $^{\circ}$ C change in the temperature of the Bragg grating¹⁴¹.

These changes in grating reflectances will affect the output fringe shape of the Fabry-Pérot sensor. Figure 3-6 shows the measured optical transmission spectrum of a typical Bragg grating fabricated during this investigation. This shows a calculation of the change in the effective reflectances due to the temperature induced shift in the Bragg wavelength. The changed central wavelength, as shown in Figure 3-6, will increase transmission of the IFBG to 75%.

To overcome these effects broadband gratings were fabricated, instead, so that reflectances over a wavelength range of ~ 1 nm would be identical. Care was taken to maintain the grating reflectances in the range of 30-70% during IFBG fabrication. The theoretical plots of the Fabry-Pérot output fringes as a function of three grating reflectances (30, 40 and 50%) are shown in Figure 3-7. It can be seen that the fringe pattern does not change significantly with change in the Bragg grating reflectances.

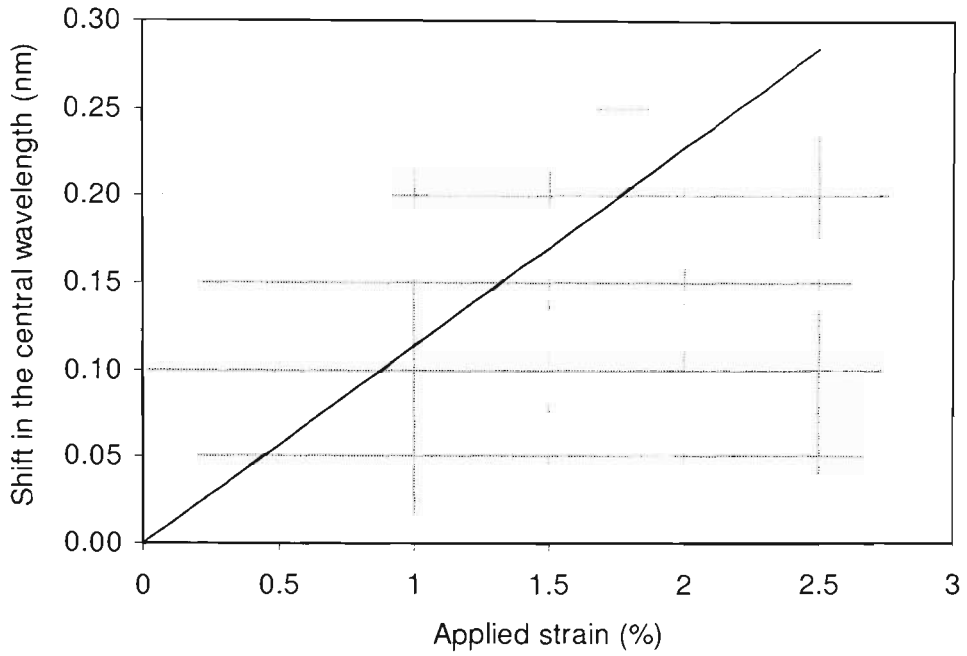


Figure 3-4: Straight line fit to the measured shift in the Bragg wavelength as a function of applied strain with wavelength-strain sensitivity of $1.15 \text{ pm}/\mu\epsilon$ at $\sim 1550 \text{ nm}$ illumination¹⁴¹.

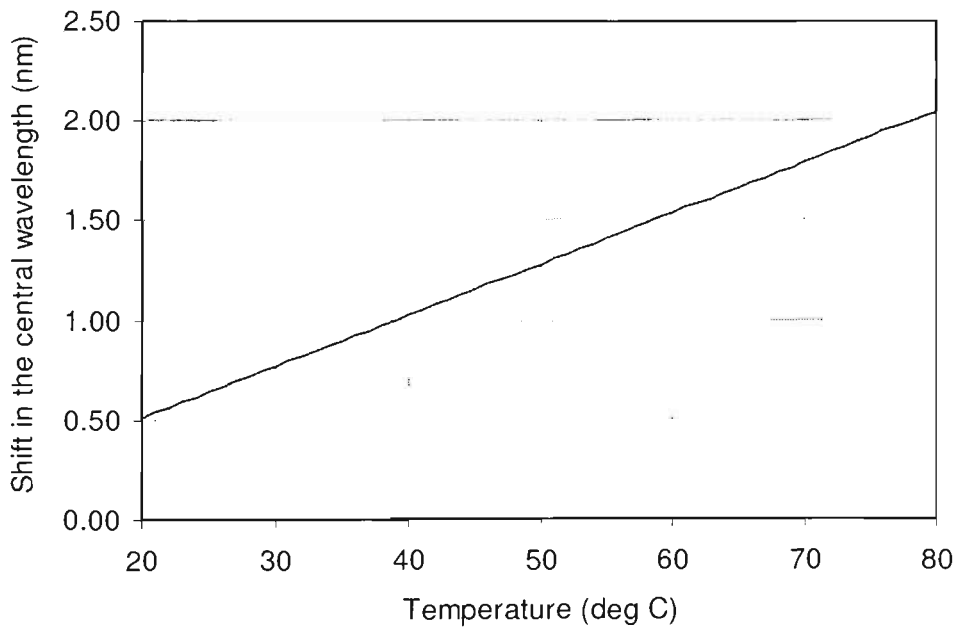


Figure 3-5: Straight line fit to the measured shift in the Bragg wavelength as a function of temperature at $\sim 1525 \text{ nm}$ illumination¹⁴¹.

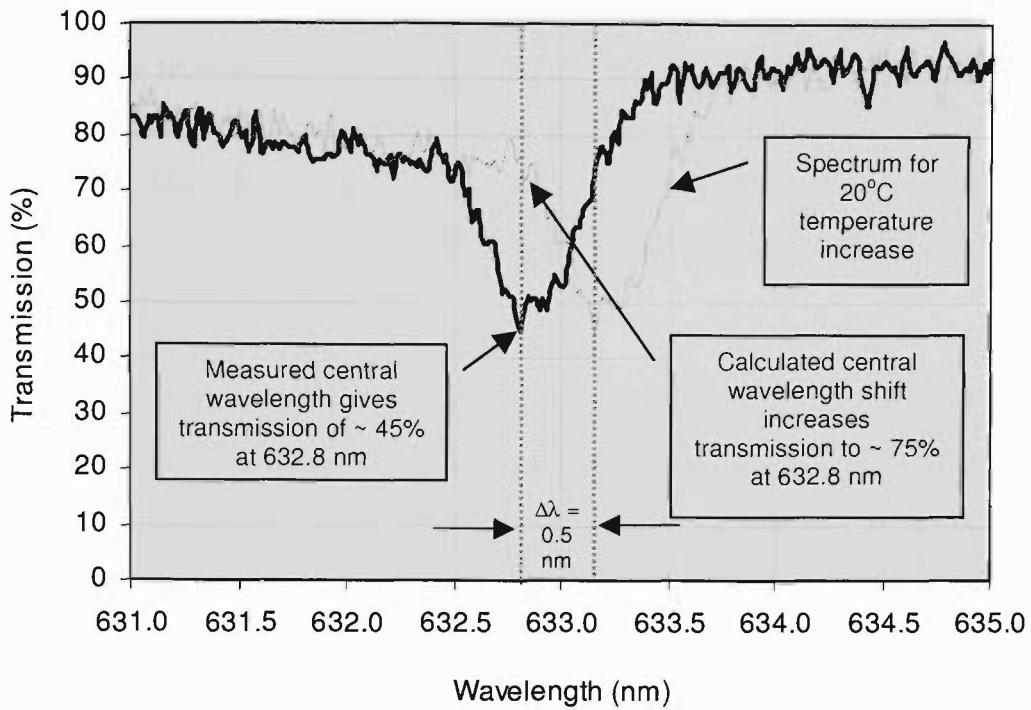


Figure 3-6: Determination of the change in the Bragg grating transmittance at 632.8 nm when the temperature rises by 20 °C, based on the transmission spectrum of a typical grating fabricated during this research.

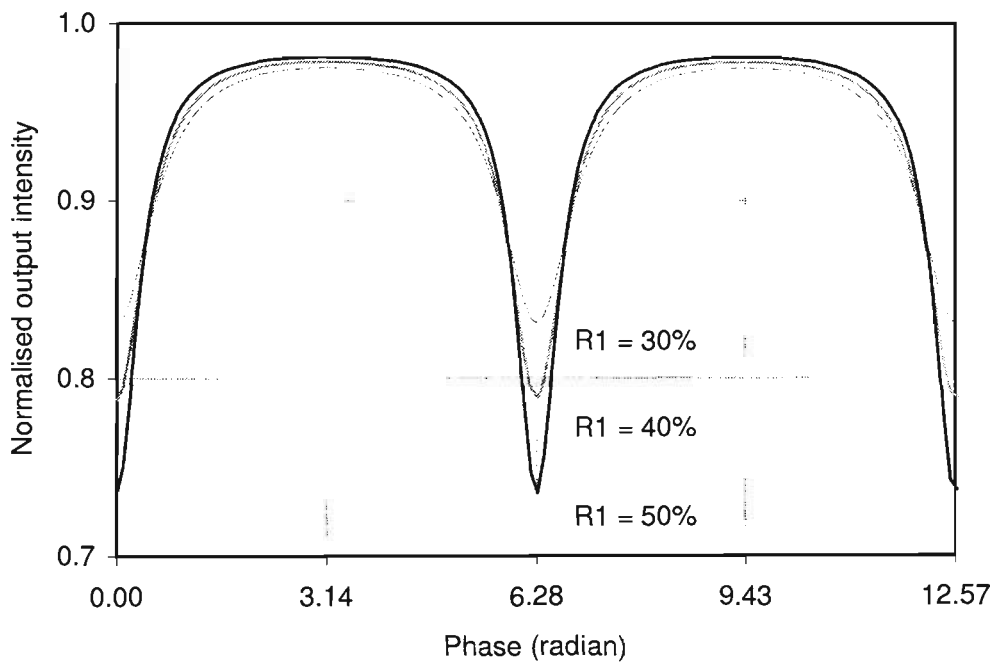


Figure 3-7: Theoretical output of asymmetric fibre Fabry-Pérot interferometer with various mirror reflectances (R_1 = reflectance of IFBG and R_2 = 94%, reflectance of the gold coating).

3.6 IFBG Fabrication

One of the key technologies in this project are in-fibre Bragg gratings (IFBG), as reviewed in Section 2.4, as one end of the optical cavity in the fibre Fabry-Pérot interferometer. This project required a number of IFBG reflectors to produce FFPI sensing elements with lengths around 0.3 metre (laboratory sensing elements) and 4 metres (field sensing elements).

These gratings were written using light from a Spectra Physics MOPO[®] (“Master Optical Parametric Oscillator”) laser pumped by the frequency quadrupled pulsed (10 Hz) Quanta Ray GCR Series Nd:YAG laser source which uses a pair of KD*P (Potassium Di-Deuterium Phosphate) crystals. The UV (245 nm) light was produced by frequency doubling using BBO crystals illuminated by the output of the MOPO laser, whose output was tuned to 490 nm. The UV beam produced was collimated via a telescope, and a cylindrical lens was used to focus the UV light into the fibre from the side. (A section of the fibre’s protective acrylate jacket was removed to facilitate writing.)

Standard optical fibres (Corning single mode at 632.8 nm) were photosensitised by subjecting them to a high-pressure hydrogen atmosphere for 24-48 hours at around 60 °C. The in-fibre Bragg gratings produced for this project were *broadband* reflectors centred at 632.8 nm with reflection bandwidths of around ~ 1 nm, and written using a prism interferometer⁹⁴ with UV light at 245 nm as illustrated in Figure 3-8. Interference between two beams, reflected from and refracted through a UV-rated quartz prism, produced a periodic intensity pattern along the fibre axis, inducing the necessary periodic refractive index changes in the fibre to create the Bragg grating. The relationship between the periodicity of the interference maxima (Λ) and the angle of intersection between the two interfering beams is given by

$$\Lambda = \frac{\lambda_{UV}}{2 n_{UV} \sin \theta}, \quad (3-10)$$

where λ_{UV} is the wavelength of the ultraviolet laser light (in this case 245 nm) and θ is the angle of the rays on the exit face of the prism.

The relationship between the Bragg wavelength ($\lambda_B = 632.8$ nm in this case) and θ is obtained using

$$\lambda_B = 2 n_{eff} \Lambda, \quad (2-10)$$

$$\text{with } \lambda_B = \frac{n_{eff} \lambda_{UV}}{n_{UV} \sin \theta}, \quad (3-11)$$

$$\text{where } \theta = \frac{\pi}{4} - \sin^{-1} \left(\frac{\sin \phi_i}{n_{UV}} \right),$$

ϕ_i is the incident angle (see schematic in Figure 3-8) of the UV radiation on the prism surface, λ_B is the Bragg wavelength, n_{eff} is the effective refractive index of the fibre (at λ_B) and n_{UV} is the prism index at the UV wavelength.

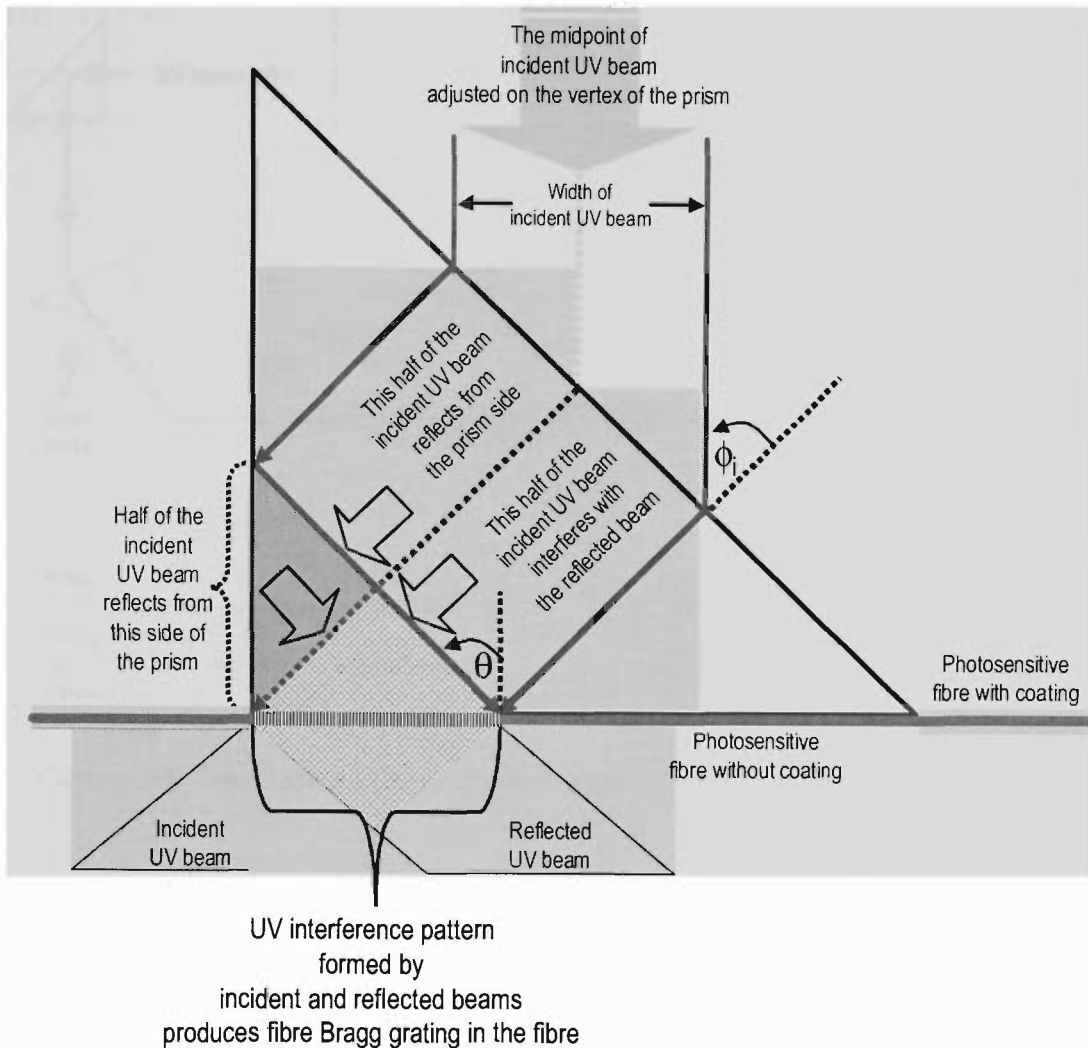


Figure 3-8: Schematic of a prism interferometer for IFBG fabrication.

Grating characteristics were monitored in real time during fabrication by measuring the transmission of a white light spectrum with an optical spectrum analyser (OSA). The grating spectrum is fine-tuned by adjusting the prism angle (ϕ_i) with respect to the incident UV beam. Figure 3-9 illustrates the successful IFBG fabrication system developed and Figure 3-10 shows a typical transmission spectrum of a broadband fibre Bragg grating.

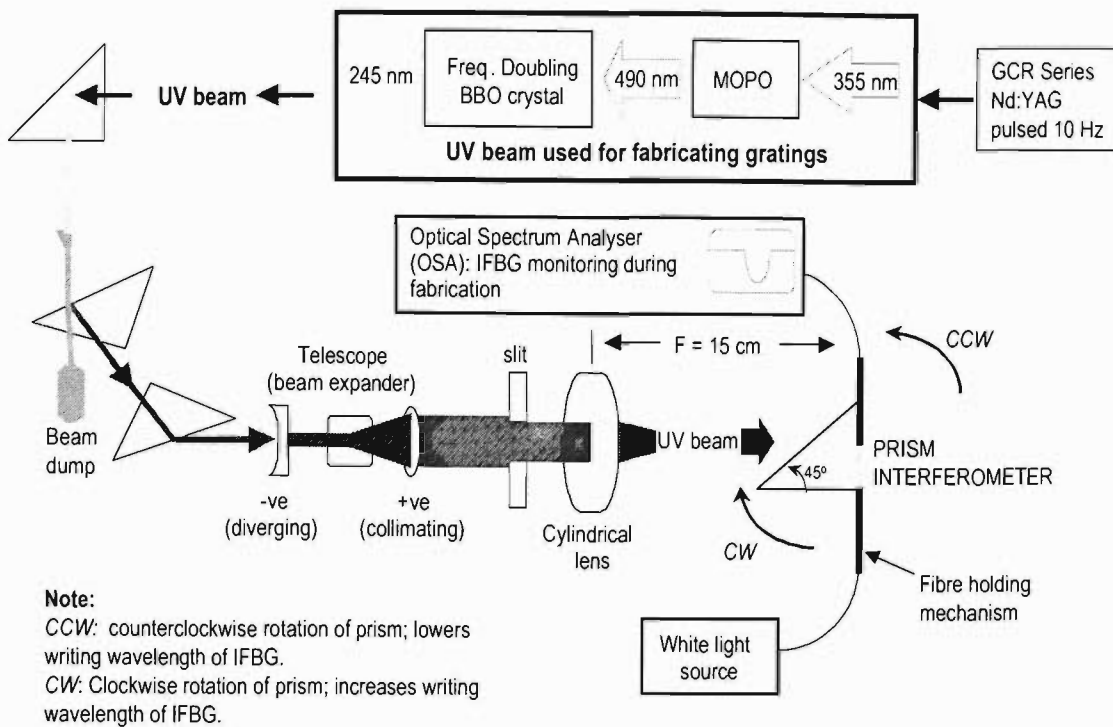


Figure 3-9: Experimental arrangement used for fabricating broadband IFBGs.

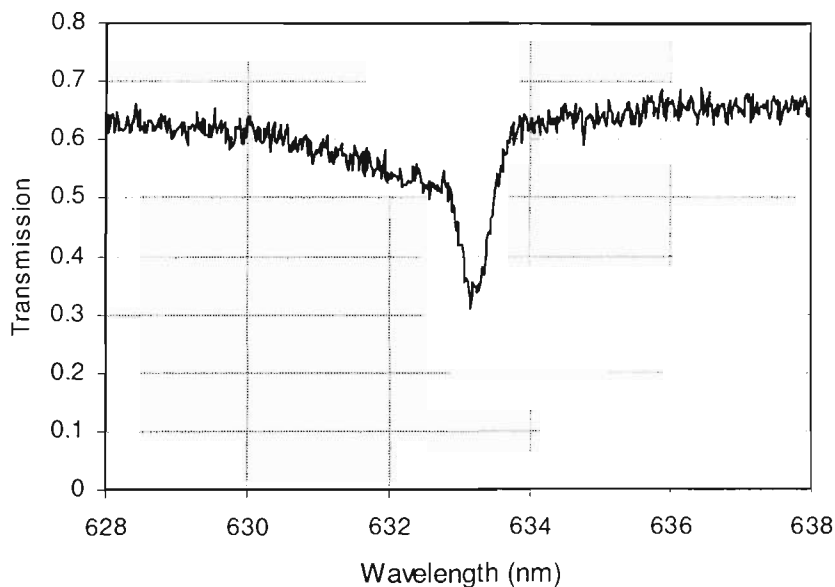


Figure 3-10: Measured transmission spectrum of a typical fibre Bragg grating, illuminated with a broadband light source. The reflection bandwidth is ~ 1 nm.

3.7 Estimation of the Sensor Output

The sensor performance depends on the mechanism through which the induced perturbations propagate through the structure and produce changes in the length of the embedded sensing arm. Preliminary sensor trials were carried out under laboratory conditions using a 300 mm long sensing element embedded in an aluminium beam (as described in Section 4.2). The total number of FFPI output fringes was estimated based on a three-point bending mechanism (Section 3.7.1).

The field version of this sensor consists of a 4 m sensing length embedded in the pavement. The vehicle-induced forces deform the pavement structure producing alterations in the embedded sensing length to generate output fringes. The fibre stretching mechanism has been hypothesised and the total fringe count for a typical pavement structure was estimated.

3.7.1. Fringe Count Estimation based on the Bending Mechanism

This section estimates the viability of an embedded sensor for general structural strain sensing applications by calculating its response to the strains induced when the test structure is bent.

Consider a test structure (beam) supported by two mounts separated by a distance L (Figure 3-11). The beam is subjected to bending in the vertical direction by applying a force at the mid-point between the two supports. The neutral axis, passing through the centre of the cross-section, does not experience any strains due to bending. In the region between the neutral axis and the convex surface the bending strain is tensile. Hence, in Figure 3-11, the bending strain between the neutral axis and the concave surface is compressive and at the beam mid-span is given by Equation (3-12)^{142,143},

$$\varepsilon = \frac{3r}{L^2} y, \quad (3-12)$$

where

r = distance of strain field from the neutral axis,

y = central deformation and

L = length between the supporting mounts.

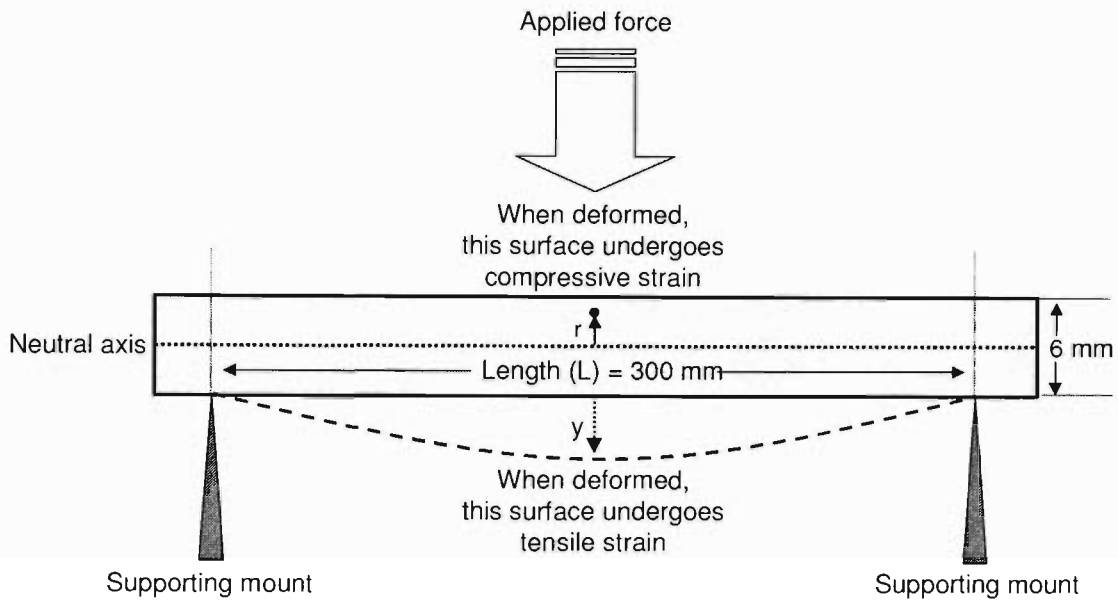


Figure 3-11: Three-point bending geometry for a beam subjected to an external load.

Equation (3-12) suggests that the theoretical strain is a linear function of the central deformation at various sensing depths. The estimated maximum error in Equation (3-12) is 5%¹⁴³.

Thus, the surface strain, at the top of the beam (i.e. at $r = 3$ mm) due to a $y = 1$ mm central deformation of the test beam can be calculated from Equation (3-12) as 10^{-4} strain. On the other hand, the underside surface of the beam undergoes tensile strain that can be calculated by substituting $r = -3$ mm in Equation (3-12). Moreover, under such strain, the surface mounted FFPI sensing length of $L = 0.3$ m should change by $\Delta L = (\varepsilon \times L) = (0.3 \times 10^{-4}) = 30 \mu\text{m}$, and should output ~ 110 optical fringes (since in Equation (3-7) it was shown that a $\sim 0.273 \mu\text{m}$ change in sensing length produces 1 fringe).

The relaxation of the beam will induce a similar number of fringes, with extra fringes possible due to dynamic effects such as “ringing” in the structure. Thus, an applied loading cycle will result in two sets of fringe groups. The first set of fringes represents the load increment (deformation) and the second set of fringes represents the load decrement (relaxation) of the structure. Moreover, the number of fringes occurring per second (fringe frequency) provides the rate at which the structure is being deformed or relaxed.

3.7.2. Effect of Loading Trends on the Sensor Output

As discussed in Section 3.7.1, when a structure undergoes compression, an embedded FFPI sensor within the structure outputs a number of fringes roughly proportional to applied structural compression. In the case of a road pavement structure, ideally, a single axle should produce a deformation-relaxation function that may be represented as shown in Figure 3-12(a). The FFPI should output two separate fringe groups for applied deformation and relaxation. Assuming that the magnitude of the applied deformation is equal to the magnitude of the relaxation, the total number of output fringes counted during the deformation should be equal to the total number of fringes counted during relaxation. Also the sum of all the output fringes, counting both the deformation and the relaxation should be linearly proportional to the applied structural deformation.

Moreover, two closely spaced axles (Figure 3-12(b)) induce two successive deformations and the second axle induces another deformation immediately after the first deformation. The associated effect on the FFPI output fringe pattern is also shown in Figure 3-12(b). Due to overlapping, fringe groups 1 and 4 contains more fringes than fringe groups 2 and 3. This indicates that two closely spaced axles may lead to fringe-loss in the total fringe count approach. An investigation of fringe loss as a function of axle spacing is provided in Chapter 5.

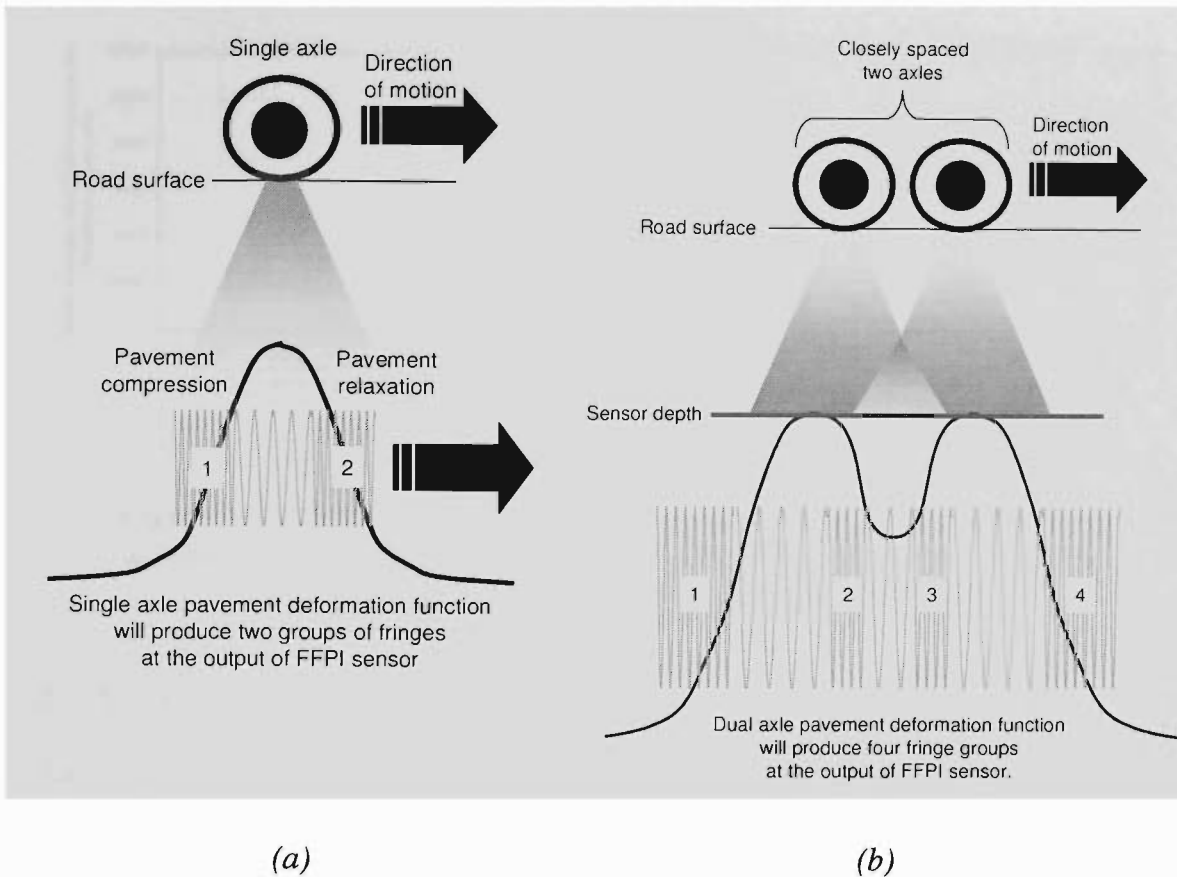


Figure 3-12: (a) Schematic of single axle pavement deformation function, (b) Overlapping of two closely spaced single axes, with numbered fringe groups.

Assuming that each axle induces a *peak-function* pavement deformation profile, two axles separated by some distance may be represented by the overall deformation profile shown in Figure 3-13(a). The peak width depends on the relaxation properties of pavement material¹⁴⁴. The smaller peak represents an axle weighing ~ 5000 kg (5 tonne) and the taller peak represents the other axle weighing ~ 10 000 kg (10 tonne). The distance between the two individual functions was adjusted to avoid any overlapping. The two individual axle functions overlap, when the distance between two axles was reduced to ~ 7 m (Figure 3-13(b)). This analysis suggests that due to the overlapping deformation profiles it may be necessary to add axle-separation-dependent fringe count correction to the total fringe count. More analysis based on the data recorded during field trials is provided in Chapter 5.

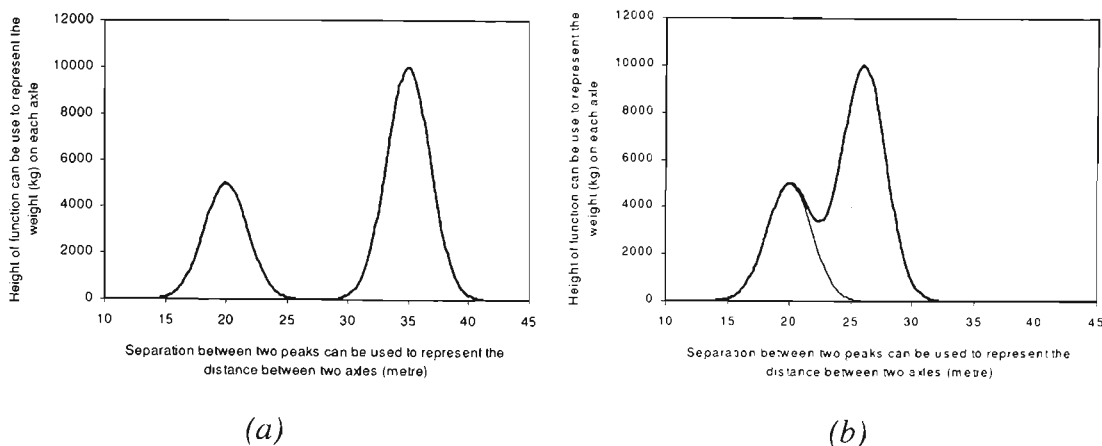


Figure 3-13: Graphical depiction showing interaction of two single-axle deformation profiles as a function of axle separation. (a) Non-interacting deformation profiles (b) Interacting deformation profiles.

3.7.3. Pavement-Vehicle Dynamics

As discussed in Section 2.5.4, significant limitations in the accuracy of WIM systems are imposed by the dynamic nature of loads applied by moving trucks on the pavement. In the case of embedded (in-road) WIM systems, the calibration process depends on understanding the vehicle-pavement behavior and the pavement-sensor reaction.

The investigation of vehicle-pavement dynamics involves research on the characteristics of pavement response in terms of stresses, strain and deflections under vehicular loads. The studies of tyre-pavement interactions under the action of moving vehicular loads mainly involve analysis of (a) road roughness, (b) vehicle speed, and (c) truck suspension systems^{116,145}. Theoretical analysis also requires either a coupled vehicle-pavement model or independent vehicle and pavement models. A variety of pavement dynamic and vehicle dynamic models have been suggested and studied^{118,119,146}. Moreover, comprehensive reviews of various mechanistic models and their limitations have been published^{120,121,147}. These factors increase the complexities in calibrating embedded (in-road) WIM systems.

Primarily, all in-road sensors measure the short-term elastic pavement deformation that provides an approximate measure of vehicle induced loading. In most common fibre optic WIM configurations, a sensing fibre can be placed in a reasonably rugged

assembly prior to its placement. The assembly can be embedded into the pavement structure so that it responds approximately linearly to the pavement deformations in an optimum way. As discussed in Section 3.4 and shown in Figure 3-14, the embedded assembly in this research is oriented perpendicular to the direction of the moving vehicles. This allows integration of the effect of vehicle-induced deflection over the road width. In such an installation, it is important to note that, despite the complexities involved in calibration, embedded (in-road) WIM sensors respond to either deflection propagated through coupled pavement layers (Figure 3-14)¹⁴⁸ down to the installation depth, or the squashing of pavement layers and the resultant lateral expansion depending on the Poisson's ratio of the material. Section 3.7.1 provided a rough estimation of the sensor output for the former case, and the later case is discussed in Section 3.7.4.

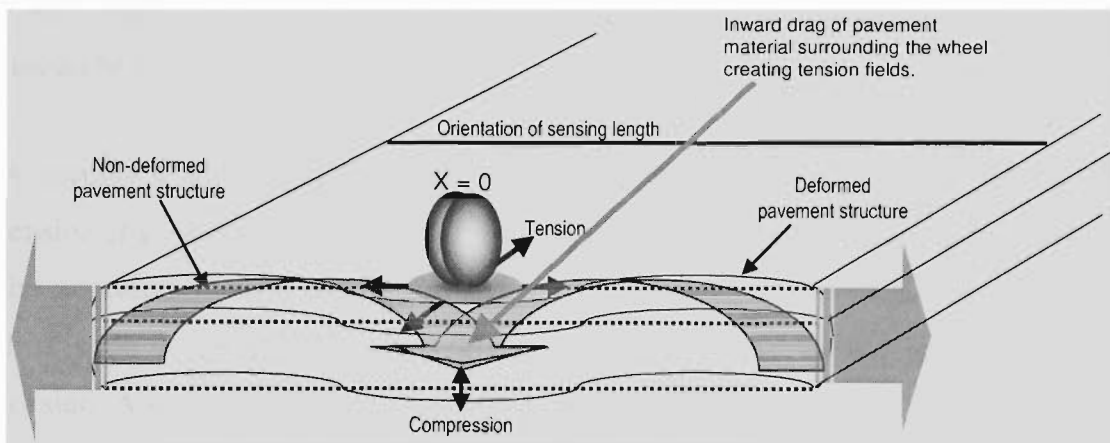


Figure 3-14: Deformation of the surface and the unbound layer of the pavement structure (half lane) showing directions of the strains¹⁴⁸.

3.7.4. Fringe Count Estimation based on Pavement Response

Pavement loading depends on the stresses induced by the contact area of each tyre of an axle. This is modeled as a circular region of applied load. The pavement surface at $x = 0$ compresses vertically downwards stretching the surrounding pavement material inwards under the wheel and induces tension as shown in Figure 3-14.

Figure 3-15 shows results from a finite element stress (horizontal) analysis¹⁴⁹ of a loaded (at $x = 0$) pavement surface near the asphalt concrete (AC) layer. Note that other stress fields, such as vertical stresses, shear stresses, torsions, etc. affecting

pavement material, were not included in the investigation. The negative and positive stress field lines, shown in Figure 3-15, indicate that the AC pavement layer undergoes compression and tension simultaneously that varies as a function of depth. The tension and compression at the surface layer gradually decreases at greater depths and after ~ 50 mm depth the compression reduces to zero. Indeed, tension is the dominant effect in the pavement structure that propagates to the layers below ~ 50 mm.

In the case of multi-axle loading, each axle as shown in Figure 3-15, induces its own characteristic tension/compression fields and depending on the axle separation, interacting combinations of these fields produces gross stress fields. Typical horizontal tension and compression fields in asphalt concrete (AC) layers resulting from multi-axle loading of pavement material were investigated by other researchers¹⁴⁹ (Figure 3-16).

According to this trend, the layers should have negligible compression and reduced tension at greater depths. Thus, the fibre sensing element embedded ~ 800 mm below the pavement surface would experience an attenuated version of the vertical stress profile shown in Figure 3-16 where compression would be negligible with finite tension. Also these effects are dynamic; the stress fields suffer overall reduction and non-linearity that results in a complex response function. These attenuated stress fields would have the net effect of stretching the fibre and the change would be approximately proportional to the applied loads, depending on the properties of the pavement material.

However, as the analysis above is complex a simple approach, in which the pavement is considered as an ideal material with a known Poisson's ratio, is used to estimate the total output fringe counts.

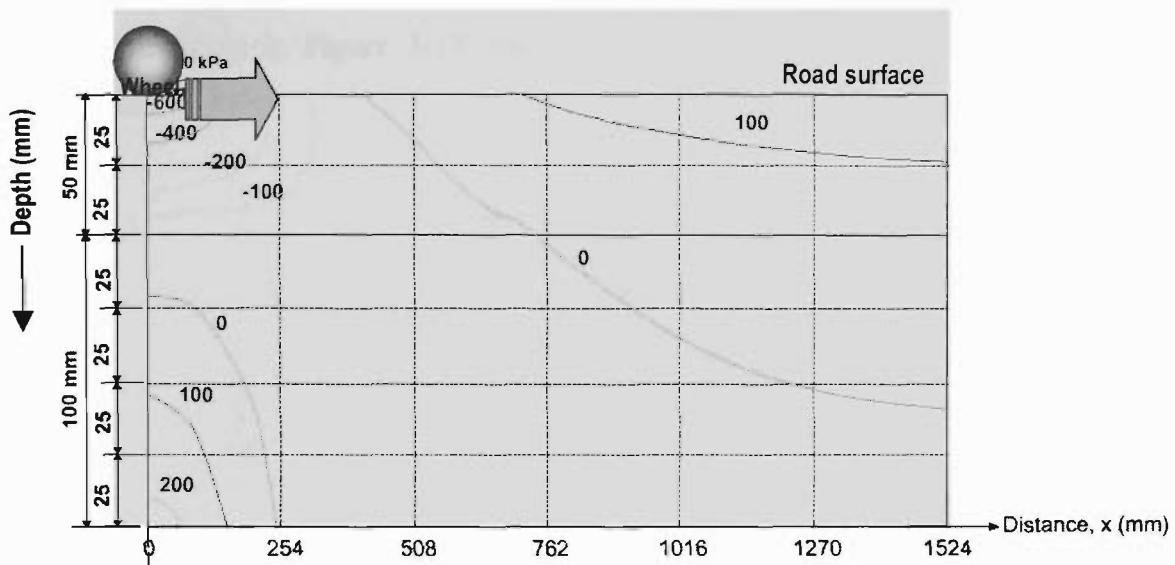


Figure 3-15: Horizontal stress distribution in AC layer calculated using a finite element stress analysis method. The figure also shows tensile and compressive stress fields in microstrains¹⁴⁹.

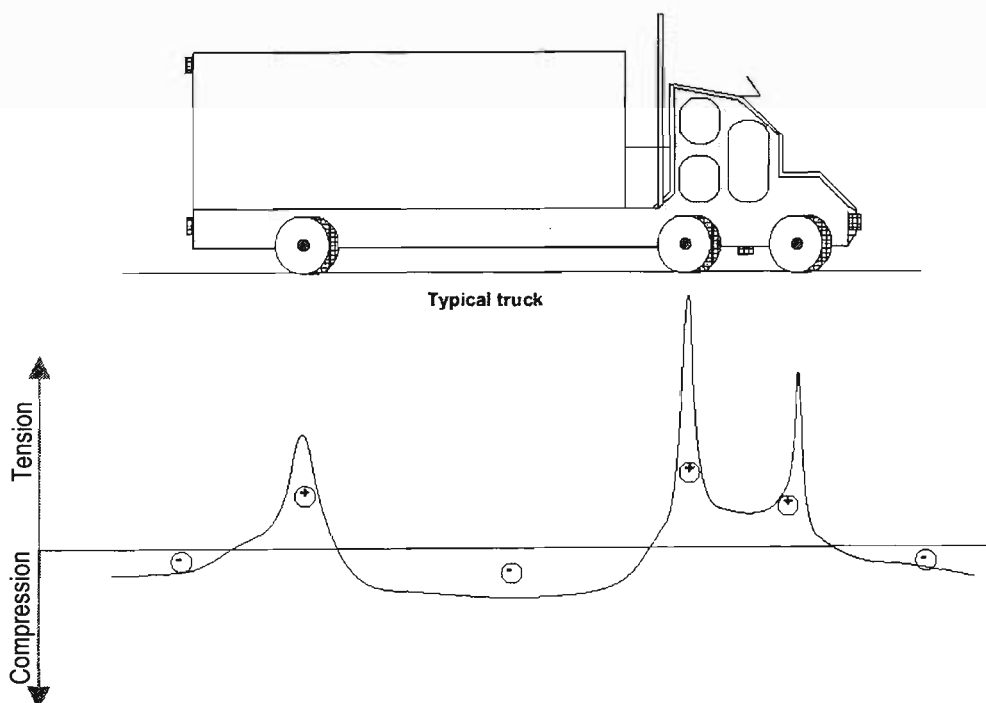


Figure 3-16: Horizontal stress distribution in AC layer under action of multi-axle loading showing combination of tension and compression profile at the bottom of the asphalt layer¹⁴⁹.

A material loaded in one direction will undergo strain perpendicular (transverse strain) to the direction of the applied load as well as parallel (longitudinal strain or

axial strain) to it. Figure 3-17 illustrates the application of Poisson's ratio to this situation.

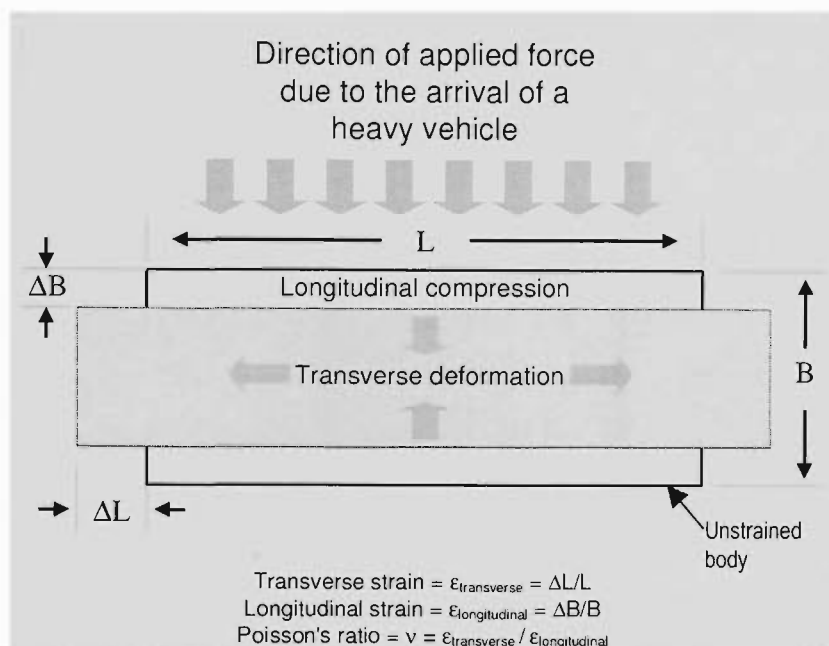


Figure 3-17: Application of Poisson's ratio, showing how the shape of the pavement will be affected by an applied force.

Poisson's ratio is an important parameter for the dynamic characterisation of pavement material. Results of modelling in which, the pavement material is treated as viscoelastic, and Poisson's ratio decreases linearly with loading frequency and temperature are shown in Figure 3-18. Although this graph shows variations of Poisson's ratio and temperature, the authors noted that, in elastic analyses, energy considerations require that the Poisson's ratio be between 0 and $\frac{1}{2}$, and concluded that the Poisson's ratio variation shown in this figure was valid between 0.01 and 0.495 only^{150, 152}. Therefore, for the modelling in this thesis, the Poisson's ratio variations were assumed to be in the range of 0.01 to 0.4. Moreover, in this section, the value of Poisson's ratio used for estimating the total number of fringes was assumed to be 0.4.

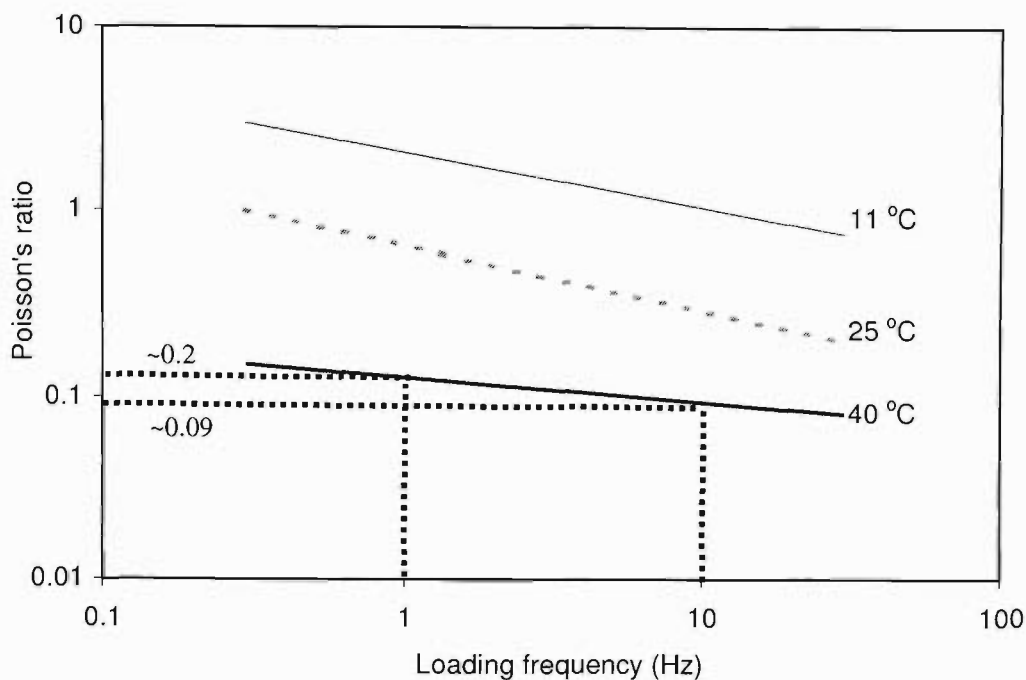


Figure 3-18: Variations in Poisson's ratio of typical pavement material as a function of loading frequency and temperature¹⁵⁰. The authors noted that, the values of Poisson's ratio are valid between 0.01 and 0.495 only.

For the present case, the length of the sensor (L) is 4 m and the depth of the sensor (B) is ~ 800 mm. The pavement surface deforms approximately on the submillimetre level¹⁵³ due to vehicular loads (in this case assuming the range of $\Delta B \approx 0.01$ to 0.09 mm). The point sensors embedded ~ 800 mm below the pavement surface, into the subgrade, experience an average vertical strain of $\sim 250 \mu\epsilon$ ¹⁵⁰. Note that the point sensor readings are highly susceptible to the lateral position of the transducer beneath the road surface. Also, irregular vehicular loads on the pavement surface increase the complexity in quantifying the parameter, ΔB . However, for a rough estimation, assuming ΔB is in the range of 0.01 to 0.09 mm due to the arrival of the vehicle axle, the longitudinal strain is calculated using $\epsilon_{\text{longitudinal}} = \Delta B/B = \Delta B \text{ mm} / 800 \text{ mm}$. Now by knowing the sensor length, L is 4 m, ΔL can be calculated as follows:

$$\nu = \frac{\epsilon_{\text{transverse}}}{\epsilon_{\text{longitudinal}}} = \frac{\Delta L/L}{\Delta B/B} \quad (3-13)$$

$$\Delta L = \left(\frac{v \times \Delta B \times L}{B} \right) = \left(\frac{0.4 \times \Delta B \times 4m}{800mm} \right) \quad (3-14)$$

Hence, by substituting ΔB in the range 0.01 to 0.09 mm in Equation (3-14),

$$\Delta L = 20 - 180 \mu\text{m}.$$

By substituting above values of ΔL in Equation (3-7), the total number of fringes can be estimated in the range of ~ 37 to 329.

This estimated number of fringes depends on the transverse deformation of the pavement material. It is also important to note that this estimation of total fringe counts also depends on the temperature, loading frequency and Poisson's ratio of the pavement material. As a result of seasonal changes, water content in the pavement material will also affect the pavement response.

For example, consider the Poisson's ratio trend at 40 °C shown in Figure 3-18. A variation from 1 to 10 Hz of loading frequency changes Poisson's ratio from ~ 0.09 to 0.2 and results in a significant change in the estimation of the total number of fringes from ~ 21 to ~ 46 for any deformation. These variations may mandate a dynamic calibration system for the sensor, but the number of total fringes should be proportional to the applied deformation for a given Poisson's ratio irrespective of slow changes in the Poisson's ratio due the prevailing environmental conditions.

3.7.5. Fringe Frequency Estimation

The Fabry-Pérot interferometer produces optical "fringes" as the sensing element is stretched, where the observed fringe rate is proportional to the rate of change of length (or strain) in the sensing fibre as illustrated by the example in Figure 3-19. Consider a vehicle moving at 90 km/h (25 m/s). Each axle of this vehicle will remain on the sensor for 1/25th of a second indicating that an event of pavement deformation and relaxation has a frequency of 25 Hz in this particular case.

Assuming a 1 m sensor width and symmetric pavement deformation, in which the rate and amplitude of pavement deformation and relaxation are identical, and

neglecting pavement properties, then according to Section 3.7.4, the total number of fringes estimated using the Poisson's ratio principle is ~ 100 . Thus, under ideal conditions, it is necessary to determine the rate at which ~ 100 fringes should be sampled to identify an event occurring at 25 Hz with adequate resolution.

To achieve minimum resolution for an ideal sinusoidal fringe, it is necessary to acquire a minimum ~ 10 samples per fringe. This leads to the minimum sample rate of ~ 25 kHz. As the weight of an axle changes, more fringes are expected within the same time frame. Therefore, a sampling rate of ~ 50 kHz should be sufficient for acquiring these events. National Instrument's AT-MIO-16E-1 data acquisition hardware capable of a maximum sampling rate of 1 MHz was adopted for these experiments.

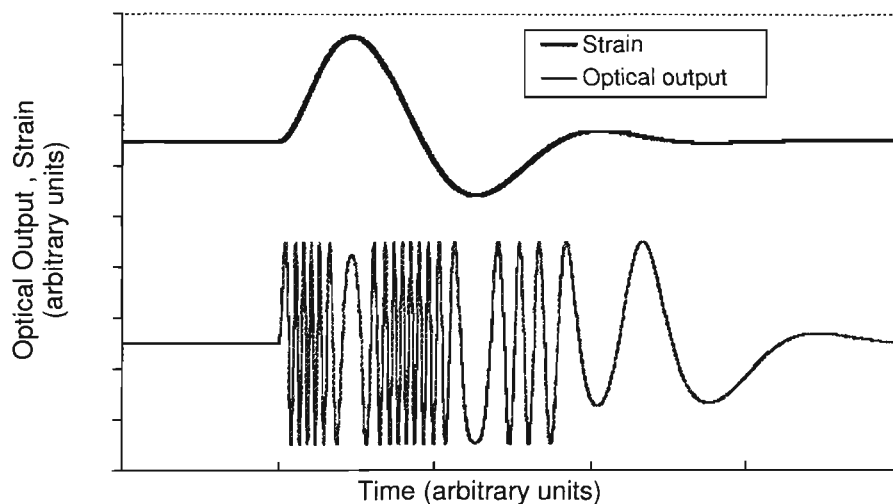


Figure 3-19: *Expected variation of the optical output of an FFPI interferometer causes by the indicated applied strain.*

The interferometric fringe patterns manifest themselves as quasi-sinusoidal variations of the output intensity in time. Random perturbations in the sensing arm of an interferometer can alter the output fringe patterns as jitter. It is possible to filter some of this high and low frequency noise by using electronic filtering circuits along with the data acquisition hardware. This simplifies the fringe analysis algorithms. However, random structural deformations capable of producing fringes in the

bandwidth of the detector will affect the sensor signal despite the electronic pre-filtering.

Fringe counting has a significant drawback - the Fabry-Pérot is insensitive to the *sense* of the change in strain (increasing or decreasing), so it is not possible to unambiguously determine changes in the absolute fibre strain in this manner. Hence, this sensor will not readily return real time strain information directly. Figure 3-20 shows the theoretical (from Equation 2-5) output of a Fabry-Pérot consisting of an IFBG for R_1 (30%) and a gold coating reflectance for R_2 (94%). This figure also illustrates the fringe pattern as compared with the fringe frequency.

However, repeatable events (as discussed in Section 3.7.2) with a characteristic strain “signature” will produce a total fringe count proportional to the applied peak load, in principle. Therefore, in the interests of simplicity, the “total fringe count” approach was investigated to determine whether or not a reliable relationship exists between peak strains in transient load “events” and the number of fringes observed during these events.

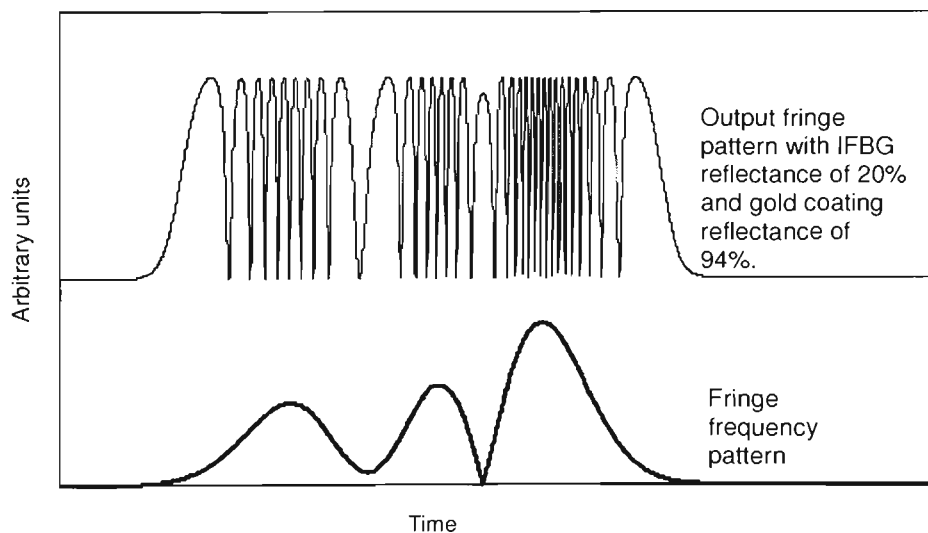


Figure 3-20: Theoretical FFPI output fringe pattern and its fringe-frequency.

3.7.6. Method of Calculating Fringe Frequency

A Fourier transform is one option to consider for transforming fringe data into frequency information within a defined time span. In this particular application, to

identify variations in the fringe frequency components in the time domain, it is necessary to calculate Fourier transforms over many overlapping sets of data points. Each Fourier transform will provide information about frequency components and associated powers present in that data set over the time interval defined by the windowing function. The “spectral view” of a data set (presented in Figure 3-21), measured during primary field trials is shown in Figure 3-22. This particular plot was obtained from CoolEdit96 software developed by Syntrillium Software Corporation (using the “Blackmann windowing function”). This enables the display of a waveform by its frequency components, and is useful for determining common frequencies in the data set. The abundant frequencies in the measured data set are indicated in Figure 3-22 using the darker shades. The resolution of the spectra is limited by the time-window.

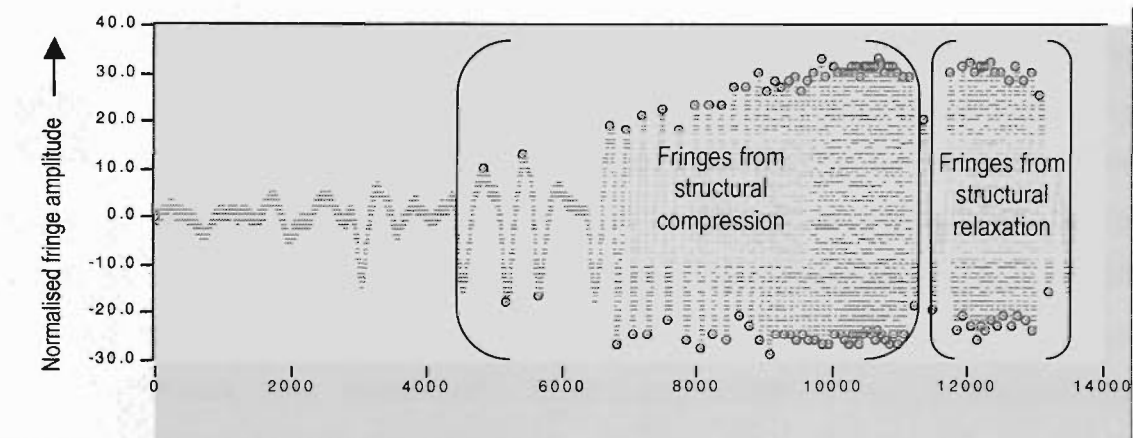


Figure 3-21: Part of some measured truck data showing FFPI output fringes as detected by the algorithm for a single cycle having unequal compression and relaxation events.

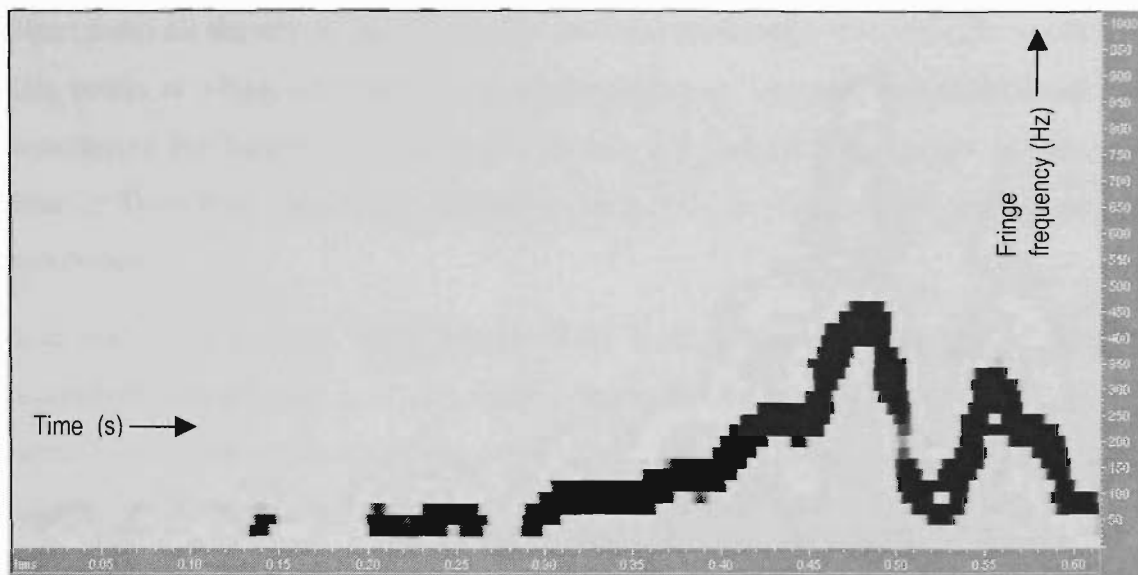


Figure 3-22: Spectral view of the output fringe data presented in Figure 3-21 showing various frequency components present in the waveform.

By choosing an appropriate windowing function, it is possible to enhance the ability of the Fourier analysis to extract spectral details from the signal with better resolution. However, the property of the windowing function defines the trade-off between frequency and time domain resolutions. Hence, for a given data set, the windowing function characteristics can be chosen either to recover all time domain information with zero frequency domain resolution or to recover frequency domain details with zero time resolution¹⁵⁴. It is also possible to have a situation that provides 50% time and 50% frequency domain information at a cost of 50% reduction in the frequency and time resolution respectively. Therefore it is important to define an appropriate windowing function for processing a given fringe data set. Also, there may be more than one windowing function/s required to process a single data set. This will lead to the design of a filter bank that can be used to process that particular data set only and requires the design of another filter bank for processing another data set. As output fringe-frequency variations depend on elastic properties of the structure, it is likely to require more than one windowing functions for processing the fringe data from other sensors. This complicates the real-time data processing algorithm.

Apart from all the above issues, Fourier analysis produced a discrete (2^n) number of data points at a time and determined all the frequency components in the signal. By considering the number of data points in each file, for such an amount of data, the Fourier Transform algorithm required a long time to calculate all the frequency components.

It is important to note, from Figure 3-19, that the fringe frequency is directly proportional to the rate at which applied strain varies. Therefore monitoring of the deviations in the fringe frequency provides estimation of rapidly varying (dynamic) applied strain profiles. It is possible to process every component of the fringe frequency to understand the minor details related to the structural strain fields using FFT. However, as the main interest was approximate strain profiles only, it was decided to monitor the fundamental frequency component in each data set; a much simpler task than processing all frequency components. An algorithm developed for retrieving such information is explained in Section 4.3.

3.8 Summary

This chapter provided details of the development of a fibre Fabry-Pérot sensor for generic distributed structural sensing applications. Theoretically, a $\sim 0.268 \mu\text{m}$ change in the sensing length produces a single fringe at the sensor output. Hence a rough estimation of an applied strain can be estimated by counting the total number of output fringes. The effect of variations in the frequency and amplitude of the laser source on the FFPI output was estimated. This assisted the selection of the appropriate source module for the sensor system.

The shape of FFPI output fringes depends on the reflectances of the end mirrors of an optical cavity. Therefore assuming an end-mirror coating of reflectance 94%, appropriate mirror reflectances of the fibre grating were estimated to be in the range of 30-70%. This will allow data acquisition hardware to sample each fringe with reasonable resolution. The temperature and strain induced changes in the central wavelength of an in-fibre Bragg grating and its effect on the sensor output was also estimated and discussed. The use of broadband fibre gratings reduces these effects significantly. The technique of producing broadband fibre gratings used during this research was also discussed.

The FFPI sensor was configured to operate in the reflection-mode. The cavity mirrors were fabricated by selecting appropriate reflectance values for achieving moderate finesse and reasonable fringe resolution suitable for real-time data acquisition using standard data acquisition hardware.

Total output FFPI fringes were estimated for the embedded sensing length using a three point bending mechanism approach under laboratory conditions. Around 112 fringes were estimated for an applied 1 mm deformation to the sensing length of 0.3 m. In the field version of this sensor, significant limitations in the accuracy of WIM systems are imposed by the dynamic nature of loads applied by moving trucks on the pavement. Primarily, assuming that in-road sensors measure the short-term elastic pavement deformation and provide approximate measure of vehicle induced loading, around 92 to 830 optical fringes were estimated depending on the pavement properties. The effect of change in the Poisson's ratio of the pavement material on the total fringe counts was also studied. For a vehicle traveling at ~ 25 m/s, sampling rates of around 50 kHz were calculated for acquiring FFPI output fringes with reasonable resolution. This provides the required characteristics of the data acquisition hardware.

Both examples showed the potential of this sensor for generic structural and WIM sensing applications. The single-transducer FFPI sensor response for (a) bending mechanism has been investigated under laboratory conditions by embedding the sensing element into an aluminium beam (generic structural strain sensing application) and (b) Poisson's ratio mechanism by embedding the sensing element into a pavement structure (single-transducer WIM sensing application).

CHAPTER 4

LABORATORY SENSOR: DESIGN, CONSTRUCTION AND CHARACTERISATION

4.1 Introduction

In Chapter 3 the options for a WIM sensor were considered. A decision was made in favour of a long Fabry-Pérot interferometric strain sensor based on fringe counting. This chapter considers the detailed design of the sensor, its theoretical limitation and the verification of the design issues using a short sensor in a laboratory test rig.

These practical tests involved several of these sensing elements, of length 0.3 m, bonded within grooves in a flat aluminium beam. The beam was subjected to controlled periodic lateral bending using a universal testing machine. In this way it was possible to explore the dynamic and static response of the sensor. The sensor was then evaluated against theoretical expectations of linearity, frequency response, noise concerns and repeatability. These practical issues are discussed in Section 4.4.

Note that the sensor employed in the field application is much longer, approximately 4 m. Issues of sensitivity and noise in the longer sensor are anticipated and discussed in Section 3.3.

Section 4.2 describes the design and construction of the fibre transducer and test beam and the use of a universal testing machine to supply the required deformation. The design and operation of the data acquisition and processing algorithm is discussed in Section 4.3. Section 4.4 discusses calibration of the embedded FFPI sensors based on the fringe counting technique. In addition to counting interferometric optical fringes the software effectively tracks the time derivative of the strain experienced by the sensing fibre. This information is useful for estimating the structural deformation profile.

4.2 Sensor Design

4.2.1 Transducer Construction and Sensor Assembly

The sensing element was embedded in an aluminium beam of dimensions (length $500 \times$ width $59 \times$ thickness 6 mm) that behaves elastically for central lateral deformations of up to a few millimetres. The laboratory arrangement of three point bending system

described in Section 3.7.1 is shown in more detail in Figure 4-1. Four 'U' grooves were milled along the length of the beam to allow sensors to be placed at nominal distances of 1.5 and 2.8 mm relative to the beam surface (Figure 4-2). The sensing length consisted of a jacketed fibre except for a 4 cm section of bare fibre where the in-fibre Bragg grating (near-end reflector) was written. Two, essentially identical, versions of the sensors were placed into two of the grooves, each at nominal depths of 1.5 and 2.8 mm. The grooves were then filled using Loctite S2 Metal Set with the sensing cavity positioned approximately midway along the length of the test beam. The fibre length between the structure and detector electronics was protected by a hard polymer jacket surrounded by kevlar material. The extended portion of polymer jacket and kevlar material immediately outside the structure was also glued to the structure to provide additional strength. After attachment, the beam surface was machined and polished to remove excess adhesive. A commercially available electrical strain gauge, namely a Micro-Measurements CEA-Series, was bonded to the underside surface of the aluminium beam to measure variations in the surface strain for various induced deformations.

Figure 4-3 shows the overall FFPI sensor assembly constructed for the laboratory trials.

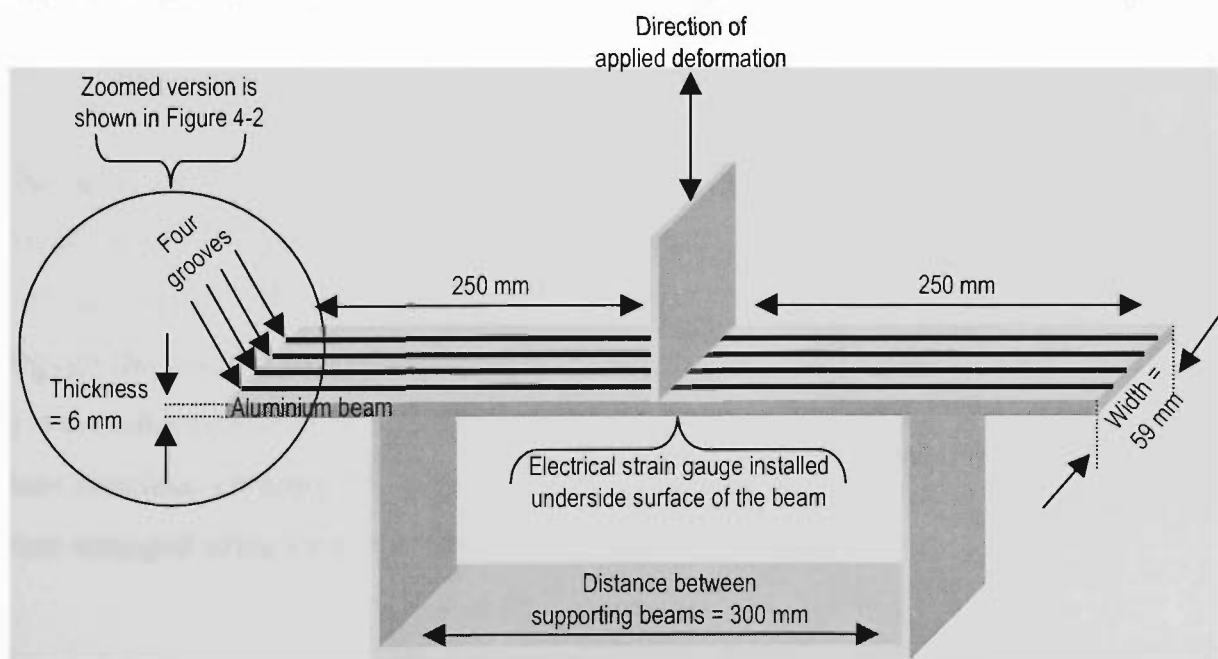


Figure 4-1: Laboratory configuration of three-point bending system showing aluminium beam, supporting mounts and direction of deformation.

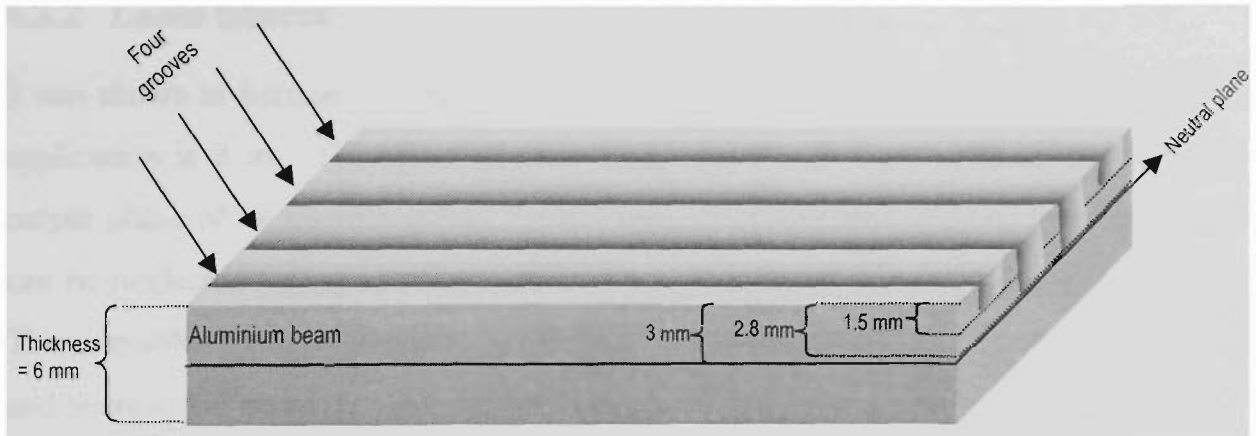


Figure 4-2: Cross-section of the aluminium beam showing position and depths of four 'U' grooves.

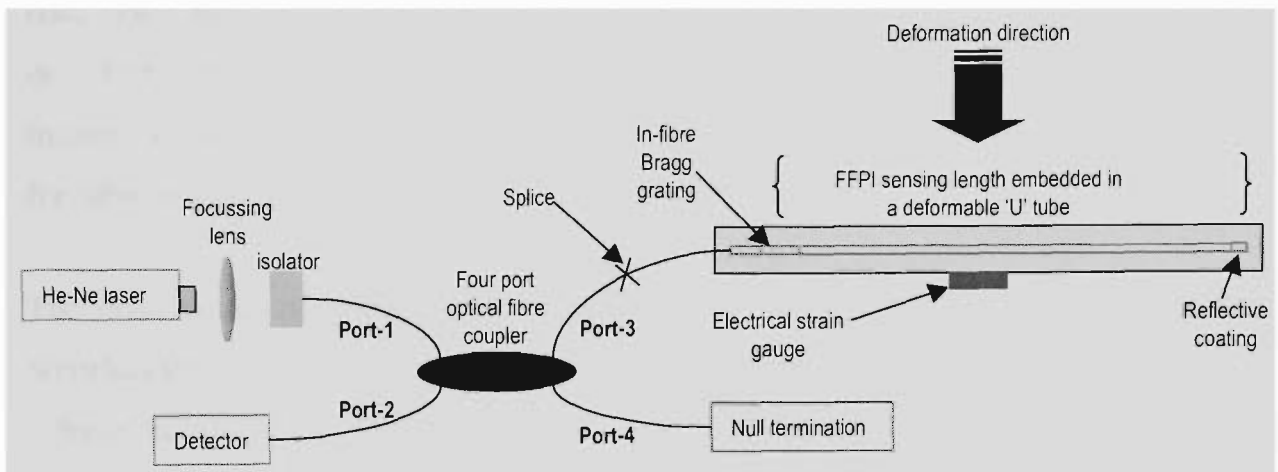


Figure 4-3: Laboratory sensor test arrangement showing optical arrangement, aluminium test beam, position of electrical strain gauge and direction of deformation.

The light was launched into the FFPI cavity via a four-port 50-50 coupler at port-1 (Figure 4-3). The FFPI optical cavity, of ~ 300 mm sensing length was spliced to port-3 of the coupler. The returning light from the interferometric sensing element passes through the coupler to a detector at port 2 (Figure 4-3). The unused coupler port (port-4) was null-terminated in index matching gel to prevent back-reflections from the air-glass interface entering the detector. The fibres and fibre components of this system were arranged using FibreNet fibre organisers.

4.2.2 Laser Source

It was shown in Section 3.3 that the minimum requirement for coherence length for this application is 8 m. The effect of laser frequency noise and amplitude noise on the output phase of an interferometric system have also been discussed in Section 3.3 and can be neglected for an interferometric system employing fringe counting techniques. The tolerable limits for frequency and amplitude noise, calculated from Equation 3-8 and Section 3-3, were shown to be ± 25 MHz and $\pm 25\%$ respectively.

In operation, this sensor system requires a portable laser module. Fibre-coupled solid-state lasers have comparatively smaller dimensions than gas lasers and reduce the size of a box containing light launching optics. However, most solid state lasers have limited coherence length (few centimetres) and so solid-state devices are suitable only for fabricating FFPI systems with smaller sensing lengths.

The most common, portable and inexpensive gas laser is the He-Ne with operating wavelength of 632.8 nm. Typical He-Ne gas lasers have a discharge tube of around 10 – 50 cm in length and 30 mm in diameter with a power output in the range of 0.5 to 2.0 mW. Other gas ion lasers such as argon, krypton, xenon or He-Ar mixture are generally larger than He-Ne lasers and even less efficient. However, they can generate a few hundreds of milliwatts (not required for this application) at various visible, near infrared and ultraviolet wavelengths.

He-Ne lasers operating in the multimode regime have linewidths of approximately 1500 MHz, and a coherence length of about 0.2 m. On the other hand, He-Ne lasers operating in a single mode and stabilised to 1 MHz have around 1500 times greater coherence length, (up to 300 m) and are suitable for use with the long fibre Fabry-Pérot cavity used in this research.

These requirements were met by a Melles Griot frequency and intensity stabilized He-Ne laser source (CDR/IEC 825-1:1993 Class: IIIa/3B¹³⁶). It has the following specifications:

Absolute frequency deviation peak to peak	1 minute	: ± 0.3 MHz
	1 hour	: ± 2.0 MHz
	8 hours	: ± 3.0 MHz,

Absolute intensity deviation	1 minute	: $\pm 0.1\%$
	1 hour	: $\pm 0.2\%$,

Frequency versus temperature dependence < $0.5 \text{ MHz}^\circ\text{C}$.

The lifetime and long term stability of this laser were not evaluated during this research. For the anticipated application it would be necessary to run the laser source 24 hrs a day for its entire life. However, as the frequency stability requirement is ± 25 MHz, no problems in this regard are anticipated.

In addition, a small percentage of back-reflected light from the interferometric configuration (particularly from splices and couplers in the system) could also generate unwanted optical frequency noise in the laser. An isolator was placed at port-1 of the coupler (Figure 4-3) to prevent these back reflections from disturbing the laser.

This sensor operates on the He-Ne wavelength of 632.8 nm. However, it is possible to adopt sources with other wavelengths by changing the specifications of optical coupler, sensing fibre and the Bragg wavelength of a grating in the sensing system. The type of optical coupler at the launching end should suit the laser wavelength. The type of sensing fibre used to fabricate the sensing length requires a single-mode fibre at the source wavelength. Thirdly, the in-fibre Bragg grating requires a change in its Bragg wavelength to match the new source wavelength. This requires significant modifications in aligning the prism interferometer that allows fabrication of the grating at a desired Bragg wavelength.

4.2.3 Detector Circuit

A high speed, low noise fibre optic PIN photodiode type OPF480 with peak response wavelength at 820 nm was used along with a suitable two stage transimpedance amplifier for this application. Two identical circuits were constructed and tested, thus allowing simultaneous comparison of two sensors. Input light was modulated at various frequencies and output voltages were recorded for each circuit. The pass-band of the receiver circuit has been set to eliminate low frequency drifts in the photocurrent associated with temperature changes and non-signal-related mechanical strain noise, and to filter out high frequency photocurrent noise above the expected signal band. Such high frequency noise is due to: acoustic pickup in the sensing element, electromagnetic interference and thermal noise in the receiver circuitry.

The bandwidth measurements of the detector electronics were carried out using a modulated 810 nm pig-tailed laser diode. The receiver output pass-band was adjusted to produce an output signal of around 1 V peak-peak. The input light was modulated at various frequencies and output voltages were measured. The measurement setup is shown in Figure 4-4. The output voltage level can be adjusted to achieve the desired signal using an appropriate gain factor in the amplifier circuit. The maximum gain of the AC amplifier (NE5532) electronics was 2200 at 10 kHz.

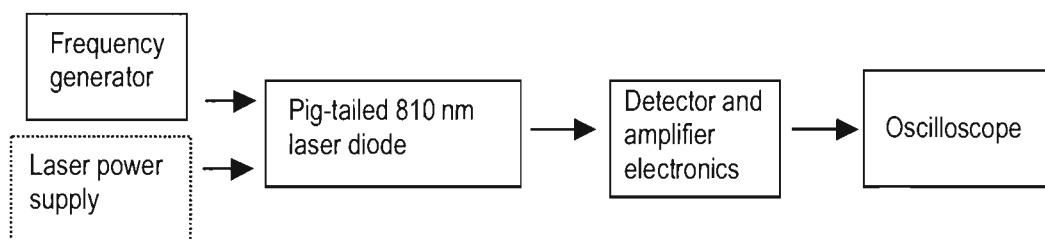


Figure 4-4: Experimental setup for determining bandwidth of detector circuit.

Figure 4-5 shows the output voltage as function of input optical modulation frequency for the detector circuit. The typical signal to noise ratio observed by the photodiode and amplifier is about 23 dB, and indicates that this noise level is negligible as compared

with the fringe amplitude. More specifically, the 3 dB roll-off frequencies are 30 Hz and 50 kHz (Figure 4-5).

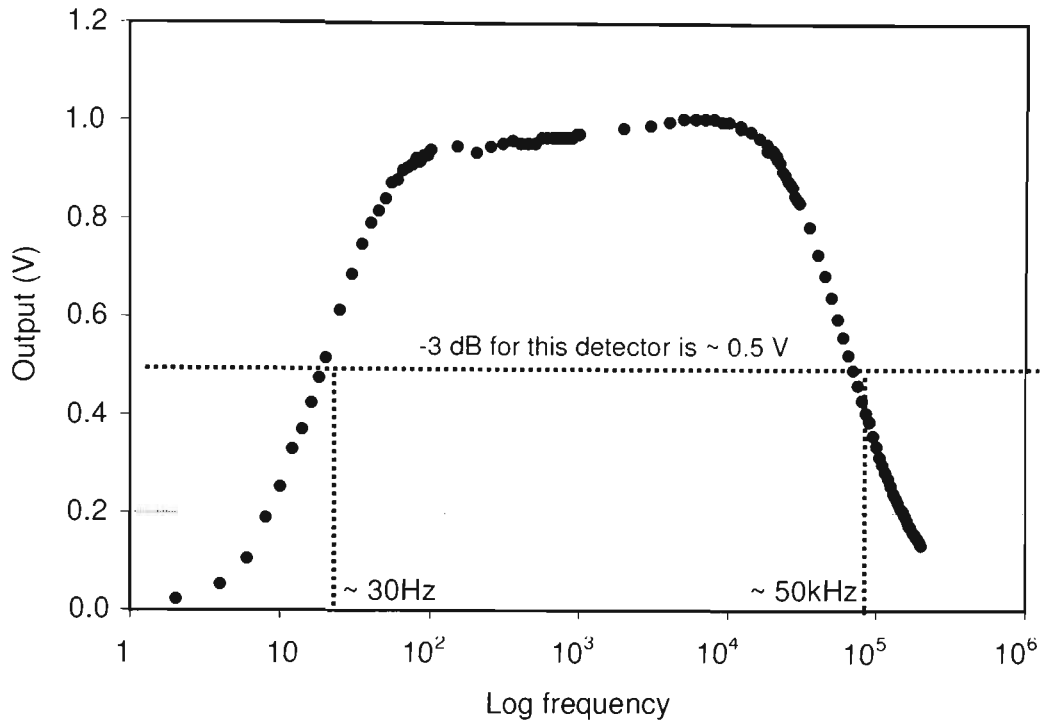


Figure 4-5: Frequency response of the optical detector circuit.

4.3 Software Development

4.3.1 Introduction

As discussed in Section 3.7, a fringe counting algorithm was to be implemented. The development of that algorithm and the attendant issues are now discussed.

An initial algorithm developed for fringe counting was based on detecting zero-crossings in the data set. However, apart from fringes, this algorithm also detects low amplitude AC electronic noise which adds to the total number of fringes. The option of using a simple peak detection algorithm was considered but that detects and counts small amplitude peaks associated with noise. However, a variant of these that combines threshold and peak-detection eliminates small amplitude noise sensitivity yielding a more faithful total fringe count. However, such algorithms detect incomplete fringes

(multiple peaked fringes, as illustrated in Figure 4-6) in the data sets which are due to undesirable mechanical perturbations (explained in Section 4.4.2.1). This problem can be eliminated by considering both positive and negative peaks or, to put it another way, one complete fringe is considered to be a peak followed by a trough. However, as discussed in Section 4.3.4, this algorithm fails to detect these double fringes with significant amplitude variations.

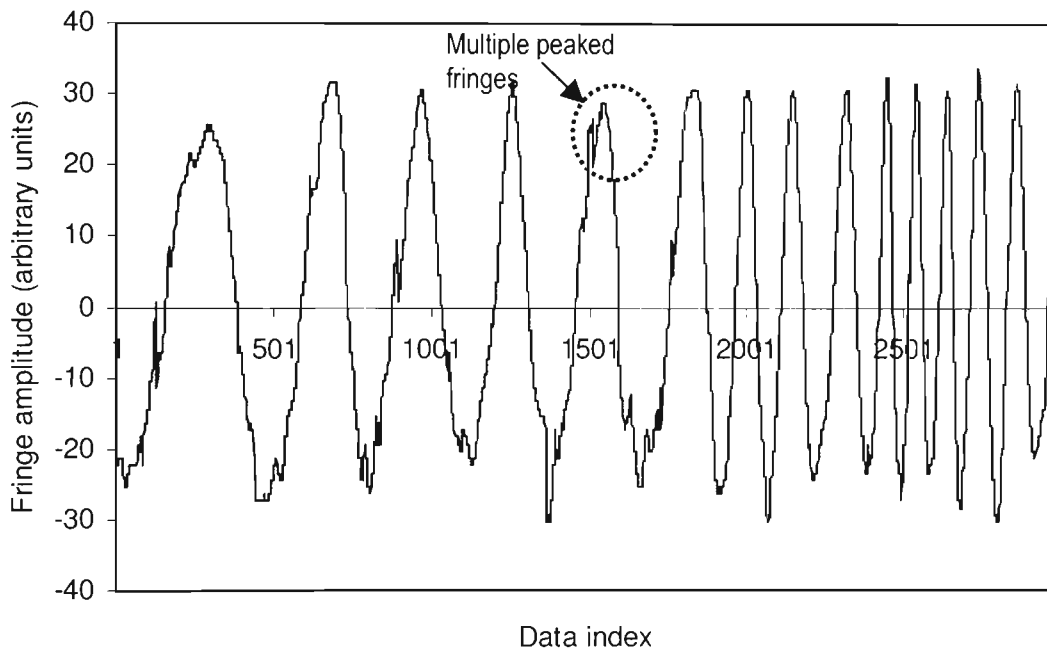


Figure 4-6: Multiple peaked fringes recorded by FFPI sensor due to induced mechanical instabilities in the test structure.

A robust fringe counting algorithm was therefore developed based on threshold and positive / negative peak detection, the data ultimately being output in a two-column text file.

(a) Data Acquisition:

National Instrument's AT-MIO-16E-1 data acquisition hardware was configured and controlled by software developed using LabView4.1. The laboratory software requires manual triggering on visual notification of an event. The program configures the hardware, acquires data and stops on the user's command. During real-time acquisition,

the program saves data in a temporary file and this is further processed and saved after the acquisition stops. The software automatically generates date-time stamped filenames for saving raw and processed data sets.

(b) Data Processing:

The program reads acquired raw data from a temporary file and initially subtracts from each individual data value the average of all data values in that data set. It is necessary to eliminate low amplitude noise by setting two thresholds, one positive and one negative. In the present software, the thresholds are user defined for testing purposes, but in principle, determination of the threshold levels can be done in software. If the data point is greater/less than the relevant user-defined threshold, then the software considers that point as a starting position of a positive/negative peak. A positive/negative peak can be determined by calculating the maximum/minimum of the data values above/below the user-defined threshold values. The consecutive positive and negative peaks can then be tabulated. Starting from the first detected peak, the program counts one positive and one negative peak as a fringe.

4.3.2 Explanation of the Method

As an example of how the software works, the raw data from an initial field trial captured from a passing truck is shown in Figure 4-7. This test-set of 5000 data points was acquired with a sampling rate of 22050 samples/second; hence the data trace length is ~ 0.23 seconds. The program has detected 7 positive and 7 negative peaks (total 14 peaks) or in other words, 7 fringes detected for this particular event. Each data point in an array is numbered from 0 to n and called a *data index* of that particular data point. The first negative peak was detected at data index = 492 with amplitude approximately -13.3 units. As discussed in Section 4.3.1, the amplitude of the detected fringes has been averaged, and the first positive peak was detected at data index of 2318 with amplitude of ~ 16.6 units. These positions of positive (2318) and negative (2760) peaks can be termed as peak or trough indices respectively. As the program starts fringe counting from the first detected peak, the position of each positive peak is regarded as

the ‘fringe index’ for that particular fringe. The program determines and saves fringe amplitudes and fringe indices in a separate two-column file in text format.

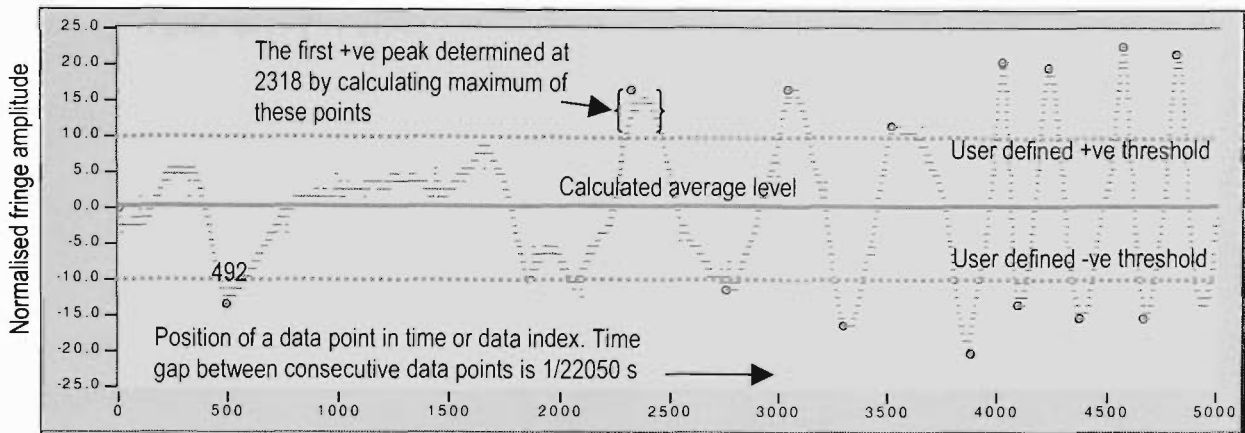


Figure 4-7: Output of typical fringe data showing complete data set, calculated average level for this particular data set, user-defined positive and negative threshold levels and detected positive and negative peaks.

The duration of the data traces in the practical field situation (more detail in Chapter 5) varied from a minimum of 2 seconds (44100 samples) to several seconds, giving rise to very long single column data files. A large portion of the file contains noise-data before and after the event (not shown in Figure 4-7). This pre- and post- noise is removed manually, but as mentioned earlier, would be removed by software in a practical implementation. The data processing strategy rejects detailed fringe shape information that does not add significant information about the structural deformation. Thus in this particular case, Figure 4-7, the program processes 5000 points and saves indices and amplitude data in the format shown in Table 4-1. The total number of data pairs (in this case 14) are the number of detected peaks and provides information stemming from the change in length of an embedded sensing fibre. The first column of Table 4-1 can be processed to reveal the “frequency” information for the detected fringes. Fringe frequency, the inverse of the fringe period, is indicative of the rate at which the sensing fibre is being stretched and gives direct information about the rate of applied structural deformation. The second column of Table 4-1 shows relative amplitudes of the detected fringes. These fringe amplitudes are important for deciding threshold levels before the

fringe detection step in the software, and the fringe indices are important for calculating instantaneous fringe frequency as discussed in the next section.

Table 4-1: Program processes raw fringe data and stores peak indices and corresponding amplitudes in this format.

Index	Amplitude
492	-13.3
2318	16.7
2760	-11.3
3042	16.7
3293	-16.3
3522	11.7
3875	-20.3
4021	20.7
4095	-13.3
4228	19.7
4371	-15.3
4569	22.7
4670	-15.3
4813	21.7

4.3.3 Instantaneous Fringe Frequency Calculations

As discussed in Section 3.7.5, the variations in fringe frequency with time provide information about the rate at which the structure is deforming (strain rate). The instantaneous fringe frequency (Figure 4-8) gives a single-valued frequency as a function of time for the data set shown in Figure 3-22. The instantaneous frequency of peak and trough for each fringe in Hz was calculated by dividing the sampling rate, 22050 samples/sec, by the total number of points defining that peak or trough. For example, consider a fringe consisting of total 100 data points where the peak has 60 data points and the trough has 40 data points. The algorithm generates two instantaneous frequency points for that fringe as 367.5 Hz (for peak) and 551.25 Hz (for trough). The fringe frequency suffers some quantization error due the limited number of points per fringe, and a post-filtering step is used to smooth this quantization

error. Figure 4-8 shows such post-filtering, a moving average filter, applied to the fringe frequency data obtained by processing the raw fringe data shown in Figure 3.22.

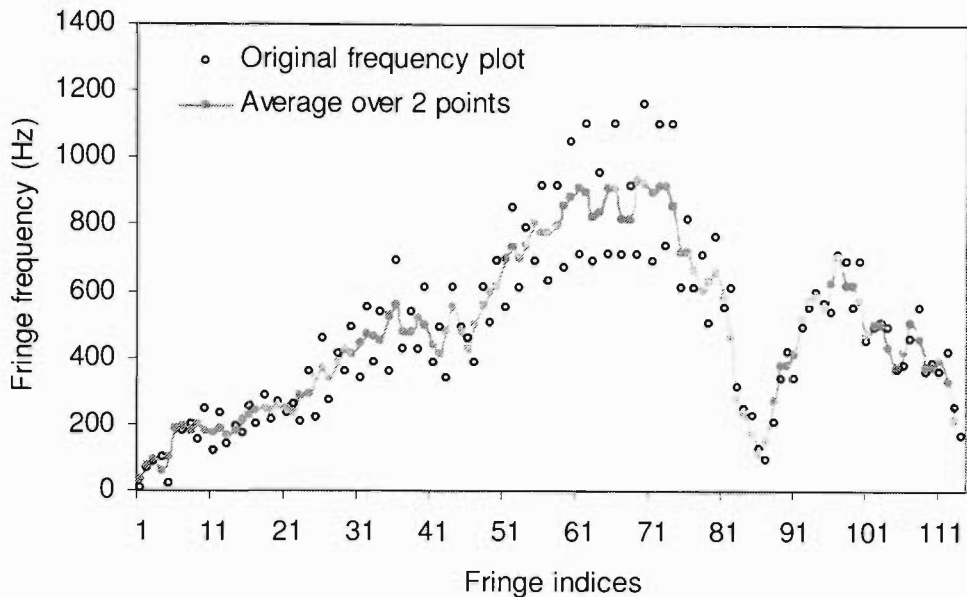


Figure 4-8: Instantaneous fringe frequency plot obtained by averaging the peak and trough frequency components in the raw fringe truck data shown in Figure 3.22.

4.3.4 Limitations

This algorithm has some problems in detecting incomplete (fractional) fringes and is susceptible to the relative amplitude variation of the fringes. The reasons for fractional fringes and the variation in fringe amplitude are discussed in Section 4.4.2.1. An example where the algorithm fails to detect a fringe due to significant variations in relative fringe amplitude is shown in Figure 4-9. The algorithm detects a positive peak detected at index 424 but fails to detect a negative fringe at index 462 which does not cross the user-defined threshold of -10 units. Thus the algorithm recognises this negative peak at index 462 as a part of amplitude variations and waits for the data trend to reach the negative maximum at index 544. This results it in missing another positive peak at index 511. Thus, the algorithm missed a negative and a positive peak or a complete fringe while analysing this particular data set. Therefore, this algorithm may fail to detect fringes where valid peaks (occasionally) fall below the preset threshold.

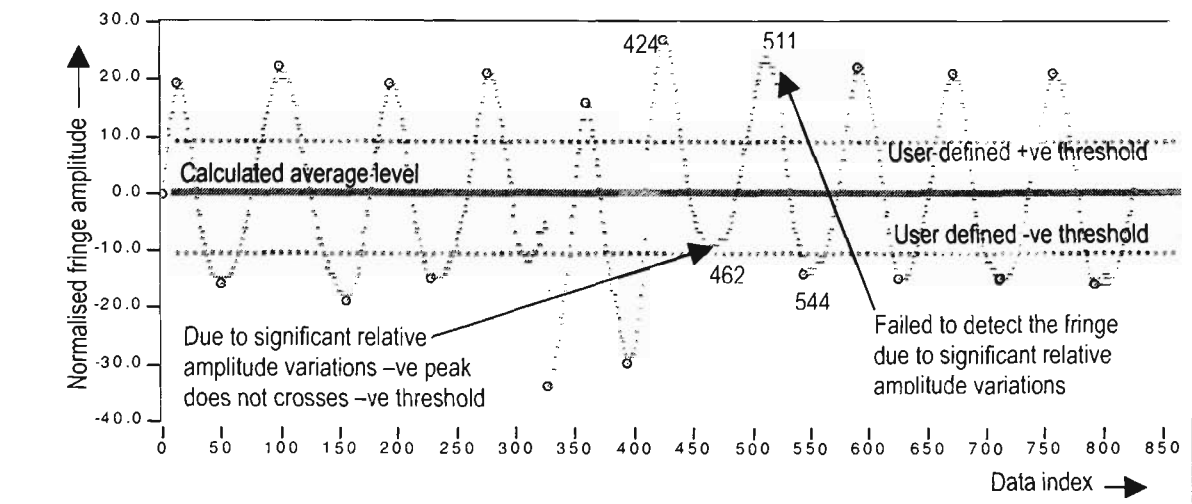


Figure 4-9: Example of the signal processing algorithm in operation, showing how it failed to detect this set of truck fringes with significant relative amplitude variations.

4.4 Sensor Characterisation

4.4.1 Test System Description

The test beam was configured as depicted in the photograph of Figure 4-10, in an Instron 8501 Universal Testing Machine, shown in Figure 4-11. The sensing system configured for laboratory trials is shown in Figure 4-12. The optical arrangement of the sensor was previously shown in Figure 4.3. During various laboratory trials, the sensor output was recorded and analysed while periodic deformations were applied to the mid-span region of the test beam.

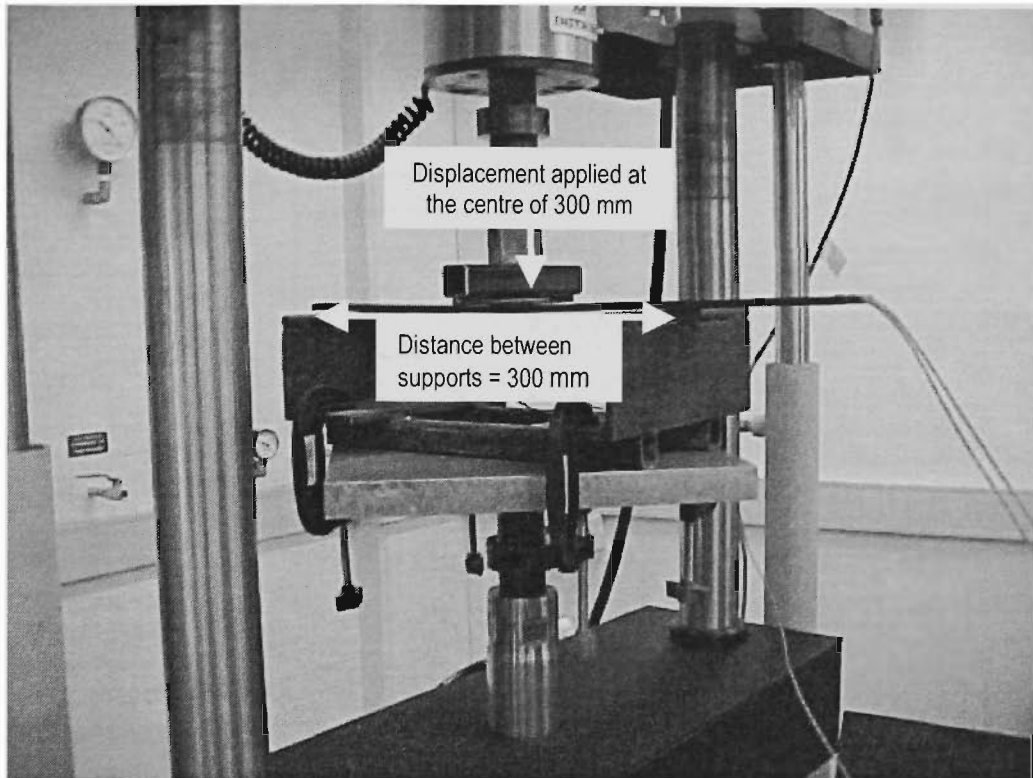


Figure 4-10: Laboratory setup showing the three-point bending system, within the Universal Testing Machine.

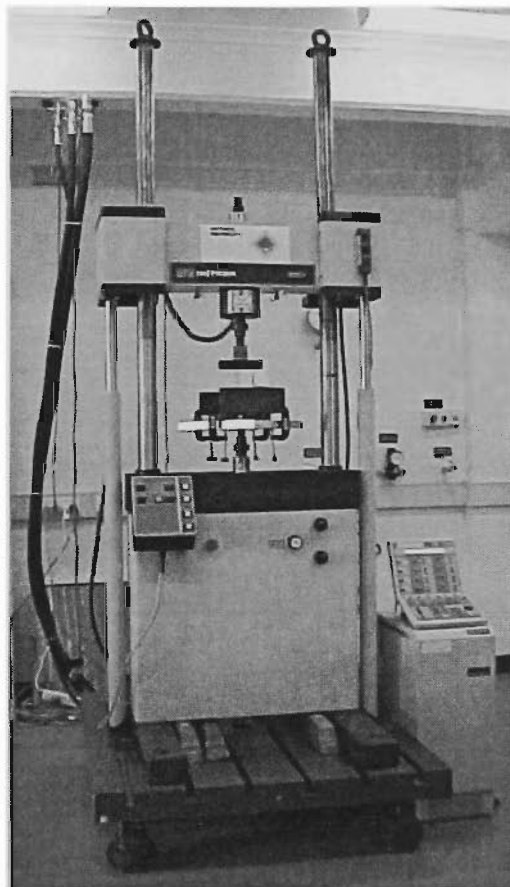


Figure 4-11: Instron 8501 Universal Testing Machine.

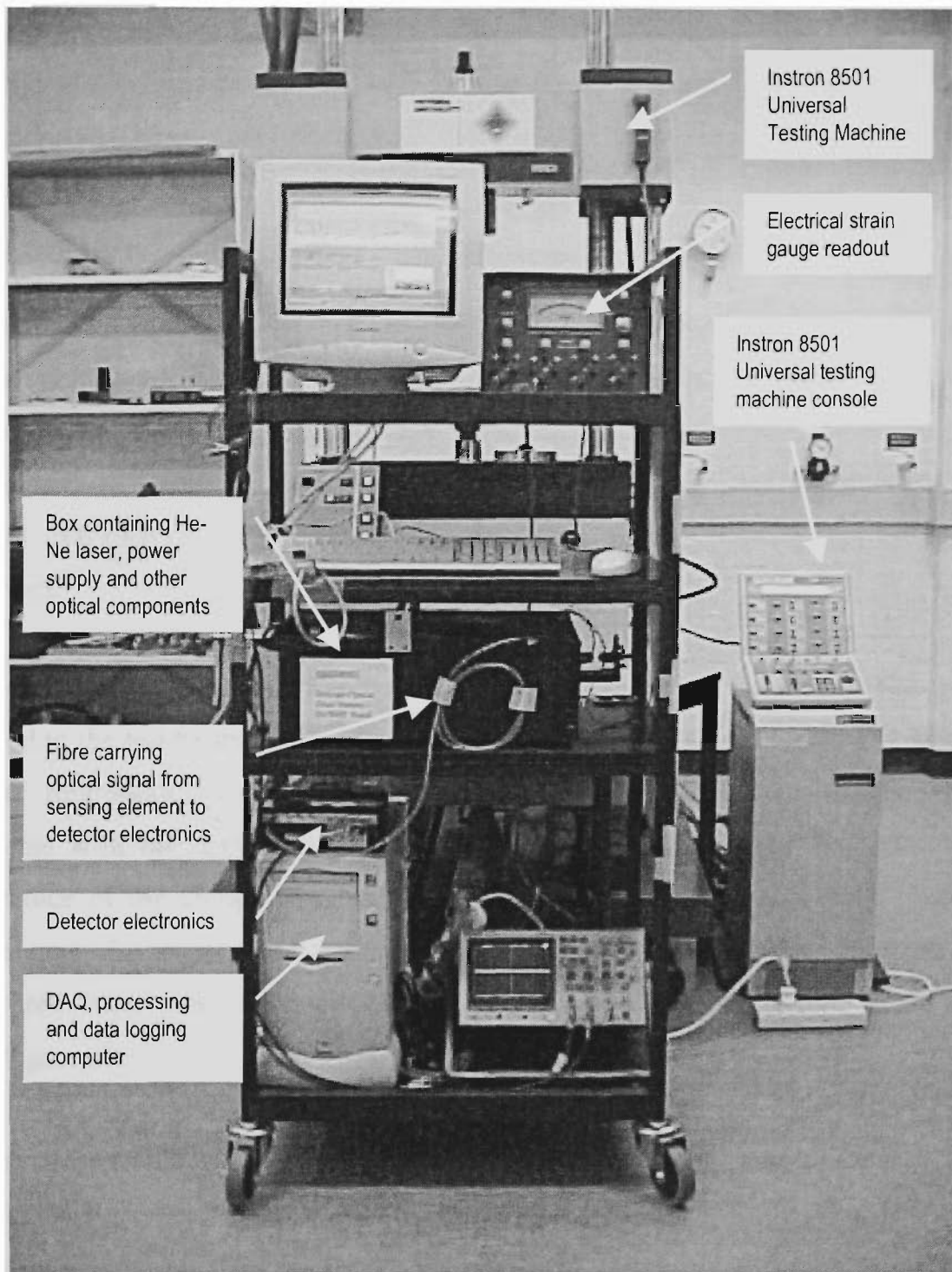


Figure 4-12: Laboratory sensor assembly.

4.4.2 Calibration

When the aluminium beam is subjected to various deformations, the surface installed electrical strain gauge determines the associated strain induced within the structure. In the first instance it is necessary to calibrate the electrical strain gauge before using it as

a standard to calibrate the FFPI sensor. The uncertainties in the electrical strain gauge readings and calibration are discussed in Section 4.4.2.1. The FFPI sensor calibration and characterisation is also discussed.

4.4.2.1 Electrical Strain Gauge Calibration

As mentioned in Section 4.2.1, an electrical strain gauge was bonded to the underside of the aluminium beam surface. This section investigates the performance of the electrical strain gauge by comparison with theoretical estimations calculated using Equation 3-12. This transducer beam was subjected to various triangular dynamic central deformations using the testing machine and the strain gauge output was recorded.

The electrical strain gauge output is linearly proportional to the central deformation applied to the test beam (Figure 4-13) with a correlation coefficient (R^2) of 0.999. (The Linear Regression method shows the degree to which the strain gauge readings correlate with the applied deformations, in this case $R^2 = 99.9\%$). Note that the magnitude of the compressive and tensile surface strains measured by the electrical strain gauge for an applied deformation is identical. In this case, the magnitudes of the measured strains were in agreement with theoretical estimations within a standard error of $1.9 \mu\epsilon$.

The uncertainties associated with the strain gauge and applied deformations using the testing machine were $\pm 3\%$ (for a single cycle) and ± 0.01 mm respectively. The errors in the electrical strain gauge were obtained by comparing the output with the theoretical estimation explained in Section 3.7.1. The major affecting factors involve combinations of unknown parameters such as (a) mechanical instabilities, (b) variation in the assumed position of the neutral axis (midway between the top and bottom surface of the beam) due to the presence of other grooves and (c) glue thickness beneath the electrical strain gauge.

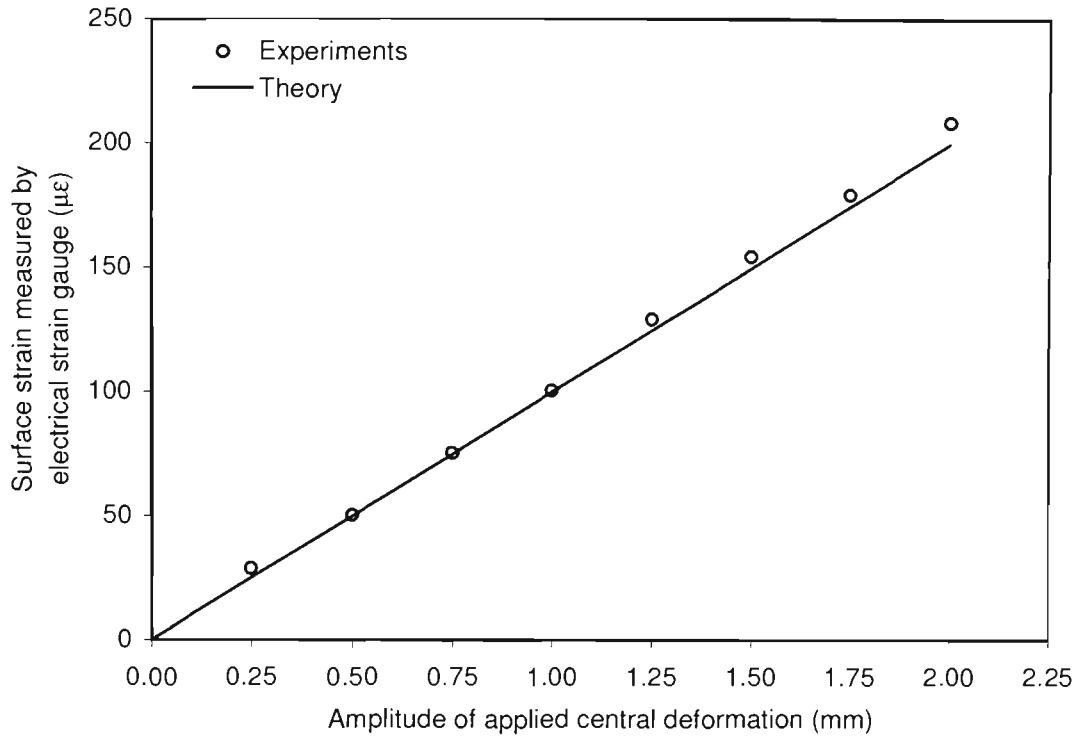


Figure 4-13: Measurements from surface installed electrical strain gauge readings compared with theory at various applied central deformations.

The applied deformation induces mechanical instabilities in the test structure due mainly to the vibration of the hydraulic pump used to actuate the machine. These instabilities, as measured by the surface installed strain gauge, are shown in Figure 4-14. The deformation cycle starts from the maximum deformed state of the test beam where the electrical strain gauge measures the maximum negative strain value, as it is bonded to the underside of the test beam. Therefore, the applied deformation and measured strain graphs are inverted compared to each other. Also, the positive and negative strain values shown in Figure 4-14 are due to the removal of the DC component, as explained in Section 4.3.1.

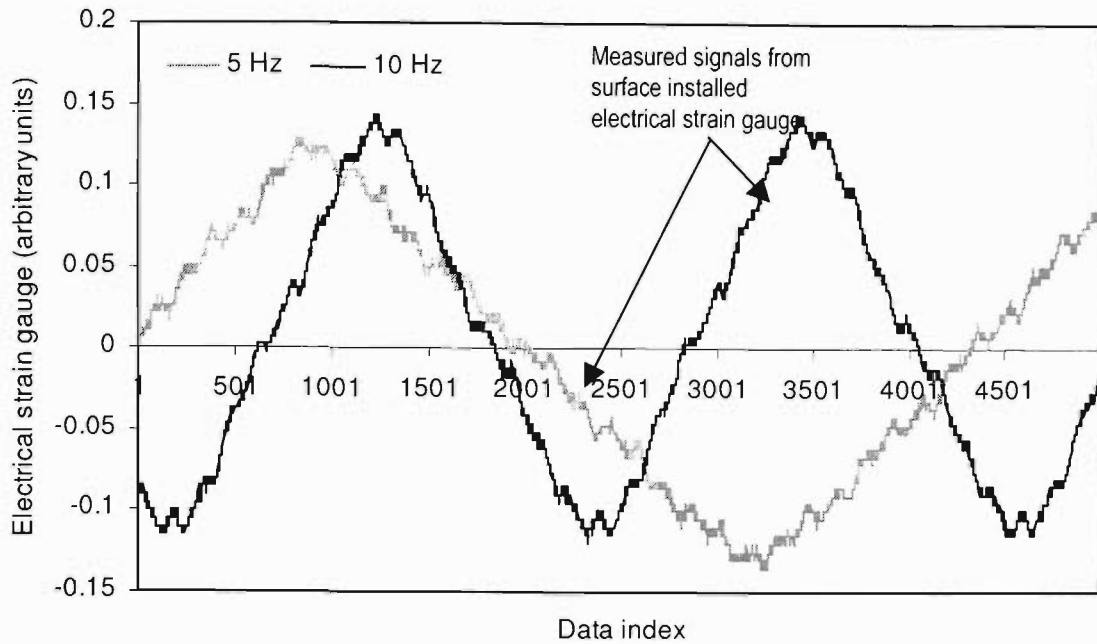


Figure 4-14: The test beam response measured by surface installed electrical strain gauge by applying a 2 mm peak to peak deformation signal at the rate of 5 Hz and 10 Hz using the testing machine. Mechanical instabilities in the test beam are apparent from the strain gauge profile.

4.4.2.2 FFPI Calibration

Theoretically, (from Section 3.2), one FFPI fringe is generated by $\sim 0.273 \mu\text{m}$ change in the sensing fibre length. Therefore, the fibre-length change (ΔL) associated with N fringes can be given as $\Delta L = (N \times 0.273) \mu\text{m}$. The strain induced on the sensing length of 300 mm is $\Delta L/L = [(N \times 0.273) \mu\text{m} / 0.3 \text{ m}] = (0.91 \times N) \mu\epsilon$.

Two FFPI sensing elements were embedded in the 6 mm thick aluminium beam, as described in Section 4.2.1. The test system was configured in such a way that one of the sensing fibres was placed very close to, but just off, the neutral plane to explore the response and noise in the low-sensitivity regime. Another sensing fibre was placed away from the neutral plane to provide a stronger signal for comparison. The test structure was pre-deformed at the centre of the three point bending arrangement shown in Figure 4-1 before applying the periodic deformation signal. The primary purpose of pre-deformation was to achieve good contact with the test beam and, secondly, to move into the linear range of operation. The expected strain profile as a function of various

central deformations for two installation depths is presented in Figure 4-15 as obtained using Equation 3-12.

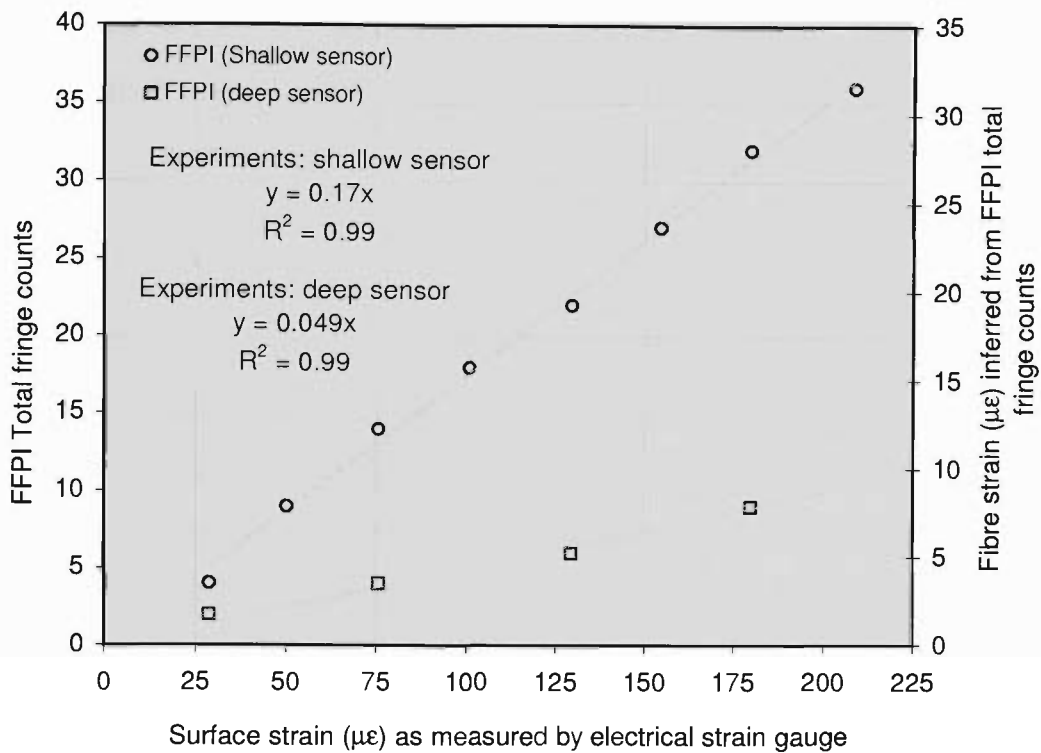


Figure 4-15: Average of fringe counts from the two different FFPI strain sensors in the aluminium beam as a function of peak strain, obtained from the surface installed electrical strain gauge, for periodic deformations of various amplitudes.

Periodic deformations of various amplitudes were applied, at a constant frequency of 20 Hz, and FFPI output fringes were recorded for both sensors. The total fringe counts were obtained using software described in Section 4.3. The average of the total number of output fringes (over several deformation cycles) is shown as a function of the peak surface strain, as measured by an electrical strain gauge, in Figure 4-15. The right hand Y-axis shows the inferred fibre peak strain values calculated from the total fringe counts $[(0.91 \times N) \mu\epsilon]$. Clearly the total fringe counts vary linearly with the measured surface strains and the straight line fit shows a correlation factor of 0.99 for both sensors.

A surface strain of $210 \mu\epsilon$, induced by applying a central deformation of 2.00 ± 0.01 mm, gives $\sim 105 \pm 3 \mu\epsilon$ mid-way between the neutral plane and the surface of the test structure. The shallow FFPI sensor, installed at a similar depth, outputs 36 fringes for this deformation as shown in Figure 4-15. Thus, experimentally, the round trip phase-strain sensitivity for the shallow sensor is $\Delta\phi / \epsilon L = 3.59 \times 10^6 \text{ m}^{-1}$ which is 3 times lower than the expected value of $1.15 \times 10^7 \text{ m}^{-1}$ from Equation (3.7). The deep sensor has a phase-strain sensitivity of $1.02 \times 10^6 \text{ m}^{-1}$, which is ~ 10 times lower than the expected value. It is important to note, especially in the case of the deep sensor (located ~ 0.1 mm from the neutral plane), that a very small discrepancy ($\sim \pm 0.5$ mm) in the distance of the sensor from the neutral plane affects the sensitivity very significantly (up to a factor of 6). Hence, the distance of the embedded sensing fibres from the neutral plane determines their sensitivity to lateral bending, with sensitivity becoming zero for fibres that happen to lie exactly in the neutral plane, as recognised by others¹⁵⁵. In addition, there are other small errors including instrumental errors associated with the electrical strain gauge ($\pm 3\%$) and errors in the amplitude of the applied central deformation (± 0.01 mm). Also, surface installed electrical strain gauge is a point sensor and monitors strain at a single point at the mid-span on the beam surface. However, embedded FFPI measures average strain along the sensing length at its depth. Therefore for a given distance from the neutral plane, the average strain should be less than the point strain, inferred from the surface installed electrical strain gauge measurements, at the mid-span of the test beam.

In the case of bonded fibre sensors, Lesco *et al.*¹⁵⁶ compared the performances of an extrinsic fibre Fabry-Pérot sensor and conventional resistive foil strain gauges. They demonstrated that the experimental results are in agreement with the theoretical strain-matrix concentration created in vicinity of the fibre. The extent of adhesion between the optical fibre sensing element and the test beam affects the reliability and performance of the sensor system. The fibre has an acrylite coating which is far less rigid than the glass fibre and the surrounding material. Thus, the strain measured by a length of fibre is less than the real strain on the surrounding material¹⁵⁷. Therefore, in this case the

strain measured by the electrical strain gauge gives the true strain on the test structure. In addition, the fibres are embedded in the grooves with a particular bonding material in such a way that they are parallel to the neutral plane. The strain transfer coefficients of the bonding material also affects the strain response of the fibre optic sensor. Moreover due to a non-uniform amount of bonding material along the length of a sensing fibre and beam, it is likely that the sensing element is not exactly parallel to the neutral plane. Also, as mentioned in Section 4.4.2.1, variation in the assumed position of the neutral plane (midway between the top and bottom surface of the beam) due to the presence of other grooves also affects the system. Therefore, it is necessary to determine the calibration factor for each of the embedded FFPI sensors by measuring its response relative to that of an electrical strain gauge.

4.4.3 Sensor Repeatability and Linearity

Sensor repeatability was investigated by counting the total number of fringes for several sinusoidal deformation cycles applied at constant amplitude of 1 mm and deformation frequency of 10 Hz. Figure 4-16 shows an example of the applied sinusoidal deformation cycle recorded from the actuator output of the testing machine and the corresponding fringe groups showing consistent fringe counts for the deformation and relaxation cycles. As the rate of applied deformation increases, the output fringe frequency increases gradually reaching maximum at around 0.5 mm deformation. At the transition point from the applied deformation to relaxation, an abrupt reduction in the fringe frequency is also apparent in Figure 4-16.

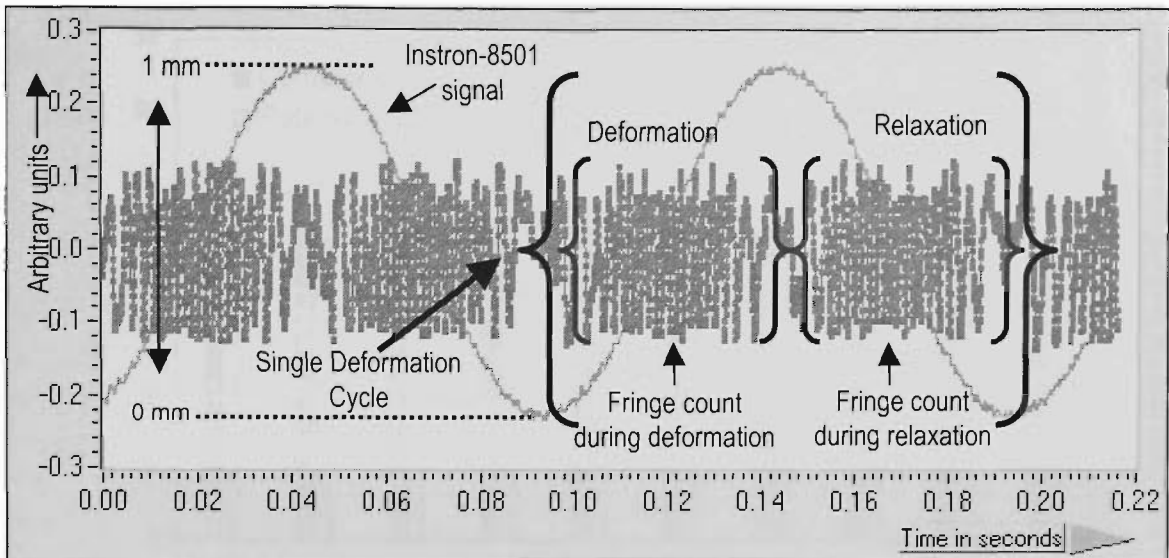


Figure 4-16: Shallow FFPI output fringes obtained from a 1 mm deformation at the centre of the aluminium beam using the testing machine at a deformation rate of 10 Hz.

Figure 4-17 shows deformation-relaxation fringe counts for 10 consecutive cycles for a constant applied deformation amplitude of 1.25 mm at a frequency of 20 Hz, as a function of cycle number (total 10 cycles). For each cycle a pair of bar graphs is shown; the left and right of each pair represents compression and relaxation fringe counts observed at a deformation frequency of 20 Hz respectively. It can be noted that the total fringe counts remain consistent within ± 2 fringes for several applied structural deformation cycles and independent of the applied deformation frequency. The independence of the fringe counts to frequency was expected, but it was thought prudent to check that the hardware filter or the acquisition algorithm was not influencing the fringe count in the frequency area of interest.

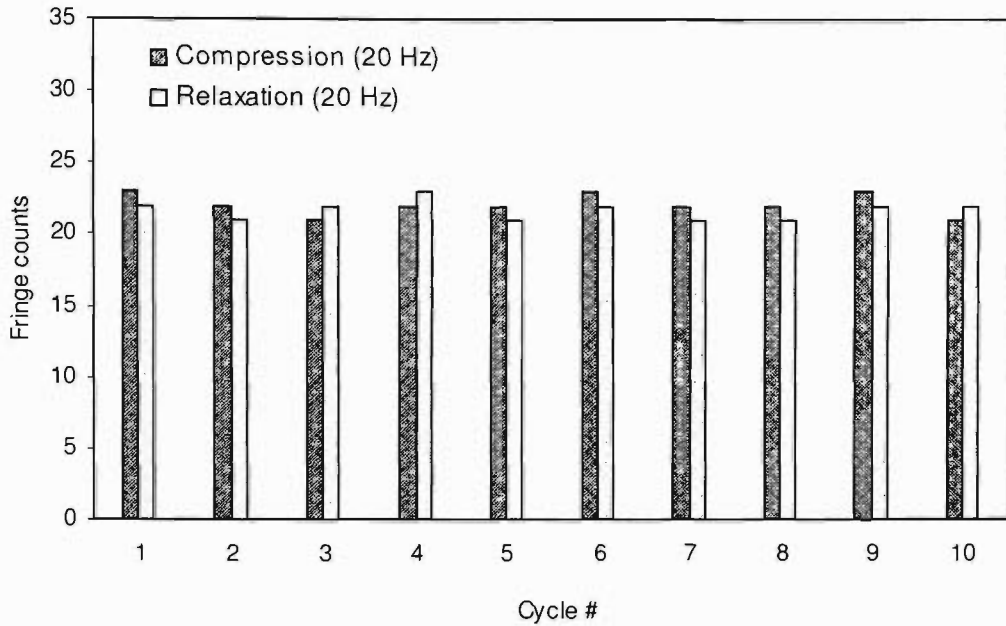


Figure 4-17: Measurement of sensor (shallow FFPI) repeatability for 10 cycles at applied deformation frequency of 20 Hz with a central deformation of 1.25 mm.

Sensor linearity was also tested by counting the total number of fringes obtained for various central deformation amplitudes between 0.25 and 2 mm. The total number of fringes was found to be consistent within 1 to 2 fringes (Figure 4-18) subject to limitations of the acquisition algorithm; see Section 4.3.4. This shows that the FFPI sensor gives consistent measurements for structural deformation and relaxation without any significant hysteresis.

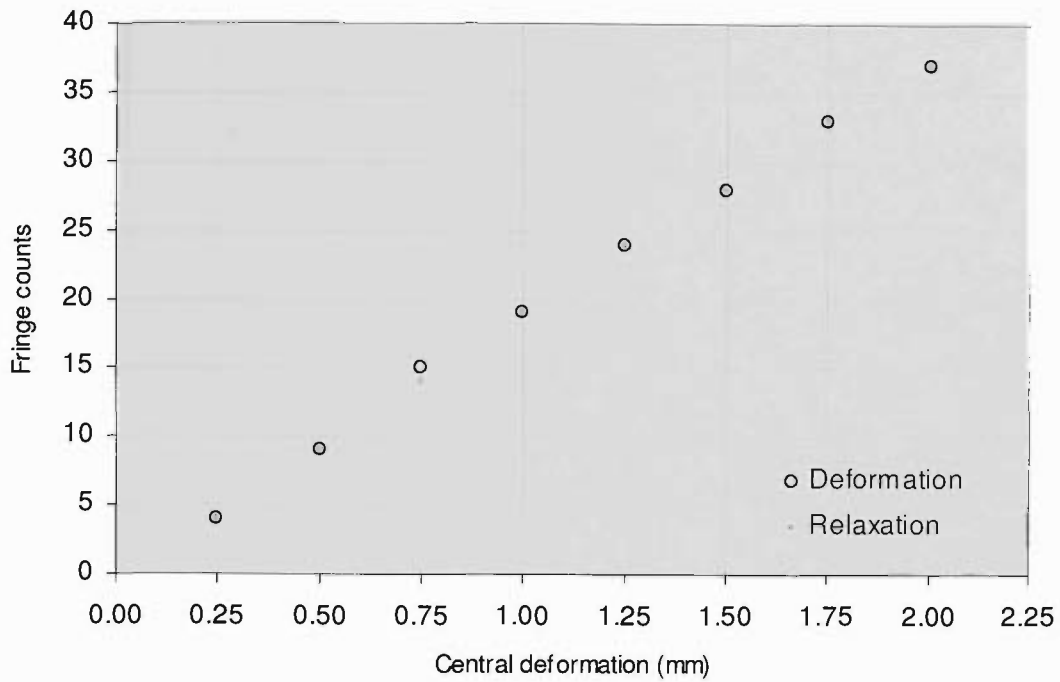


Figure 4-18: Fringe counts during deformation and relaxation of the shallow FFPI sensor for a single deformation and relaxation cycle, for various central deformations.

Figure 4-19 shows a graph of a calibration factor, the ratio of the number of fringes to the magnitude of the central deformation (fringes/mm), as a function of the central deformation as measured by the shallow FFPI sensor, and obtained from the data in Figure 4-18. The average of ~ 17.8 fringes/mm remains constant for the applied deformation frequency of 20 Hz.

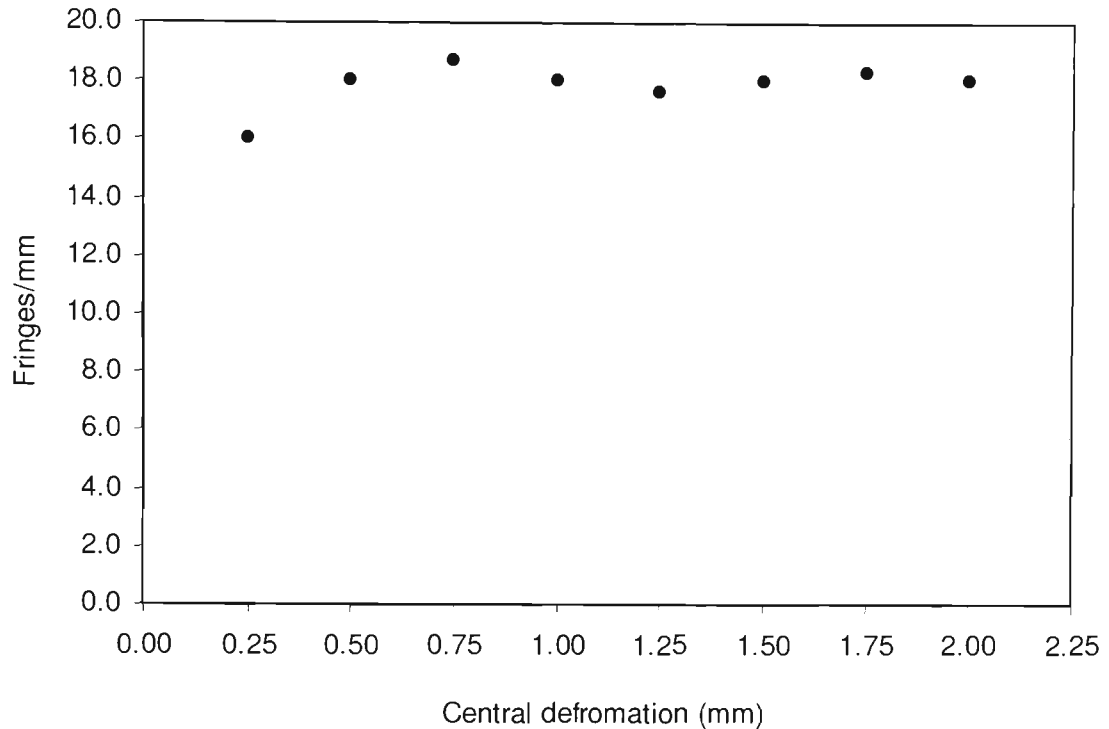


Figure 4-19: Calibration factor (fringes/mm) as a function of the central deformation amplitude for the shallow FFPI sensor.

4.4.4 Effect of Sinusoidal and Triangular Deformation Profiles on the Output Fringe Patterns

These tests assess the ability of the sensor to determine the deformation profile from the fringe frequency information.

As structures can deform randomly under the action of random perturbations of any amplitude, it was important to investigate the sensor response for various deformation functions. During these experiments, the aluminium test beam was subjected to sinusoidal (Figure 4-20) and triangular (Figure 4-21) deformation functions at various frequencies and the output fringe patterns were recorded and analysed. The mechanical instabilities (explained in Section 4.4.2.1) induced by the testing machine on the test structure have already been observed in the measurements recorded from the surface installed electrical strain gauge (Figure 4-14). Furthermore, sudden minor changes in the direction of structural deformation due to these mechanical instabilities also induce

variations in the output FFPI fringe amplitudes (Figure 4-20) and lead to incomplete or rapidly reversing fringe patterns.

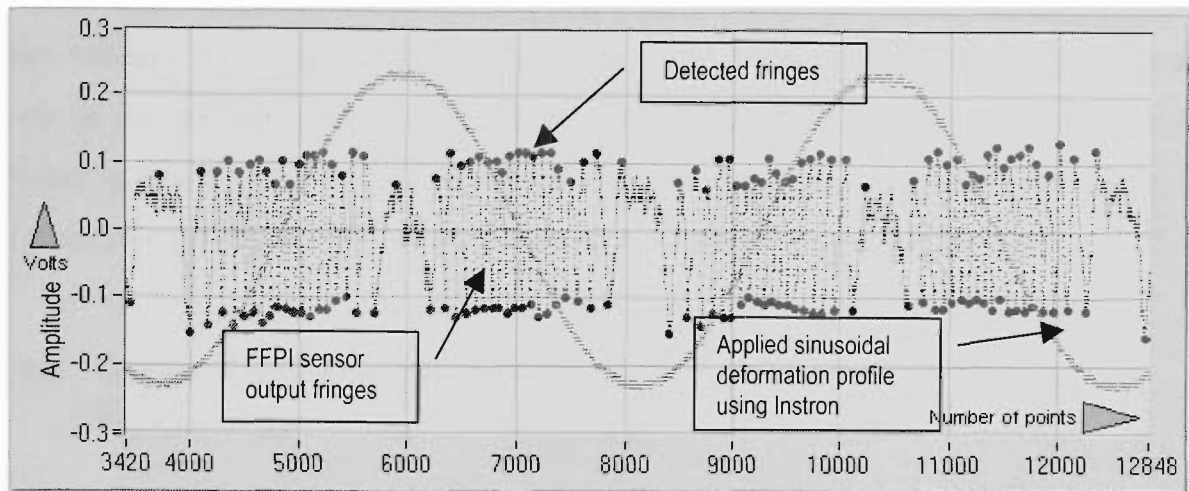


Figure 4-20: Processed and detected fringe data for shallow FFPI sensor obtained by applying a sinusoidal deformation to the test beam.

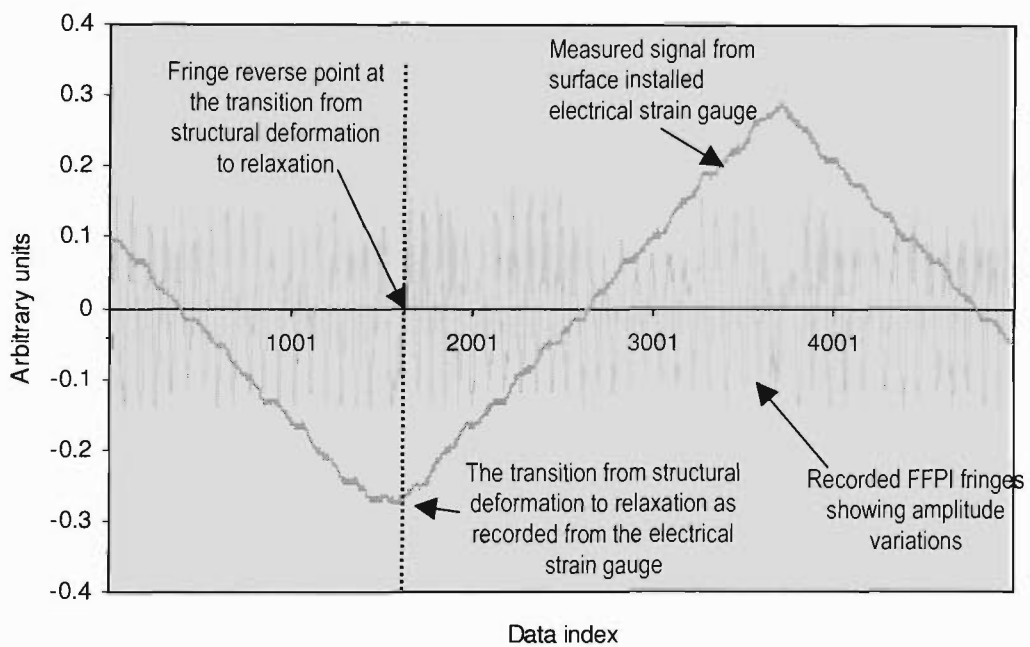


Figure 4-21: FFPI shallow sensor and strain gauge response for applied triangular deformation.

The electronic bandwidth of the detector circuitry also contributes to fringe amplitude variations and is evident at the turning points of the applied mechanical deformation

waveform. As the mechanical waveform approaches the peak value, the rate of deformation reduces gradually from a constant value to zero (Figure 4-20). This reduction of deformation frequency reduces the fringe rate to zero and the electronic filter reduces the fringe height. This effect separates the deformation and relaxation cycle of the test structure visibly in Figure 4-20. However, a similar effect is not very evident in Figure 4-21 as the mechanical deformation cycle has a triangular shape, and so there is a rapid transition from deformation to relaxation and vice versa.

4.4.5 Estimation of Applied Deformation Profile using Fringe Frequency

This section uses the change in output fringe frequency to estimate the shape of applied deformation profiles.

When the beam was subjected to sinusoidal deformations (Figure 4-20) the fringe frequency increases to a maximum for the highest slope of the applied deformation function. On the other hand, the fringe frequency reduces to a minimum for the minimum slope of the applied deformation cycle. Therefore, the phase difference between the processed FFPI signal and the electrical signal is 90° . Figure 4-22 shows the applied sinusoidal deformation profile and the strain profile obtained by processing the instantaneous fringe frequency data recorded from the FFPI sensor, confirming this expectation.

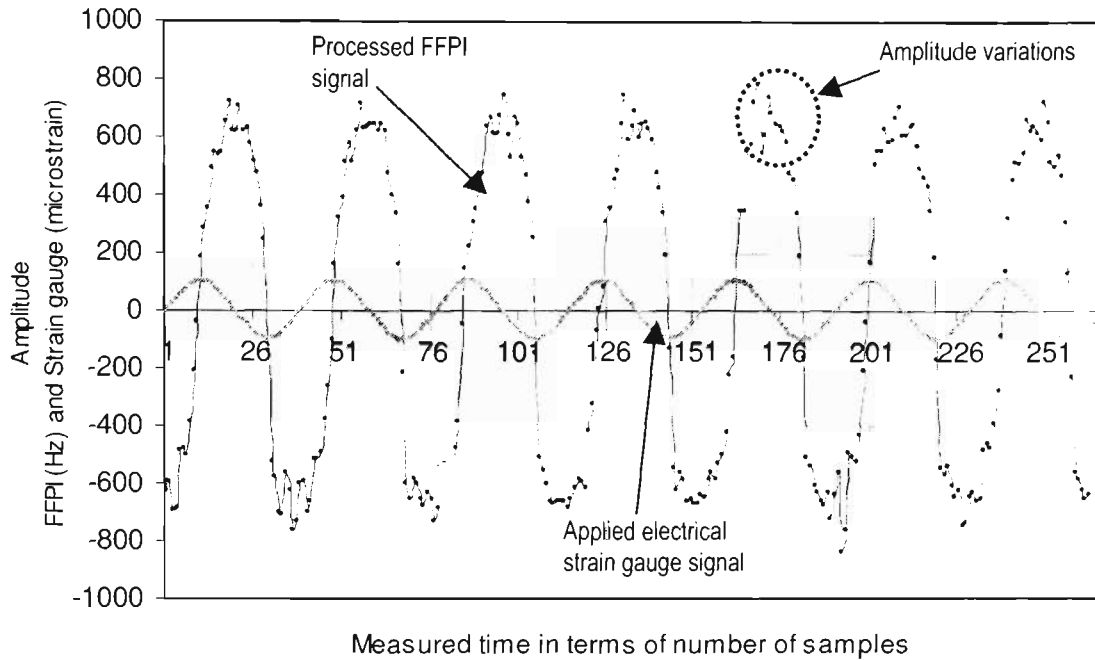


Figure 4-22: Comparison between structural strain profile obtained by processing the fringe frequency and electrical strain gauge. This data was recorded for 1 mm central deformation.

The FFPI signal shows high-frequency variations in the individual peaks and troughs. These high-frequency noise components are about 1/6 as large and at frequencies similar to the optical fringe rate. This is easily noticeable at the peaks of the processed FFPI signal (Figure 4-22) and was expected (Section 4.3.3). It is caused by variations in the instantaneous fringe frequency, which in turn is caused by the undesirable structural instabilities induced by the testing machine.

The FFPI response was also investigated by subjecting the test beam to triangular deformation functions. Figure 4-23 shows the triangular deformation profile of the actuator applied to the test beam and the resultant FFPI sensor response. When the test beam was subjected to triangular central deformations, the slope of the deformation profile was constant and therefore, the fringe frequency (in this case ~ 1000 Hz) was constant during both, deformation and relaxation of the test beam (Figure 4-23). Hence, the sensor response shows a square wave profile when the structure is subjected to triangular deformations. Figure 4-24 shows an applied triangular deformation and the processed FFPI response. The plot shows amplitude variations in the processed FFPI

signal just after each sudden transition. This is a real effect in the turning points of the applied triangular deformation waveform caused by the mechanical system failing to produce an ideal triangular deformation.

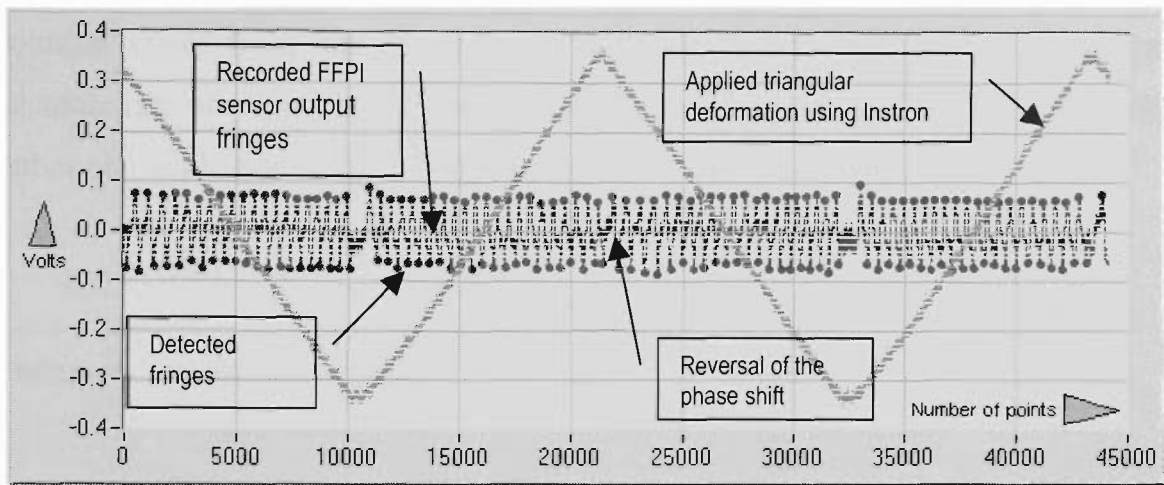


Figure 4-23: Output of the data processing algorithm showing detected fringes from shallow FFPI sensor by applying a triangular deformation to the test structure using the testing machine.

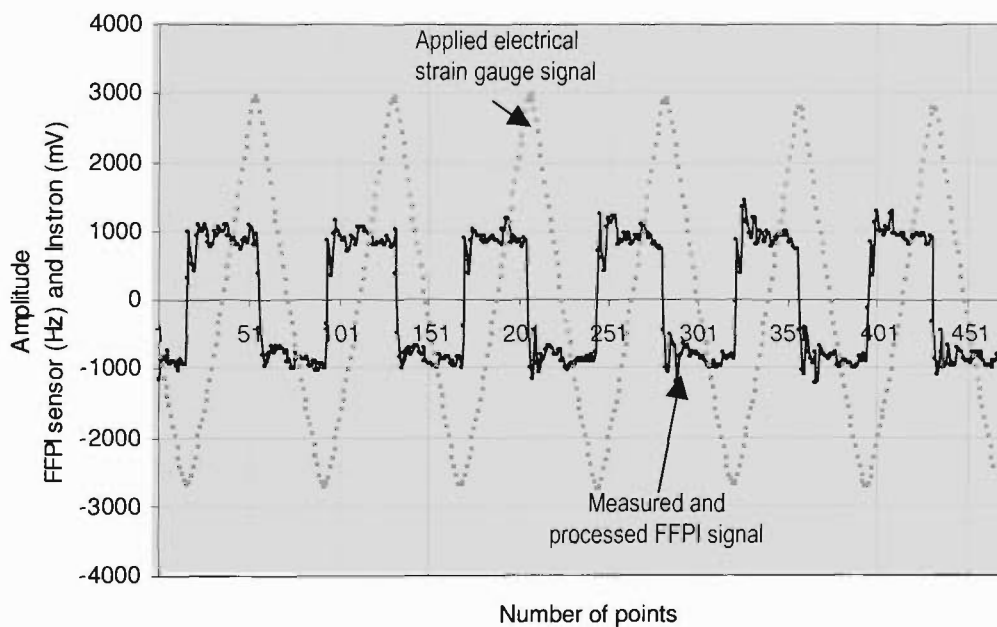


Figure 4-24: Comparison between structural deformation profile obtained by processing the FFPI fringe data in Figure 4-23 and an applied triangular deformation function.

The method of calculating the instantaneous fringe frequency is explained in Section 4.3.3. As discussed in Section 4.4.2.2, each fringe represents approximately 0.268 μm change in the length of the sensing fibre and the number of points defining each fringe (fringe resolution) changes with changes in the fringe period. Hence the strain resolution varies from one fringe to the next in a single data trace. The maximum detectable rate of change in the sensing length can be determined for a given minimum number of sample points for a fringe, as follows:

$$= \frac{22050 \left(\frac{\text{samples}}{s} \right) \times 0.268 \left(\frac{\mu\text{m}}{\text{fringe}} \right)}{\text{number of points in that fringe} \left(\frac{\text{samples}}{\text{fringe}} \right)}$$

$$= \frac{5909.4}{\text{number of points in that fringe}} \left(\frac{\mu\text{m}}{s} \right)$$

Figure 4-25 shows typical fringe data recorded by bending the test beam at a frequency of 20 Hz. The mechanical vibrations induced by the testing machine affect the fringe shape. However, approximately 14 – 16 data points per fringe were observed in this case. The minimum observed fringe was 14 points/fringe which gives ~ 422.1 $\mu\text{m/s}$ and therefore, the maximum detectable change in strain of the 0.3 m sensing length is $[422.1 (\mu\text{m/s}) / 0.3 (\text{m})] = 1407 (\mu\epsilon/\text{s})$. This indicates that for this particular data set, the FFPI sensor is detecting dynamic strains (rate of change of the sensing length) of the order of 1407 Hz or 1 kHz. Better strain resolutions at higher deformation rates can be achieved by using higher sampling rates and expensive data acquisition hardware.

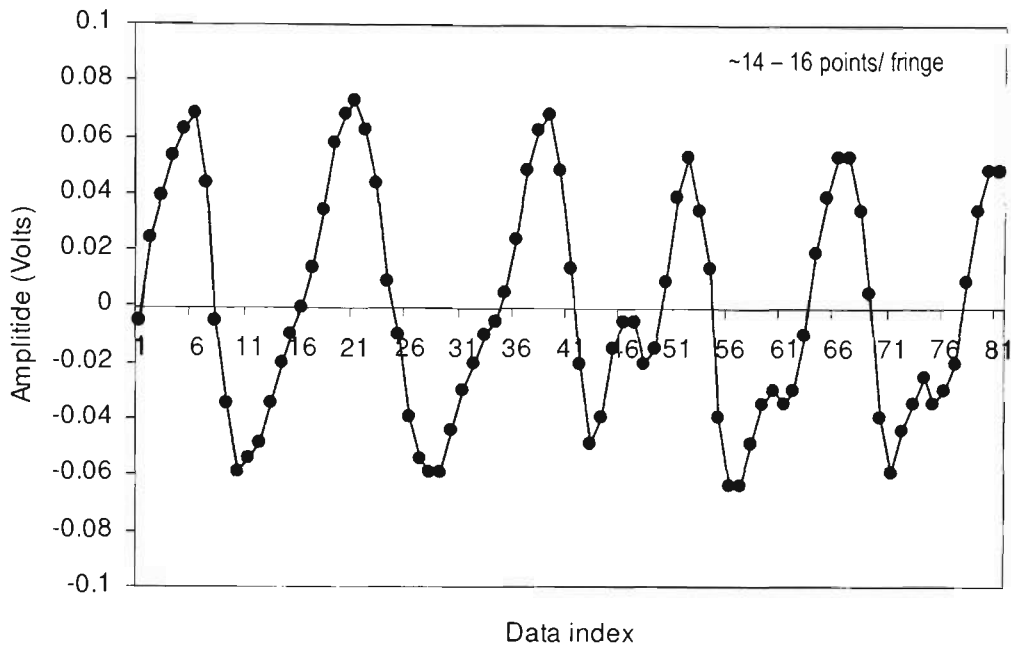


Figure 4-25: Typical FFPI fringes recorded at a 20 Hz deformation frequency showing individual number of points per fringe.

Thus, the FFPI response was studied by applying various deformation functions to the test beam. From the discussion in the previous paragraphs it is clear that this sensor has the ability to determine the shape of an applied deformation profile. This property of the sensor is useful for determining the shape of a pavement deformation profile (Section 5.7.2).

4.4.6 Strain Sensing Limitations of the Laboratory Experiments

This sensor monitors dynamic structural strain profiles at various deformation frequencies. In these measurements the sensor output was obtained by deforming the test beam at various frequencies using the testing machine. As discussed above, the dynamic response of the FFPI sensor is linear with applied sinusoidal deformation and the fringe count is independent of frequency in the range of 5-20 Hz. In this test the FFPI output was recorded by applying deformation frequencies above 20 Hz. This allows investigation of the FFPI sensor response at higher deformation frequencies.

Figure 4-26 shows the plot of normalised number of total FFPI fringes and amplitude of the periodic deformation signal as a function of various deformation frequencies applied using the testing machine. At low deformation frequencies, ~ 30 Hz, the FFPI fringe frequency decreases below the lower limit of the electronic filtering circuit that reduces the fringe amplitude significantly. On the other hand, for deformation frequencies above ~ 25 Hz, the applied deformation signal is distorted significantly. Finally, the testing machine gradually reaches its mechanical limit at ~ 50 Hz; Figure 4-27 shows a deformation profile as the testing machine reaches its mechanical limit and the corresponding FFPI fringe patterns. As the rate of deformation increases, the mechanical limit of the applied deformation profile gradually affects the quality of the FFPI fringe patterns. In these cases, the software fails to detect the affected fringes and the FFPI sensor response follows a similar trend to that of the testing machine data shown in Figure 4-26. Moreover, at higher deformation frequencies, apart from the higher frequency limits of the electronic filter, ~ 50 kHz, the FFPI sensing performance is limited by the capability of the data acquisition system. In this particular case the maximum sampling rate of the hardware is 1 MHz.

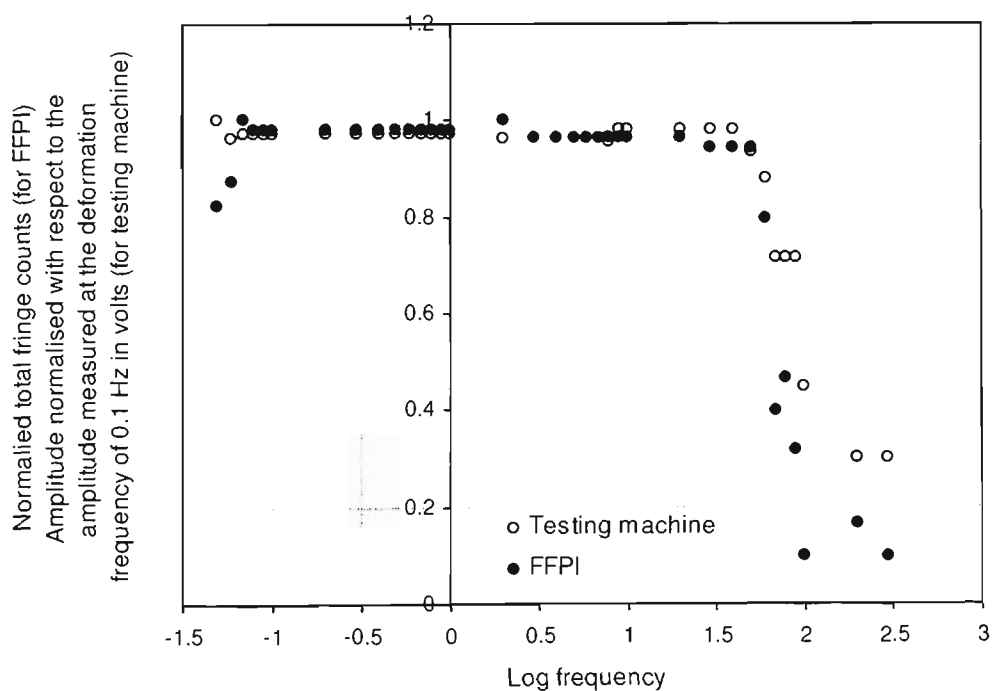


Figure 4-26: The frequency response of the testing machine and the FFPI sensor showing how the testing machine reaches its mechanical limit at a deformation frequency of ~ 50 Hz.

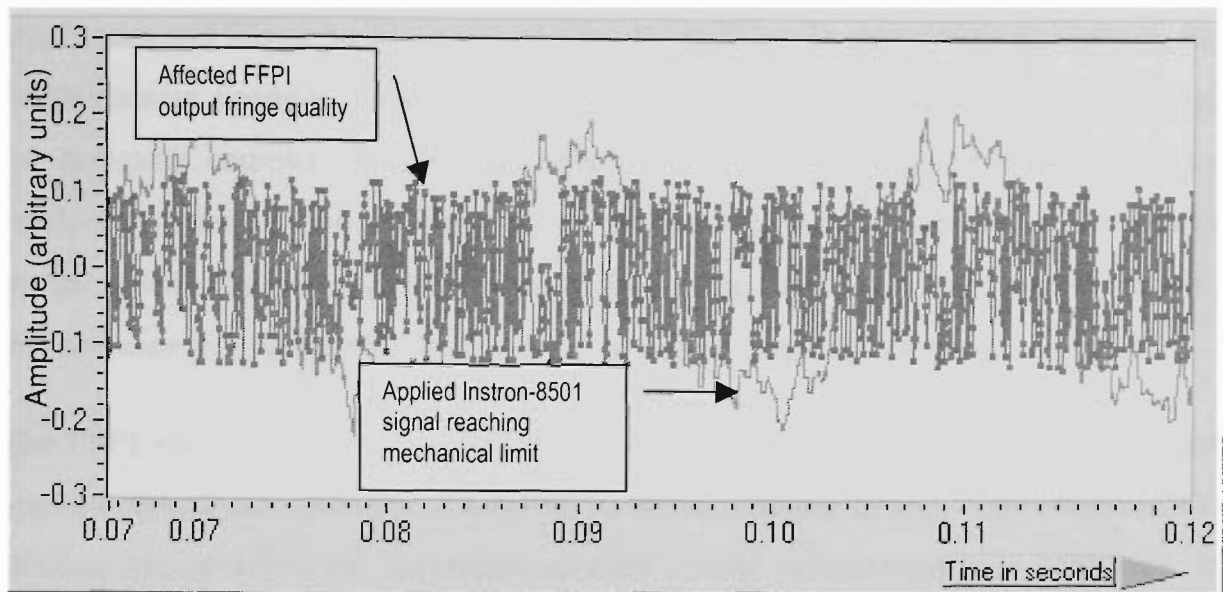


Figure 4-27: Output FFPI fringes recorded from the shallow sensor showing how they are affected by the mechanical limit of the testing machine at a deformation rate of 50 Hz.

4.5 Summary

The FFPI sensor was developed and investigated for its response by conducting various tests in a controlled manner.

Laboratory transducers consist of 300 mm FFPIs with the launching end reflector being an in-fibre Bragg grating and gold coating as the far-end. Two FFPI sensing elements were embedded in an aluminium test beam (length 500 × width 59 × thickness 6 mm) and their responses were compared with the output of an electrical strain gauge (error $\pm 3\%$) installed on the surface of the test beam using a three-point bending configuration. The test beam was deformed (error ± 0.01 mm) at its centre using the testing machine. The electrical strain gauge response was found to be linear as a function of applied central deformations of various amplitudes. The surface strain of $210 \mu\epsilon$ was measured by the electrical strain gauge for the maximum applied central deformation of 2.00 mm. These tests also revealed that hydraulic actuators of the testing machine generate undesirable mechanical instabilities in the test beam.

National Instrument's LabView4.1 was used for developing the software for acquiring, processing and storing FFPI output data. The processed data in the form of fringe

amplitudes and fringe positions versus time for each *event* were stored in separate files. As this sensor operates in the fringe counting regime, the software was developed only for detecting complete fringes and rejects occasionally generated fractional fringes produced by the relative amplitude noise in the fringe data, which in turn was induced by the mechanical instabilities generated by testing machine. Hence the resolution of this software in counting the total number of output fringes is ± 1 fringe.

The FFPI was calibrated by counting the total number of fringes obtained for various applied central deformations. A total of 36 interferometric fringes were observed for a shallow sensor when the maximum applied central deformation was 2.00 mm. The surface mounted electrical strain gauge measured $\sim 210 \mu\epsilon$ for this deformation. The inferred strain for the shallow sensor installed mid-way between the neutral plane and the beam surface was calculated using Equation 3-12 as $105 \mu\epsilon$. Therefore the shallow FFPI sensor has a calibration factor of $\sim 3 \mu\epsilon/\text{fringe}$ and produces an uncertainty of $\sim \pm 1.5 \mu\epsilon$ considering that the FFPI has an error of ± 1 fringe.

The sensor repeatability was studied by counting the total number of output fringes for several deformation-relaxation cycles at a constant applied deformation amplitude and frequency. The fringe count error was found within ± 2 fringes which is imposed by the software code and the inability of the software to detect occasionally generated fractional fringes in the data set. The total number of fringes counted for a single deformation-relaxation cycle was observed without any significant hysteresis for various deformation amplitudes and frequencies. At higher deformation frequencies above ~ 50 Hz, the amplitude of the testing machine signal gradually decreases affecting the output FFPI fringe quality and hence the fringe counting algorithm.

The instantaneous fringe frequency of the output FFPI fringe data was used for estimating the applied signal profiles (in this case sinusoidal and triangular) used for deforming the test beam. The phase of processed FFPI output for deformation-relaxation cycles was observed to be 90° out of phase to the phase of an applied deformation signal with $\sim 16\%$ peak to peak amplitude variations generated by the irregularities in the instantaneous fringe frequencies.

CHAPTER 5

RESULTS AND DISCUSSION

5.1 Introduction

As hypothesised in Section 3.7.3, a heavy vehicle travelling along a highway depresses the highway pavement vertically, compressing the sub-layers, which react by expanding horizontally. A fibre optic Fabry Péroto interferometer embedded at a given depth below the surface and oriented across the traffic lane, responds by producing optical fringes whose frequency varies linearly with the instantaneous rate of lateral expansion or contraction of the sub layers.

As discussed in Section 3.7.2, the compression and relaxation at depth is essentially an elastic process; vehicle-induced deformations are expected to be roughly linear with applied load. So the compression and relaxation processes ought to be symmetric for each individual axle. An axle in isolation passing over the sensor should produce two groups of fringes - those occurring during the compression phase and the same number in principle occurring during the relaxation phase. The total fringe count should scale linearly with the axle load. Therefore, it might be expected that the total accumulated fringe count for a given vehicle should also scale roughly linearly with its gross weight. A simple operating algorithm, based on this assumption of linearity, would be to divide the total fringe count for each vehicle by a calibration factor (in fringes per tonne) to deduce the total vehicular weight. One would determine this calibration factor for each sensor experimentally by acquiring fringe counts for a series of vehicles of known weights and performing a simple linear regression on the data. As discussed in Section 5.5.6, a simple calibration factor cannot be strictly applied because of the variety of axle configurations and spacings in normal traffic. As discussed in Section 3.7.2, a more sophisticated model based on overlapping Lorentzian distributions is a better approach.

The assumption of linearity was tested for many heavy vehicles by correlating total fringe counts with their gross weights determined simultaneously by CULWAY system (Section 5.2) designed by the Australian Road Research Board (ARRB). Also for a test set of trucks, weights were measured independently axle-by-axle on a traditional static weighbridge unit known as an Electronic Mass Unit (EMU) located nearby.

The reliability of the CULWAY sensor was confirmed by separate comparison with the EMU device, showing agreement within about 1%, as described in Section 5.2.2. For the remaining tests, therefore, the CULWAY was treated as the standard against which the single-transducer fibre Fabry-Pérot interferometric (FFPI) sensor was calibrated for WIM applications. The installation details for the FFPI sensor are discussed in Section 5.3.

Section 5.4 explains the generic error factors affecting the FFPI output. The analysis described in Section 5.5 discusses FFPI output fringe patterns and assesses the viability of the single-transducer FFPI sensor system for WIM applications. The calibration factors were obtained for heavy vehicles with various axle configurations by correlating the total FFPI fringe counts with CULWAY records. A Lorentzian model was developed to allow for the fringe count dependency on the axle separation.

As discussed in Section 3.7.5, the fringe data can also be used for estimating the rate of applied structural deformations. The output fringe frequencies are directly proportional to the rate of vehicle induced deformation in the pavement structures. Section 5.6 formulates the deformations induced by multiple axles from the single-axle pavement-deformation profile. The effect of axle separation and loading trends on output fringe counts is discussed in Section 5.7. Correction of the total fringe counts based on the Lorentzian model (above) is also discussed.

5.2 CULWAY System Verification

5.2.1 Introduction

The Single Lane CULWAY (SLC) system provides information on each passing vehicle including gross weight, axle configuration, axle distances, weight of each axle group and speed. The basic weighing mechanism is based on the use of a culvert as the transducer. Several strain sensors are mounted on the ceilings of an existing box culvert. The strain sensor positioning within a lane follows the guidelines outlined by Scott¹⁵⁸. The CULWAY system also includes two piezo-electric axle

detectors installed 10 metres apart from each other. A microprocessor based data acquisition and processing system acquires strain gauge and axle detector readings and processes them to estimate the vehicular parameters. The data and time logged vehicular information is registered automatically in the onsite computer system. The SLC system can be modified and configured as a Multi Lane CULWAY (MLC). Unlike SLC, the MLC system is normally used at a permanent site and requires mains power and telephone connection. The MLC computer system has a number of built-in performance monitoring and diagnostic facilities such as (a) automatic generation and faxing of a weekly status report to the site supervisors and (b) monitoring status of strain gauges and axle detectors.

5.2.2 Analysis of CULWAY Reliability

During field trials 12 heavy vehicles were selected and measured by a set of EMU, CULWAY and FFPI sensors at a single location (Pakenham, Victoria). This section compares the performances of the CULWAY and EMU systems. Figure 5-1 shows the weight of 12 vehicles measured by CULWAY as a function of EMU records. A very good linear fit gives a correlation (R^2) value of 0.99 for the CULWAY sensor.

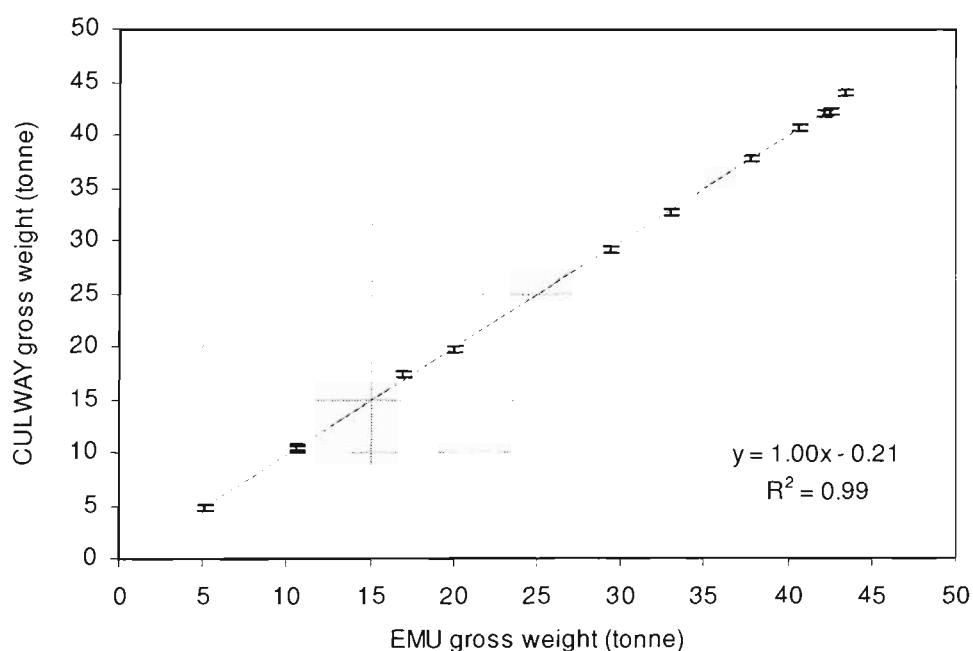


Figure 5-1: Gross vehicular weights recorded by CULWAY system as compared with those recorded by EMU system for identical vehicles.

The CULWAY calibration (within error margins of $\pm 2\%$) was obtained by investigating 12 truck signals. During the data processing time, it also identifies and records the number of vehicles missed by the data processing unit of the sensor. Therefore, the CULWAY system was used with confidence as the standard against which the FFPI WIM sensor was calibrated.

5.3 Field Sensor Installations

The FFPI sensors were installed in boreholes in an east-bound lane of the Princes Highway near an existing CULWAY site just outside Pakenham, Victoria. The sensors were laid in a 4-metre long aluminium U-section. The U-section was then filled with an epoxy for borehole installations at 800 mm below the road surface. The U-sections embedded within these boreholes were mechanically coupled to the surrounding sub-base by back-filling with a special cement grout. All the sensors were long enough for one lane sensing of the highway. A schematic of the sensor installation is given in Figure 5-2.

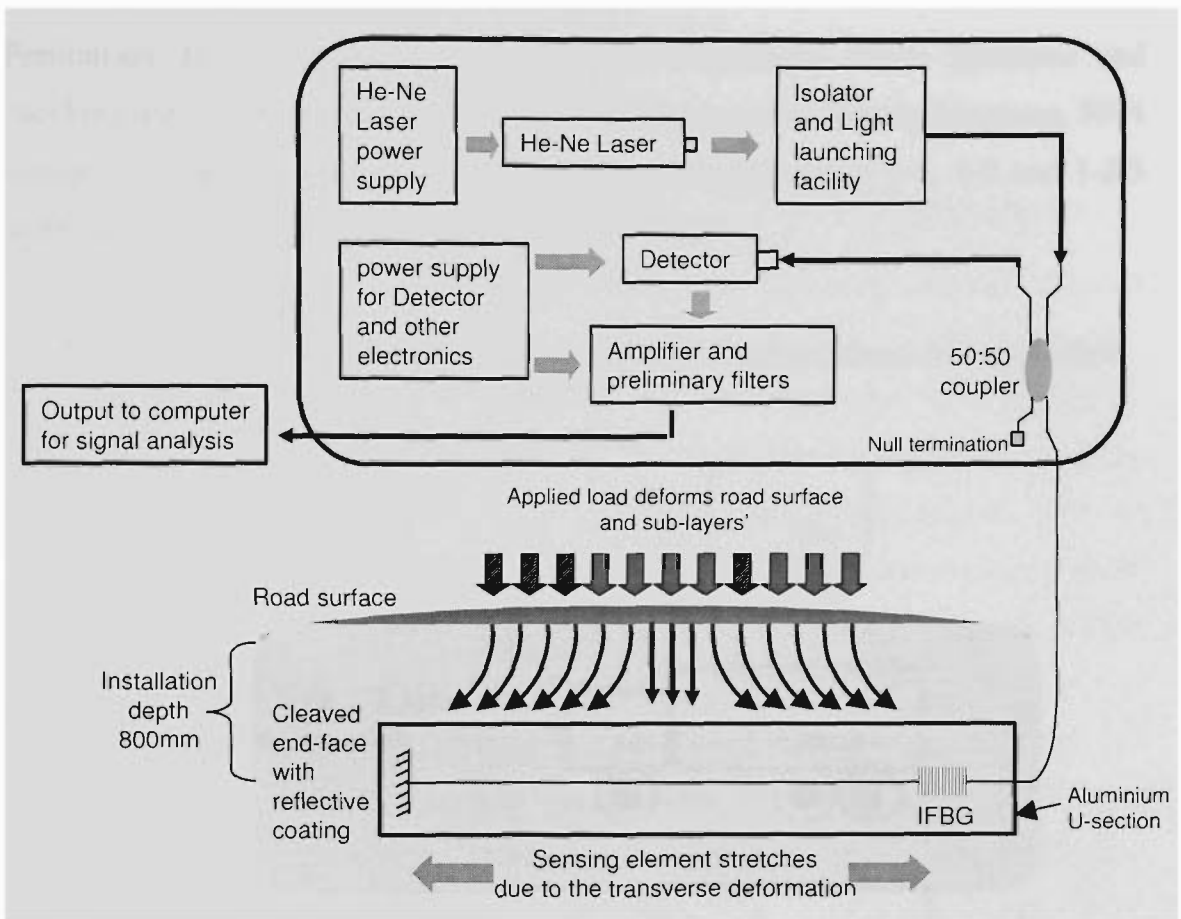


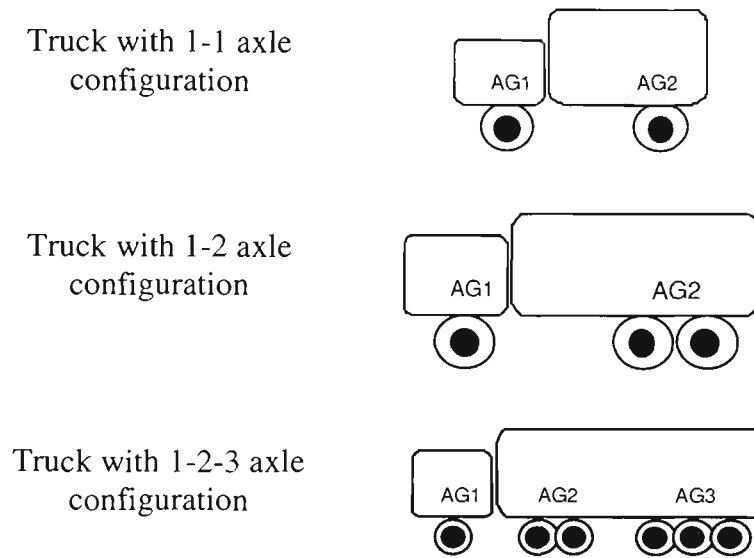
Figure 5-2: Schematic of FFPI sensor configured for the field tests showing installation details.

As with any optical system, the major challenges in the field are optical alignment, environmental insensitivity, ruggedness and maintenance of the whole assembly along with portability. It proved advantageous to place the launch and detection optics and electronics within a single metal box, with connectorised components wherever possible, so that the sensing elements could be attached and removed with ease in situ. The fibre components used for the assembly were carefully placed in appropriate fibre organisers. Also, care was taken to prevent the stabilised He-Ne laser from overheating.

A number of field trials of the FFPI WIM sensor were performed over several months, to gauge its accuracy and repeatability by comparison with independent WIM sensors installed at the Pakenham site.

Preliminary field trials were carried out for eliminating on-site problems and checking initial functionality of the overall sensor assembly. During this phase, FFPI sensor responses for trucks with typical axle configurations of 1-1, 1-2 and 1-2-3 were recorded. The terms are explained in Table 5-1.

Table 5-1: Explanation of trucks with various axle configurations. AG means Axle Group.



5.4 Error Sources

The FFPI strain sensor developed during this project is based on the fringe counting regime. As discussed in Section 3.7.3, the basic assumption is that Poisson's ratio is the dominant coupling mechanism to the sensor. For a given pavement material, Poisson's ratio is constant and typically ~ 0.4 . However, the Poisson's ratio changes due to variations in the loading frequency and temperature. Section 5.4.1 estimates the error in the total fringe counts due to these variations for various longitudinal (vertical) deformations.

The counting algorithm has a resolution of ± 1 fringe (Section 4.3). This error depends on capability of the program code to identify a group of points as a fringe. Moreover, the fringe shape is affected by random structural vibrations and electronic

filter response. The effect of fringe frequency and amplitude variations on estimating the total fringe counts is discussed in Sections 5.4.2 and 5.4.3 respectively.

5.4.1 Effect of Change in Poisson's Ratio on Total Fringe Counts

The loading frequency is a measure of how often a pavement undergoes loading and depends on the distance between axles and the speed of the vehicle. For example, consider a 1-1 axle configuration in which two axles are separated by ~ 1 m. If the vehicle moves with a speed of 1 m/s then, the time delay between the two axles reaching the sensing element is 1 s and hence the loading frequency is 1 Hz. In reality, each truck contains multiple axles and the distance between individual axles varies. Hence, the loading frequency changes significantly for a given truck, except for a 1-1 axle configuration moving with a constant speed. The axle distance and speed data for each truck were obtained from the CULWAY records. Table 5-2 shows the method for calculating minimum and maximum loading frequencies and the expected variations in the loading frequencies for 1-1, 1-2 and 1-2-3 axle configurations.

The variations in Poisson's ratio were determined from the plot shown in Figure 3-18 at 11, 25 and 40 °C¹⁵⁰. Table 5-3 shows the values of Poisson's ratio and corresponding variations in the fringe counts. At lower loading frequencies and temperatures (11 °C), as mentioned in Section 3.7.4, the value of Poisson's ratio was assumed as 0.4. However, at higher loading frequencies and temperatures the Poisson's ratio decreases. The minimum value of Poisson's ratio was obtained as 0.09 for the higher loading frequencies (~ 14 Hz). At higher temperatures (~ 40 °C) the Poisson's ratio changes for all the configurations. The data presented in this thesis were recorded near Melbourne, Australia in the month of January and February (summer season). Therefore, the approximate road temperature during daytime can be estimated to be in the range of 35 to 40 °C. Average total fringe counts for each axle configuration were calculated from Section 3.7.4 and shown in Table 5-3 for three different temperatures. Assuming constant average vehicular speed of ~ 21.5 m/s with average axle separation of 5.8 m (according to CULWAY records), a 1-1 configuration does not show any variations, as the loading frequency remains constant for constant pavement material temperature. However, significant

change is estimated for elevated temperatures of ~ 40 °C. For any given vehicle with 1-2 and 1-2-3 configurations, variation in the total fringe count is a maximum at 25 °C. This effect of change in pavement characteristics on the total fringe counts can be used to estimate the approximate variation in the correction factor for the sensor calibration based on the seasonal pavement conditions.

Table 5-2: Loading frequency calculations using vehicle speed and axle separation.

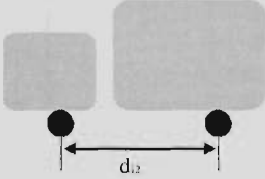
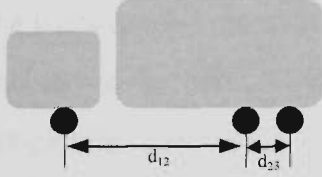
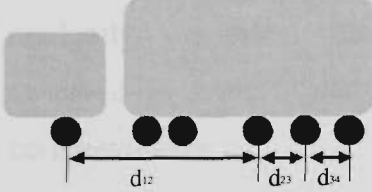
Axle configuration	Loading frequency calculations
<p data-bbox="243 691 555 724">Axle configuration 1-1</p> 	<p data-bbox="617 691 1110 724">Loading frequency (Hz) = [speed (m/s) / d_{12} (m)]</p> <p data-bbox="617 731 920 764">Speed range: 16 m/s to 22 m/s</p> <p data-bbox="617 771 997 804">Axle separation range: 4.1 m to 6.6 m</p> <p data-bbox="617 811 1202 844">Average loading frequency for 1-1 configuration = 3.7 Hz</p>
<p data-bbox="243 1001 555 1034">Axle configuration 1-2</p> 	<p data-bbox="617 1001 1218 1034">Minimum loading frequency (Hz) = [speed (m/s) / d_{12} (m)]</p> <p data-bbox="617 1041 1218 1074">Maximum loading frequency (Hz) = [speed (m/s) / d_{23} (m)]</p> <p data-bbox="617 1128 1310 1161">Average minimum loading frequency for 1-2 configuration = 4.6 Hz</p> <p data-bbox="617 1168 1333 1201">Average maximum loading frequency for 1-2 configuration = 14.1 Hz</p>
<p data-bbox="232 1335 571 1368">Axle configuration 1-2-3</p> 	<p data-bbox="617 1335 1218 1368">Minimum loading frequency (Hz) = [speed (m/s) / d_{12} (m)]</p> <p data-bbox="617 1375 1372 1446">Maximum loading frequency (Hz) = [speed (m/s) / minimum of d_{23} and d_{34} (m)]</p> <p data-bbox="617 1500 1325 1533">Average minimum loading frequency for 1-2-3 configuration = 3.0 Hz</p> <p data-bbox="617 1540 1325 1573">Average maximum loading frequency for 1-2-3 configuration = 15.5 Hz</p>

Table 5-3 : Variations in the total fringe counts estimated at various loading frequencies and Poisson's ratios at three different temperatures.

Truck axle configuration	Loading frequency (Hz)	Poisson's ratio at various temperatures			Average total fringe counts calculated for pavement deformation of 0.01 mm using Equation 3-14 at various temperatures		
		11°C	25°C	40°C	11°C	25°C	40°C
1-1	3.7	0.40	0.40	0.15	92	92	35
1-2	Min = 4.6	0.40	0.40	0.15	92	92	35
	Max = 14.11	0.40	0.25	0.09	92	58	21
1-2-3	Min = 3.0	0.40	0.40	0.12	92	92	28
	Max = 15.49	0.40	0.25	0.09	92	58	21

5.4.2 Fringe Frequency Noise

Random variations in the fringe frequency were absent in the data recorded during the trials carried out under a controlled laboratory environment; however in the field, this is not the case. As discussed in Section 3.7.5, fringe frequency depends on the frequency of structural deformation. Significant frequency variations observed in all field data sets suggest that the pavement structure suffers from random deformations at various rates during the truck passage. As the vehicle approaches the sensing element, the frequency of the fringes gradually increases and as the vehicle bounces randomly, the fringe frequency varies accordingly. Such noise was typically observed in most of the fringe data during rapid and random transitions from compression or relaxation of the pavement material.

Figure 5-3 shows how typical frequency noise affects the fringe frequency by 50% at the start of the data trace before the first axle arrives on the sensor. Some evidence of frequency noise was also observed in the fringe data recorded between the passage of more than two individual axles combined as a single axle group. Each axle in an axle group has its own dynamic motion which induces random deformations in the pavement. A typical axle group of three axles clearly shows such frequency noise, i.e. around 50 to 60% variations in the fringe frequency (Figure 5-4).

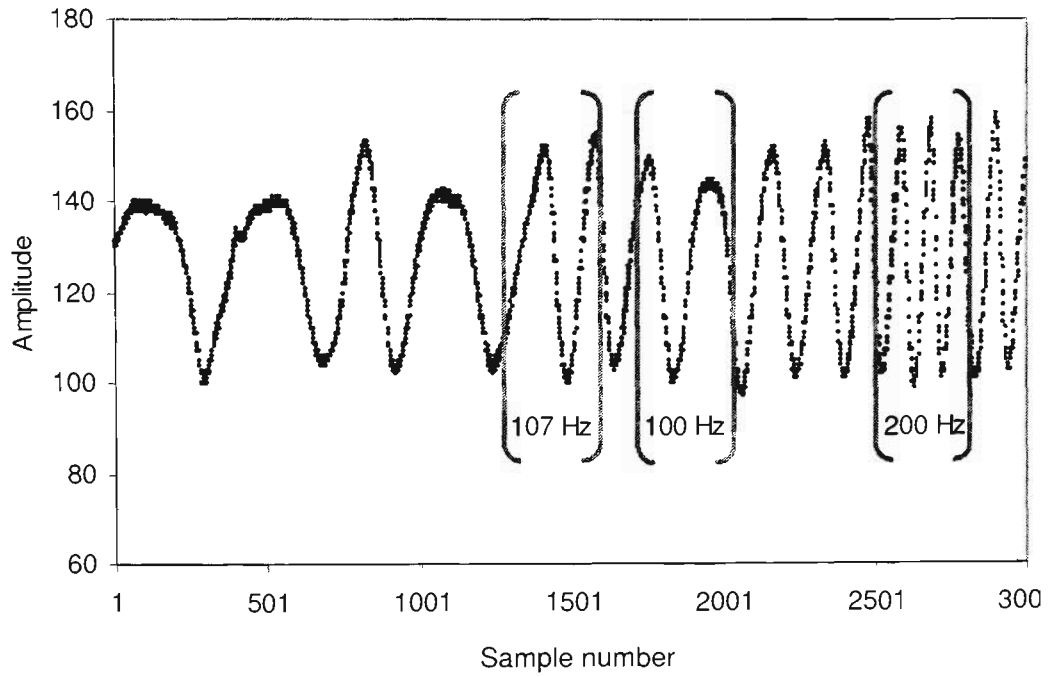


Figure 5-3: Example of the FFPI data trace showing how random phase noise resulted in around 50% variation in the fringe frequency.

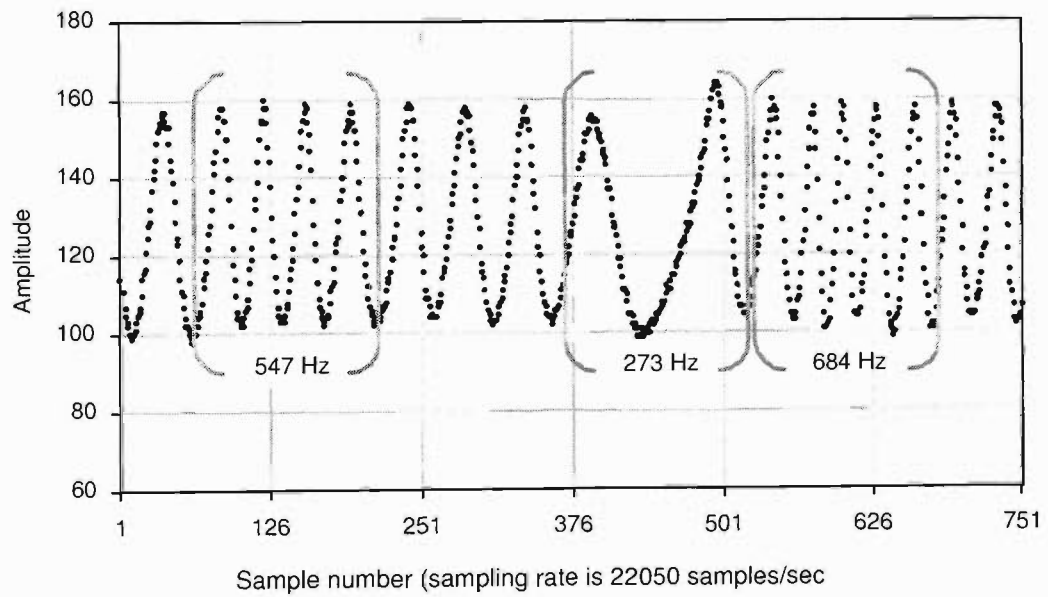


Figure 5-4: FFPI sensor data recorded during the compression induced by the third axle group which consisting of three axles. The phase reversal of the pavement deformation alters the fringe frequency by 50 - 60%.

As discussed in Section 3.7.5, the fringe frequency is directly proportional to the rate of structural deformation. Therefore, the random fringe frequency variations observed in the field data results from abrupt vehicle induced deformations in the pavement structure.

5.4.3 Amplitude Noise

Amplitude noise was mainly observed in the fringe data obtained at the start of a compression or relaxation cycle. This resulted from the combination of (a) the frequency dependence of the electronic filtering circuitry and (b) random or rapid phase reversal of the pavement deformation (Figure 5-5) especially evident from truck bouncing. If the truck is bouncing, and the frequency of bouncing is in phase with the lateral deformation of the pavement, then sudden variations in the fringe frequency are possible and were observed in many data sets. The detector bandwidth limitations (30 Hz – 50 kHz) affect these frequency variations and result in amplitude variations.

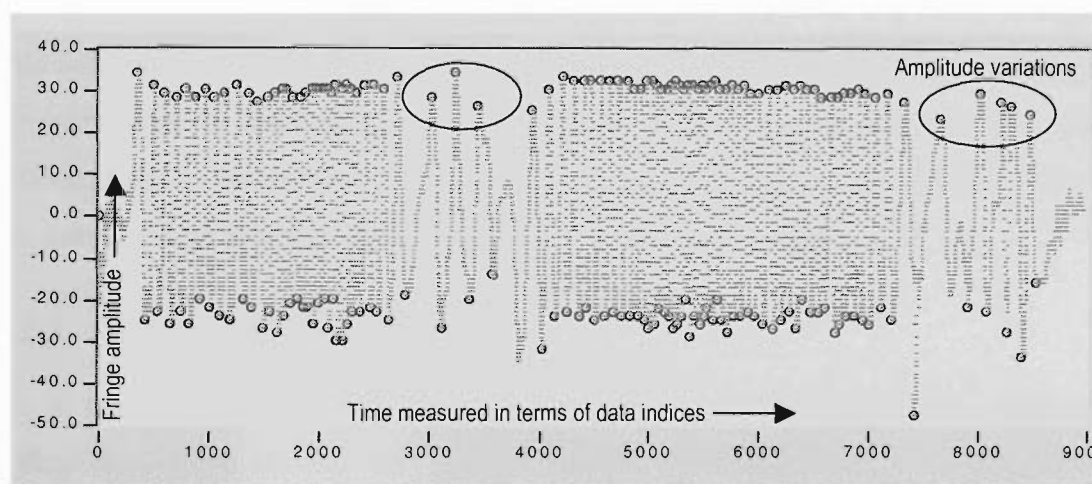


Figure 5-5: Example of FFPI data, showing how amplitude noise in the field data is mainly observed during a phase reversal of the pavement material.

The fringe frequencies ranging from 10 Hz to 100 Hz are comparable to the lower cut-off frequency of the electronic filtering circuit. As the truck approaches the sensing region, the fringe frequency gradually increases (Figure 5-6). During this period, the bandwidth of the electronic filtering circuit affects the amplitude of low frequency fringes, introducing amplitude noise in the fringe patterns. The threshold

for fringe counting can be defined manually so as to largely reject errors arising from the amplitude noise.

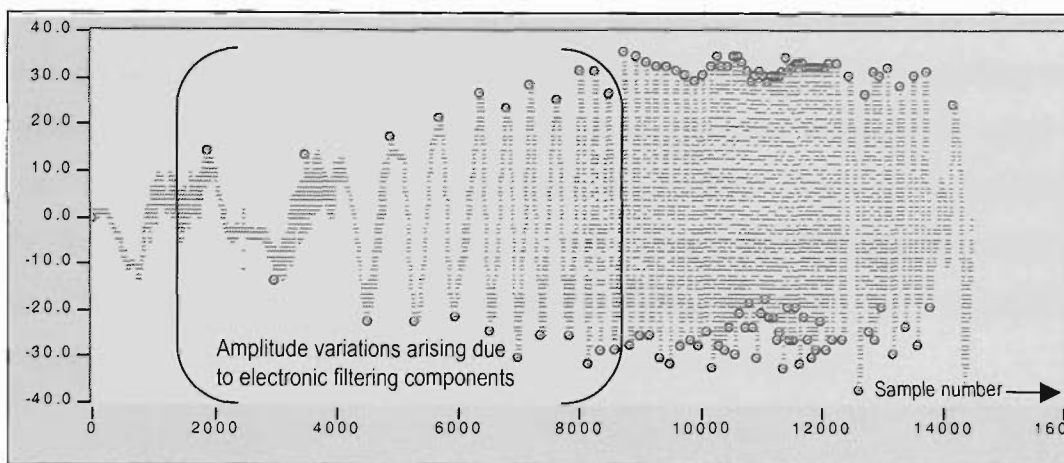


Figure 5-6: Fringe amplitude variations were observed as a truck approached the embedded FFPI sensing element

5.5 Assessing Viability for WIM Sensing

The field version of the FFPI sensor, a 4 m gauge length embedded 800 mm deep in the subgrade, is expected to output optical fringes proportional to the lateral deformations in the subgrade structure. This section provides a general discussion of the output fringe patterns and gross features of the sensor output.

5.5.1 Output Fringe Patterns

As a truck travels along the highway, the moving multi-axle load induces a deformation-wave in the road that propagates with the truck, imparting to the underlying road layers a combination of compression and expansion and shears in three dimensions. The road is designed to suffer negligible damage from individual vehicles. Therefore it is possible to conclude that the vehicle-induced strains are small compared to the plasticity limit for the road base. Also, within the multi-layered pavement structure, the characteristic time scales of the resultant structural disturbance are lower than the propagation time of the disturbance from one layer to an other. Hence, the amplitude for all strain components is expected to vary

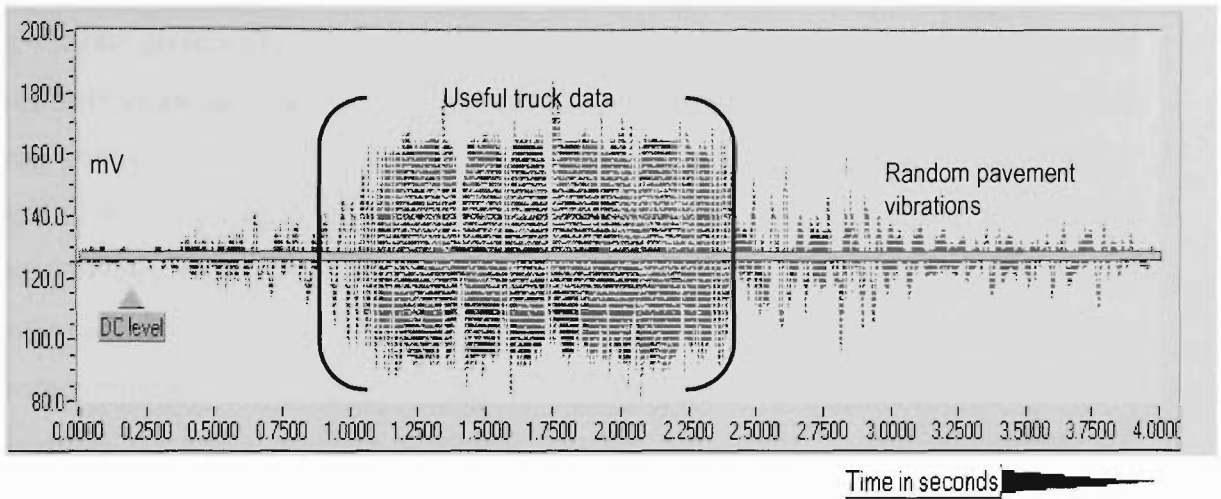
approximately linearly with the applied load. Thus, as explained in Section 3.7.2, if the loads for all wheels were doubled, all else being unchanged, the resulting strain-wave amplitude would be expected to double.

Hence, primarily it might be construed that the total amplitude of the travelling wave should scale linearly with the aggregate axle load. However, it should be noted that the travelling wave is actually a superposition of various stress fields excited by individual axles, so a load redistribution would change the travelling wave pattern, even if total (aggregate) load was unchanged. Hence, the strain-wave amplitude is not expected to vary exactly linearly with aggregate truck weight.

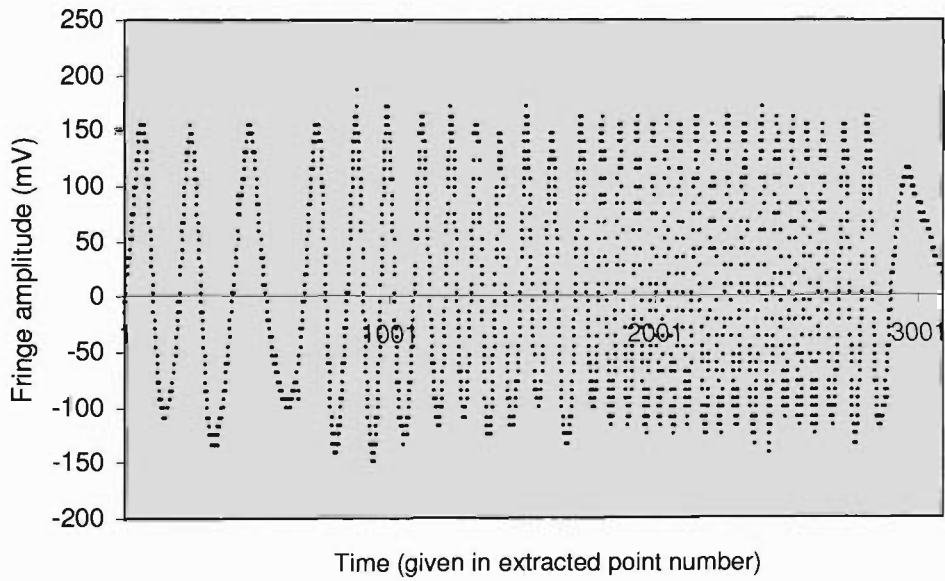
There is mechanical damping in the surface and sub-layers due to microscopic energy dissipation by electro-chemical inter-particle forces and interstitial fluid-substrate interactions. The stress distribution of a typical pavement material at various depths and under the action of a heavy vehicle was discussed in Section 3.7.4. This damping is unavoidable and necessary in any case, or else roads would vibrate excessively and be damaged. The damping is expected to introduce a variable dynamic component to the travelling wave, that will alter the form of the wave for different truck velocities, for example. As a first approximation, however, the velocity-dependent component could be regarded as a relatively small perturbation to the quasi-static strain distribution that would result from a stationary truck.

The concept of fringe groups associated with structural compression and relaxation was discussed in Section 3.7.2. The total load on the pavement exerted by a moving vehicle is the sum of the individual static loads induced by each axle of that truck and the forces generated by the dynamic action of the truck movement. Choosing a suitable sensor-installation site can reduce the possibility of generating tractional forces due to acceleration, deceleration and turning movements of the vehicle. However, vehicle induced dynamic effects will affect the sensor behaviour despite of the choice of the installation site. Figure 5-7 shows typical FFPI fringe data recorded during a truck passage (axle configuration 1-2-3). The sensor has recorded the data

for 4 seconds. A close view of the ‘useful data’ associated with truck showing individual fringe quality is presented in Figure 5-7.



(a)



(b)

Figure 5-7: (a) Typical FFPI fringe data obtained as a 1-2-3 truck passed over a sensor (b) Detailed view of the ‘useful’ fringe data showing individual fringe quality.

5.5.2 Formation of Fringe Groups

The “useful” portion of Figure 5-7 is reproduced in greater detail in Figure 5-8. These data show that the truck-trace recorded using the FFPI WIM sensor consisted of various groups of fringes. The fringe-group FG1 (in Figure 5-8) is induced by the first axle of an approaching vehicle and represents pavement compression. The small time interval between the end of the first fringe group, FG1, and the start of the second fringe group, FG2, represents the approximate time during which the axle was directly over the sensor. In other words, this also represents the amount of pavement deformation due to the arrival of that particular axle. The axle positions were confirmed in a field test by the use of axle detectors. Similarly, FG3 and FG4 represent the corresponding pavement compression and relaxation induced by the second axle group. A similar fringe-group-trend was obtained from the third axle-group (not shown in Figure 5-8).

Theoretically, as discussed in Section 3.7.2, for an ideal isolated single axle, FG1 and FG2 should consist of the same number of fringes because, pavement compression (assigned to FG1) and relaxation (assigned to FG2) should be of similar magnitudes. Previous studies¹⁴⁴ of optical fibre weigh-in-motion sensors based on polarimetric fringe patterns found that the similar number of fringes was observed for increasing and decreasing load. However, Figure 5-8 shows that the number of fringes in FG1 is not equal to (greater than, in all cases) the number of fringes in FG2. When an axle approaches the sensor, the fringe groups associated with the neighboring axle-group overlap with it to form a complex axle signature; as discussed in Section 3.7.2.

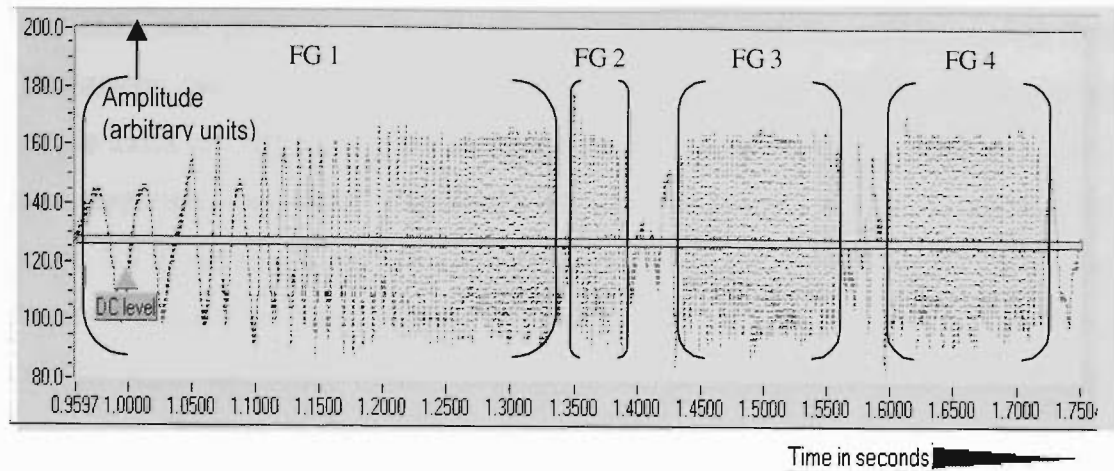


Figure 5-8: A close look at a typical 1-2-3 truck trace from Figure 5-7 showing the first four fringe groups (FG1, FG2, FG3 and FG4).

In addition, the sensor output is also affected by the non-linear behaviour of the pavement material¹⁵⁹ under the action of a dynamic strain.

Hence, a truck configuration with 1-1 axle configuration will result in four overlapping fringe groups. A truck with axle configuration 1-2 (i.e. total three axles with each axle producing two fringe groups) will give rise to six overlapping fringe groups. Therefore, the overlapping nature of the fringe patterns implies that a truck with a complex axle configuration will produce more complicated combinations of fringe-groups. One of these complex patterns (Figure 5-9) shows the fringe data of the heaviest truck (61.9 tonnes, as recorded by the CULWAY system) with an axle configuration of 1-2-3-3 and 524 fringes recorded by the FFPI-WIM sensor.

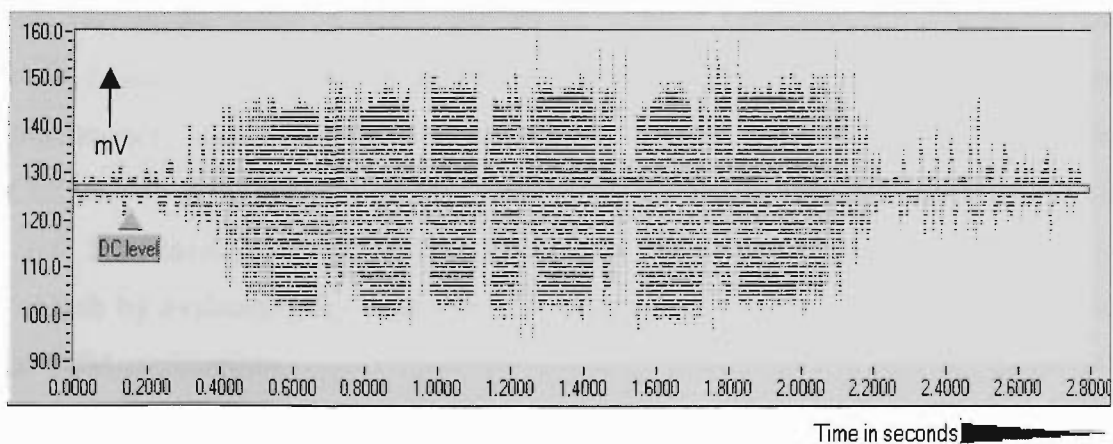


Figure 5-9: FFPI fringe data produced by the heaviest vehicle during these measurements, illustrating the complexities of such data.

Thus, each axle produces a non-localised deformation of the sublayers, and these deformations can overlap at the depth of the sensor. In the overlap regions, where multiple axles are influencing the sublayers, the road does not relax back to its initial state completely, especially if the axles are closely spaced. Hence, as discussed in Section 3.7.2, we might expect a reduction in fringe number during the incomplete relaxation and compression phases between closely spaced axles. Moreover, this is likely to affect the fringe counts obtained from heavy vehicles with many closely spaced axles more than those obtained from light vehicles with a few widely spaced axles.

The fringe-groups observed were formed by extension and relaxation of the FFPI sensor due to the compressive load-wave induced by various axles of the truck. The first axle of the truck shows more distinct fringe groups because there is minimum interference from any of the other axles. Also the weight of the first axle is almost constant. Thus, as the number of axles in an axle-group (closely placed number of axles) increases, the complexity of the interaction among the individual axle-fringe-groups increases. The resultant complex fringe patterns reduce the number of fringes per axle by the process of overlapping, and introduce errors in the fringe detection process and hence in the total fringe counts (more details in Section 5.7.3). Apart from these inherent error sources, other influencing factors are discussed in Section 5.4.

This section discusses an initial attempt to calibrate FFPI sensor based on the total fringe counts. Furthermore, it also gives an opportunity to compare the FFPI sensor performance with an existing non-fibre commercial WIM sensing system (CULWAY). The analysis of the CULWAY reliability was described in Section 5.2.2. This investigation will lead to the most important milestone of the present research by evaluating the feasibility of the proposed single transducer FFPI sensor for WIM applications.

5.5.3 FFPI Calibration using CULWAY Sensor

The first field trial occurred on 23 January 1998 at the Pakenham site. This site was located next to an existing CULWAY WIM sensing unit. The sensor was calibrated by comparing its output with the output of the CULWAY system. A bore-hole sensor used for this trial was installed 800 mm under the road surface. A total of 35 truck traces were recorded. The total number of fringes was counted for the truck traces to correlate the fringe count with gross weight of the truck. Figure 5-10 shows a plot of the number of fringes recorded by the borehole sensor as a function of the gross vehicular weight as recorded by the CULWAY system. The two quantities demonstrate a linear correlation between them.

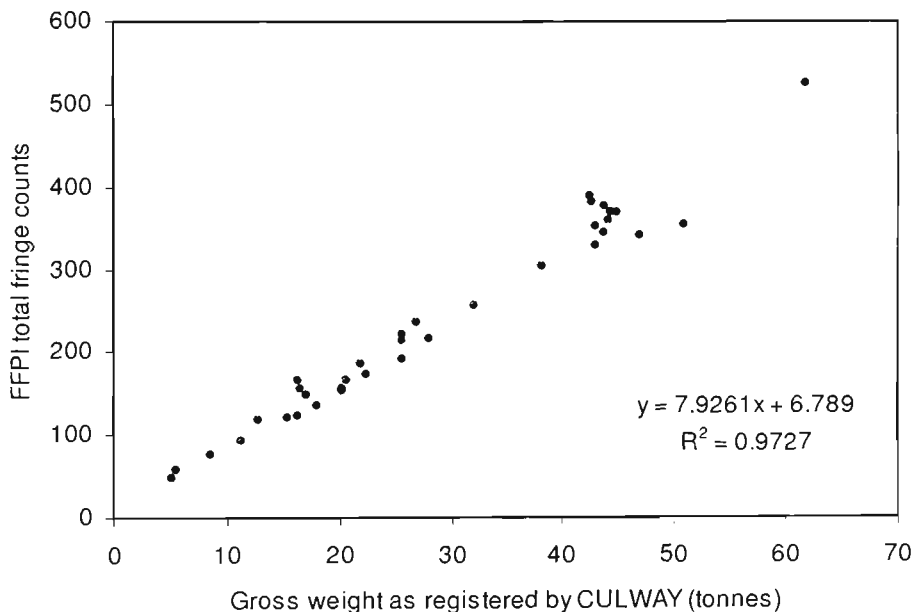


Figure 5-10: Calibration of FFPI sensor based on 35 trucks, by comparing detected total fringe-counts with gross vehicular weights recorded by CULWAY sensor.

A regression analysis showed an R^2 value of around 0.97 for the truck data indicating a reasonably good fit and resulted in the following function;

$$\text{Fringe\#} = [(\text{wt. of truck in tonne}) \times (7.9 \pm 0.2)] + (6.8 \pm 7.4)$$

The offset of about ± 7 fringes was possibly due to the random drifts in the sensor or the pavement conditions on that day (as discussed in Section 5.4.1), and represents less than 10% of the total fringe count for a 10 tonne vehicle. The errors in the total

fringe counts due to the variations in Poisson's ratio for a typical pavement material were estimated in Section 5.4.1. Also, assuming a constant pavement temperature of 40 °C, from Table 5-3, loading frequency dependent variations in Poisson's ratio can affect the total fringe counts by around 7 to 14 fringes depending upon the truck axle configuration. This agrees well with the variations of the total fringe counts observed during these measurements. Therefore, this device provides a reasonable prediction of truck weight. The error of ± 7 fringes introduces maximum error of $\sim 14\%$ for lighter vehicles of ~ 5 tonne and less for heavier vehicles. This is verified by plotting the data from Figure 5-10 as a calibration factor (fringes per tonne) against the vehicle weight (Figure 5-11). It is noted that the RMS offset in the fringe count has a greater proportional effect in the case of smaller vehicular counts rather than large ones. The calibration factor increases for smaller vehicles to around 10.0 fringes per tonne. The RMS offset in the fringe count can be obtained from the intercept in the calibration factor axis in Figure 5-10. If this RMS offset is subtracted from the fringe counts for obtaining reliable fringe counts, the scatter in the distribution of the "compensated" calibration factor is found to be somewhat flatter with increasing truck weights, as seen in Figure 5-11.

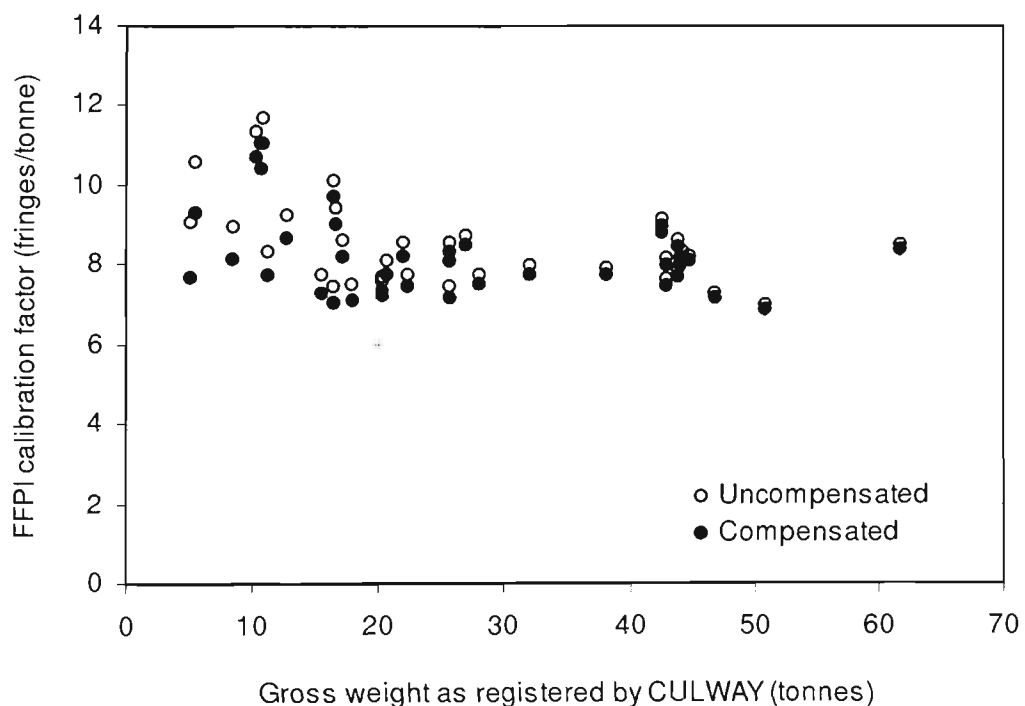


Figure 5-11: Data from Figure 5-10 replotted as an uncompensated (and compensated) calibration factor as a function of vehicle weight.

Figure 5-12 shows a plot of the total number of fringes recorded by the borehole sensor as a function of the gross vehicle weight as recorded by the CULWAY system during two different field tests. This data set contains 126 trucks of various axle configurations. The two quantities demonstrate a linear correlation between them with correlation factor (R^2) of 0.94. Regression analysis of the data set shows the standard error was ~ 24 fringes. This represents an error of $\sim 24\%$ for the lighter trucks weighing ~ 10 tonne. In case of the heavier vehicles, in the range of 40 tonne, the error reduces to $\sim 6\%$. As mentioned in Section 2.5.4, this error range of $\sim 20\text{--}50\%$, is comparable with conventional single transducer fibre/non-fibre WIM sensing systems. The secondary Y-axis in Figure 5-12 shows the corresponding transverse pavement strain calculated from the total fringe counts (for a 4 m sensing length, 1 fringe $\equiv [(0.273 \times 10^{-6} \text{ m}) / (4 \text{ m})] = 0.068 \mu\epsilon$ in the transverse direction). The longitudinal pavement strain was calculated by using the transverse pavement strain and Poisson's ratio of the pavement as 0.4 (see Section 3.7.4). Note that although Poisson's ratio changes with temperature and loading frequency, it was assumed to be constant for these calculations. Figure 5-12 shows the plot of longitudinal (vertical) pavement deformation as a function of CULWAY gross weights. The secondary X-axis suggests that the deformation of the pavement surface is in the sub-millimetre range. This agrees with the data published by other researchers¹⁵³. The complexities involved in quantifying this parameter were discussed in Section 3.7.4.

The FFPI sensor was calibrated by comparing it with the CULWAY system to test its viability for WIM applications. This investigation suggests that the FFPI sensing system developed during this research has potential for WIM sensing. The study revealed encouraging basic sensor characteristics of accuracy and repeatability. The outcomes of each field trial are discussed in Sections 5.5.3 and 5.5.4.

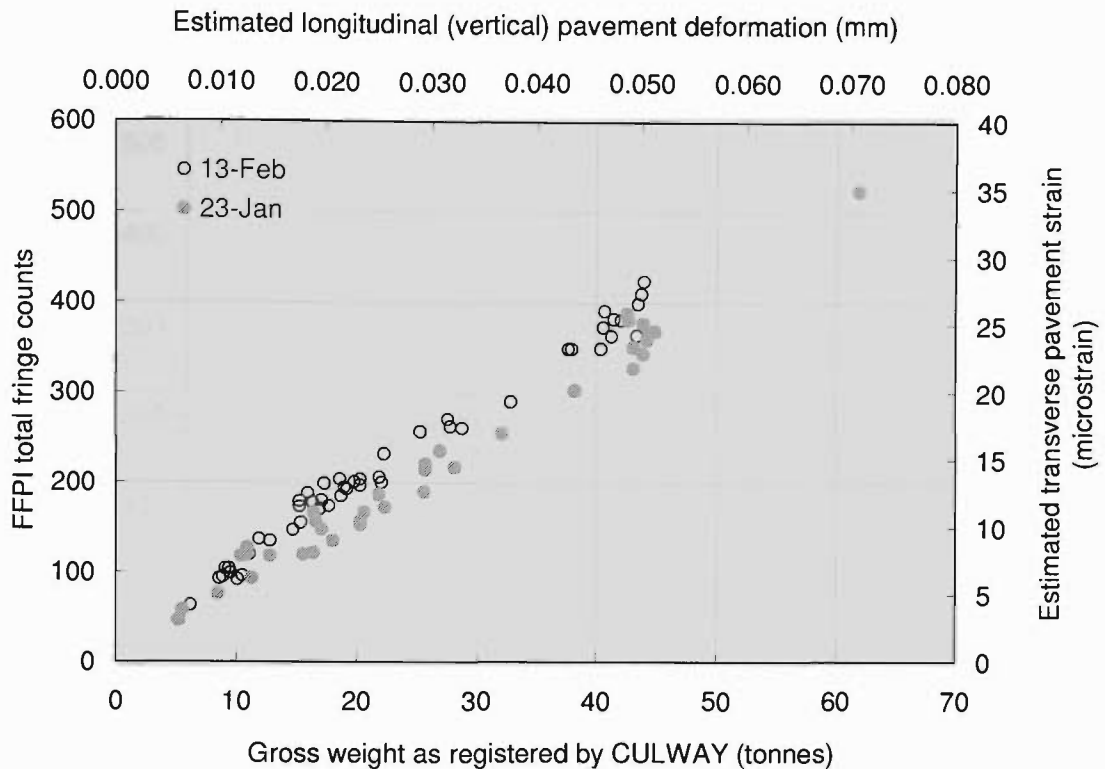


Figure 5-12: Estimation of vertical (secondary X-axis) and transverse (secondary Y-axis) pavement deformations from the graph of total fringe counts (primary Y-axis) plotted as a function of gross truck weights (primary X-axis) recorded by the CULWAY system.

5.5.4 Tests of Repeatability of FFPI Calibration Procedure

The second field trial also provided an opportunity to confirm the repeatability of FFPI sensor response and, furthermore, it also allowed testing of the cross-correlation of the characteristics of FFPI-EMU (Electronic Mass Unit); FFPI-CULWAY and CULWAY-EMU. Truck data of various axle configurations were recorded and saved on disk. These saved files were processed using the algorithm developed during this project to obtain fringe counts, fringe indices and the fringe frequencies. A total of 91 truck traces were recorded during this trial. Figure 5-13 shows the fringe count results of 91 trucks as compared with the gross weights recorded by the CULWAY system.

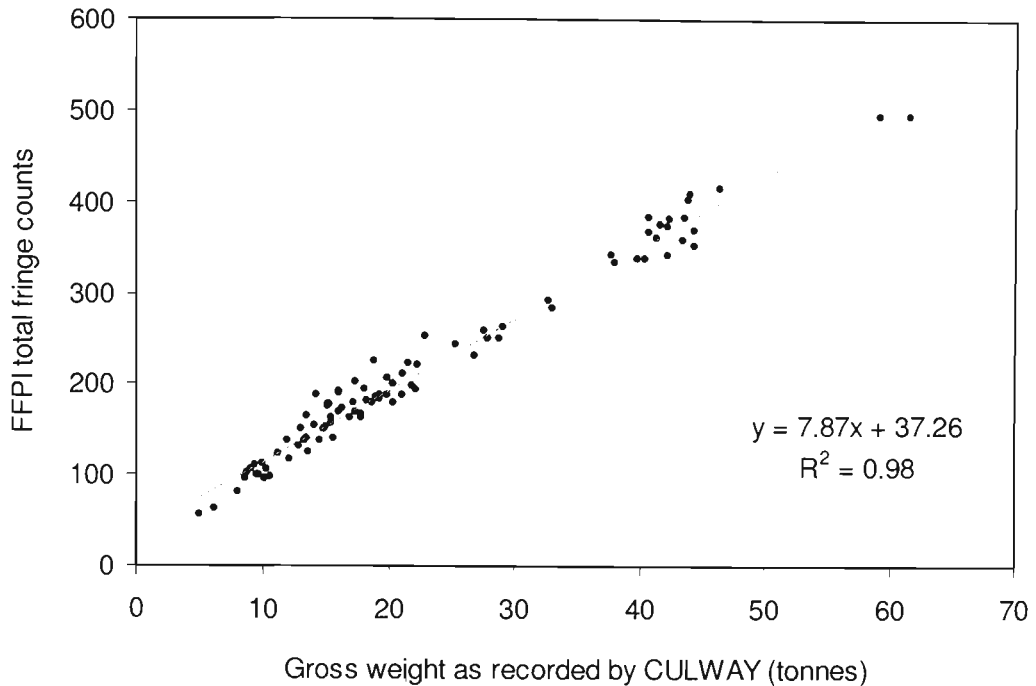


Figure 5-13 : FFPI total fringe count calibration for 91 trucks recorded during the second field trial.

The graph (Figure 5-13) shows the fringe counts as a function of vehicle weight for 91 records. The two quantities demonstrate a linear correlation between them. The calibration results in a gradient of 7.8 fringes per tonne, with a residual fringe count of 37.25 that differs from that of the first tests (7 fringes) significantly. These discrepancies are expected mainly because of variations in pavement properties and its dependence on the surroundings, especially temperature, as explained in Section 5.4.1.

Figure 5-14 shows a plot of the calibration factor (fringes/tonne), derived from the data in Figure 5-13, as a function of gross vehicle weight recorded by the CULWAY system. This plot indicates gross weights of vehicles in the range of 5 to 60 tonne, and shows that the calibration factor decreases with increasing gross weight of the vehicle. A similar trend was observed during the first trial (Figure 5-11). The nonlinearity in the variation of the calibration factor is due to the nonlinear response of the pavement under the action of dynamic forces and also due to the overlap of pavement responses to multiple axles. It is also clear from the same plot that there is

a large scatter in the fringe counts at the lighter end of the X-axis (weight in tonnes as measured by the CULWAY sensor). The variation in the calibration constant for various truck configurations is discussed in Section 5.5.6. Moreover, both field tests confirmed that (a) this single-transducer FFPI sensor has potential for WIM application, (b) there is good repeatability in the results and (c) the fringe count technique is suitable for estimating the weights of vehicles within error margins of ~ 10-15%. Similar error margins were observed for single-transducer WIM systems published elsewhere¹⁴³.

In Figure 5-14 non-loaded 1-2-3 configurations and loaded 1-1 and 1-2 configurations although of comparable gross weights in fact have different calibration factors. Therefore, the fringe count offset results partially from the fitting of a straight line to the nonlinear trend of calibration factor (fringes/tonne) as a function of CULWAY gross weights.

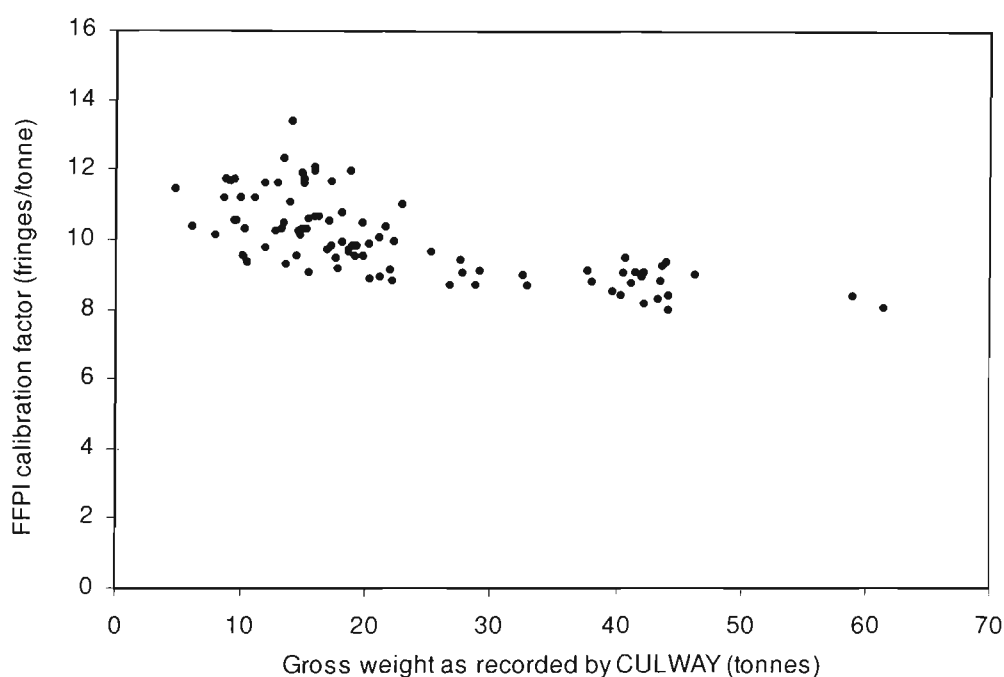


Figure 5-14: FFPI calibration factor, for the data in Figure 5-13 as a function of gross vehicular weight recorded by the CULWAY sensor, showing nonlinear trend.

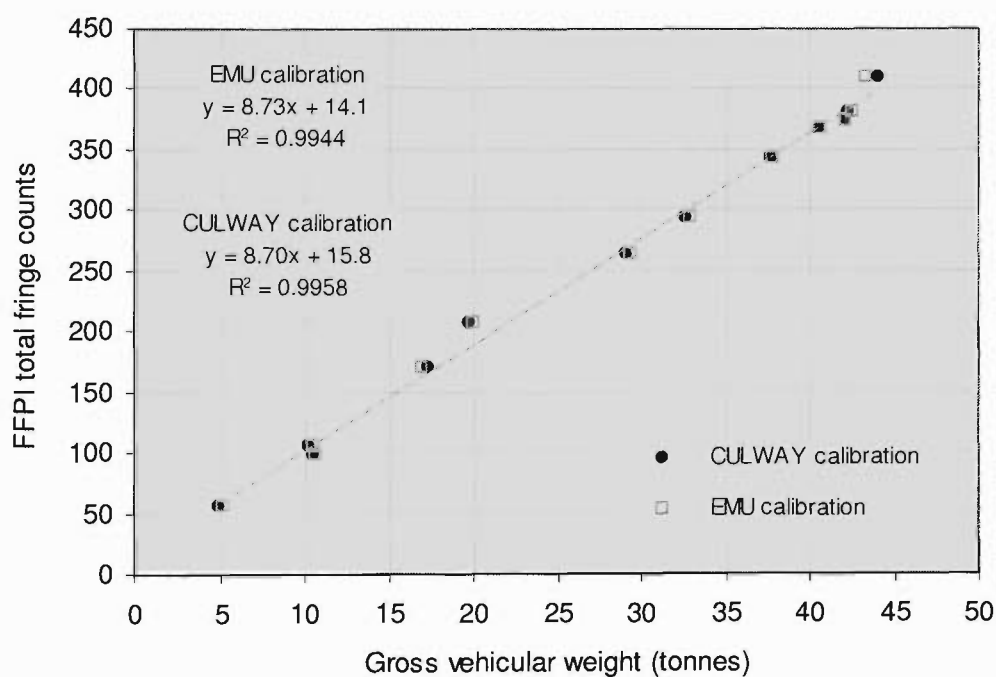
5.5.5 FFPI Calibration using EMU Sensor

This section describes the calibration of the FFPI based on the total fringe count results as compared with the EMU (Electronic Mass Unit) sensor. The EMU sensor was situated a few kilometres away from the FFPI sensor site. Trucks with heavy weights were selected from the regular traffic for EMU gross weight measurements. Trucks weighed by the EMU system were recognised at the FFPI sensor site by identifying the number-plate forwarded by a mobile phone call from a person at the EMU site. This trial allowed evaluation of the FFPI sensor by comparing its performance with the EMU data.

The EMU system recorded the 12 trucks, a few kilometres west at the VicRoads Weigh-bridge Site. The same trucks were spotted at the test site and were recorded by CULWAY and FFPI sensors. These truck traces were considered as reliable truck data. Table 5-4 shows the reliable truck data as recorded by FFPI, CULWAY and EMU at the Pakenham CULWAY Site. Furthermore, the table gives a brief idea of the variation in the calibration factor (fringes/tonne for FFPI sensor and tonne/tonne for CULWAY) as compared with EMU sensor. The standard deviation of the calibration factor for CULWAY as compared with EMU is 0.02 tonne/tonne. However, the FFPI sensor has a standard deviation of 0.67 fringes/tonne in the calibration factor as compared with EMU records. The calibration factors of FFPI sensor obtained by comparing with CULWAY (9.57 fringes/tonne) and EMU (9.49 Fringes/tonne) do not vary significantly. A plot of FFPI fringe counts versus gross weight as recorded by CULWAY and EMU (Figure 5-15) show the expected linear trend.

Table 5-4 : Reliable truck data; FFPI comparison with EMU.

CULWAY Time	EMU Total Weight (tonne)	FFPI Fringes	CULWAY Total Weight (tonne)	Calibration Factors		
				FFPI / EMU	CULWAY / EMU	FFPI / CULWAY
11:27:11	32.97	293	32.6	8.89	0.99	8.99
10:48:46	20.02	207	19.8	10.34	0.99	10.45
11:14:27	10.52	106	10.3	10.08	0.98	10.29
10:38:43	10.61	98	10.5	9.24	0.99	9.33
11:15:21	29.33	264	29.1	9.00	0.99	9.07
11:25:18	16.96	170	17.3	10.02	1.02	9.83
10:51:50	40.67	367	40.6	9.02	1.00	9.04
10:37:30	37.83	343	37.7	9.07	1.00	9.10
11:10:27	42.53	382	42.3	8.98	0.99	9.03
11:24:36	5.16	56	4.9	10.85	0.95	11.43
10:55:52	43.35	410	44	9.46	1.01	9.32
10:53:01	42.2	375	42.1	8.89	1.00	8.91
				Fringes / tonne	Tonnes / Tonne	Fringes / tonne
Average				9.49	0.99	9.57
Std Deviation				0.64	0.02	0.78

**Figure 5-15 : Linear variation of FFPI total fringe counts as compared with gross vehicular weights recorded by CULWAY and EMU systems.**

The regression analysis (Table 5-5) of the FFPI data obtained by comparing it with the EMU data shows that the value of R^2 is 0.99, which results in a better linear fit than the first field trial ($R^2 = 0.97$), as discussed in Section 5.5.3. This may be

because the number of vehicles tested during this field trial for EMU calibration (12 reliable vehicles) was much less than that of the first field trial (total of 35 vehicles).

Table 5-5 : Microsoft Excel Regression Analysis for Fabry-Pérot fringes versus EMU total weight.

Regression Statistics	
Multiple R	0.99
R Square	0.99
Adjusted R Square	0.99
Standard Error	9.86
Observations	12

	Coefficients	Standard Error	Lower 95%	Upper 95%	Lower 95%	Upper 95%
Intercept	14.14	6.42	-0.17	28.45	-0.17	28.45
EMU weight	8.73	0.21	8.27	9.20	8.27	9.20

Figure 5-16 shows the FFPI calibration factors (fringes/tonne) (from Table 5-4) as function of the weights obtained for the EMU and CULWAY sensor systems. The comparatively flatter linear distribution for the EMU sensor data shows its more consistent calibration factor. It is again clear from this analysis that the FFPI sensor is capable of estimating gross weights of trucks. This shows a calibration factor of around 10.4 fringes/tonne based on the EMU sensor, with the data set compensated for background fringe counts.

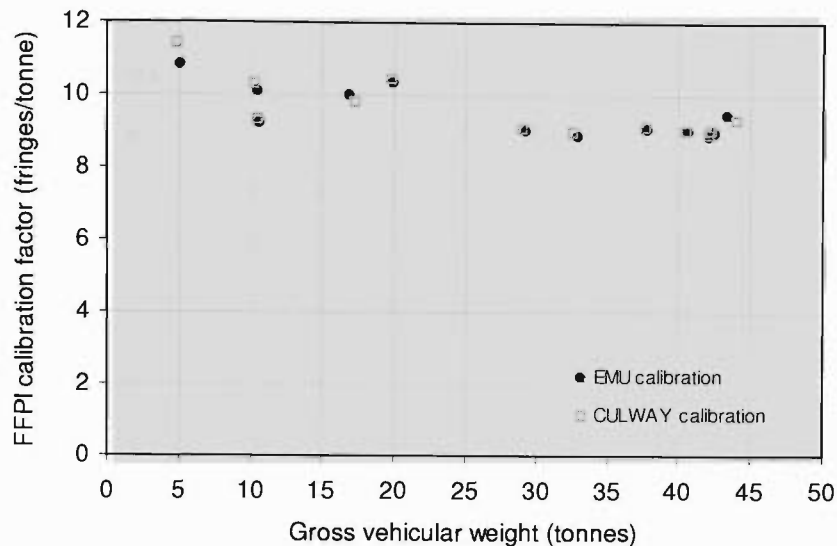


Figure 5-16: Variation in FFPI calibration factors (from Table 5-4) for 12 trucks as compared with EMU and CULWAY sensors.

5.5.6 Analysis of the FFPI Calibration based on the Axle Configurations

It was observed in all the field trials that the calibration factor is susceptible to variations in the axle configurations. This section quantifies the axle-dependent nature of the calibration factor. Only three types of standard axle configurations (configuration 1-1, 1-2 and 1-2-3) were chosen for this analysis. Figure 5-17 shows the trend of the calibration factor for various axle configurations as a function of the gross weight recorded by CULWAY sensor. The average calibration factor observed for a 1-1 configuration was ~ 11 fringes/tonne with significant scatter which may be because light vehicles tend to bounce more than heavier vehicles.

A separate investigation was carried out during this research in which FFPI fringe counts were recorded for an empty (weighing = 14.36 tonnes) and a loaded (weighing = 41.88 tonnes) 1-2-3 truck passing over a sensor embedded ~ 500 mm below the road surface. The results showed greater scatter in the calibration factor (fringes/tonne) of 16% for an empty truck records as compared with those of a loaded truck of 4%.

Similar scatter was observed in a 1-2 configuration with an average calibration factor of around 10 fringes/tonne. However, the 1-2-3 configuration showed an average calibration factor of about 9 fringes/tonne with comparatively less scatter in the data. Similar distribution of the calibration factor (fringes/tonne) with increasing gross vehicle weight was observed in the first field trial and presented in Figure 5-11. The next section describes a detailed analysis of the FFPI response to an individual axle and a group of axles.

The variation in the calibration factor, especially due to axle configuration, is the motivation for the more sophisticated fringe counting model of Section 5.7

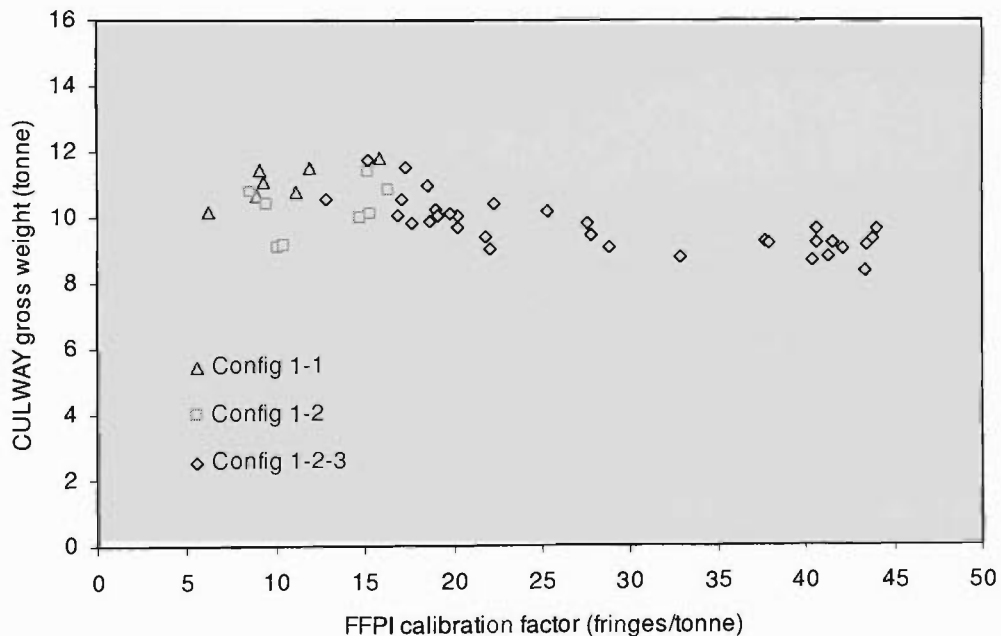


Figure 5-17: Variations in the calibration factor as a function of CULWAY gross weight for three different axle configurations.

5.6 Analysis of Single Axle Pavement Deformation Function

5.6.1 Introduction

Figure 5-18 shows details of the data presented in Figure 5-7(a) and the fringe frequency variations are clearly visible. As discussed in Section 4.4.4, the fringe frequency is maximum at the highest slope of the applied deformation function. Also

the rate of fringe frequency depends on the rate of deformation. Therefore, fringe frequency information is important for estimating the pavement deformation profile.

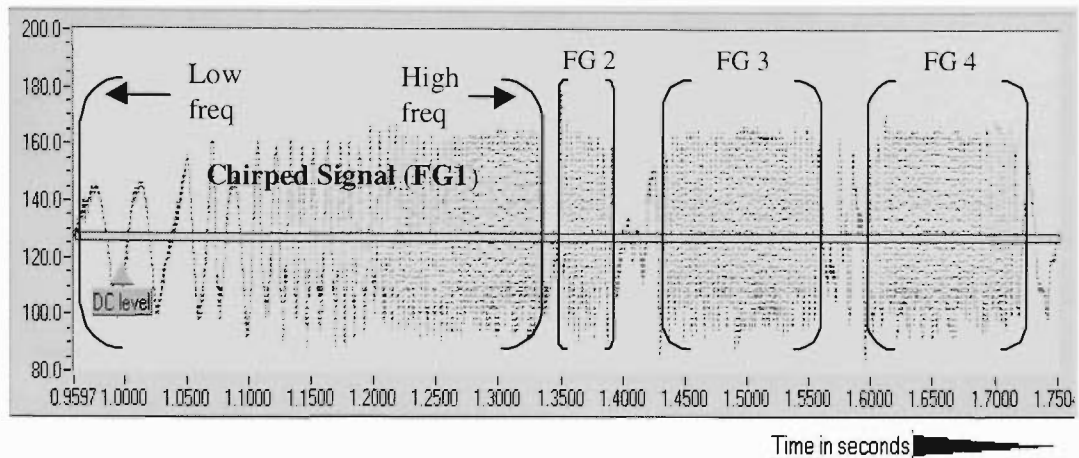


Figure 5-18: A part of the 1-2-3 truck signal from Figure 5-7(a) showing fringe-frequency variations.

Figure 5-19 shows the single-valued instantaneous fringe-frequency calculated from the fringe data as a function of fringe indices (time) of a typical truck with a 1-2-3 axle configuration. A total of six frequency peaks associated with the three axle groups are visible from Figure 5-19. The significant frequency variations are visible in the fringe index range of 30000 to 40000 arising from the multi-axle groups.

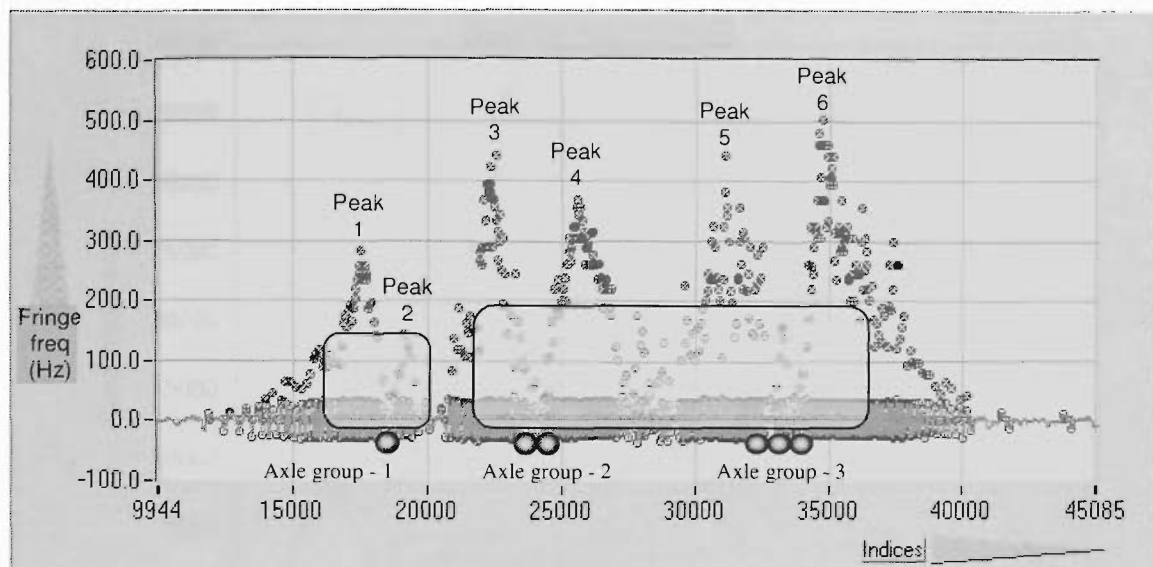


Figure 5-19: FFPI Fringe frequency profile and normalised fringe amplitude data showing fringe groups resulting from various axle/axle groups of a typical truck with axle configuration 1-2-3.

5.6.2 Method for Estimating a Single-Axle Pavement Deformation Function

As discussed in Section 3.7.5, fringe frequency information can be integrated to estimate a typical pavement deformation profile produced by a 1-2-3 configuration (Figure 5-20). In some cases, there were some extra fringes due to pavement oscillations after the departure of the truck that results in random phase errors and gives a negative cumulative area.

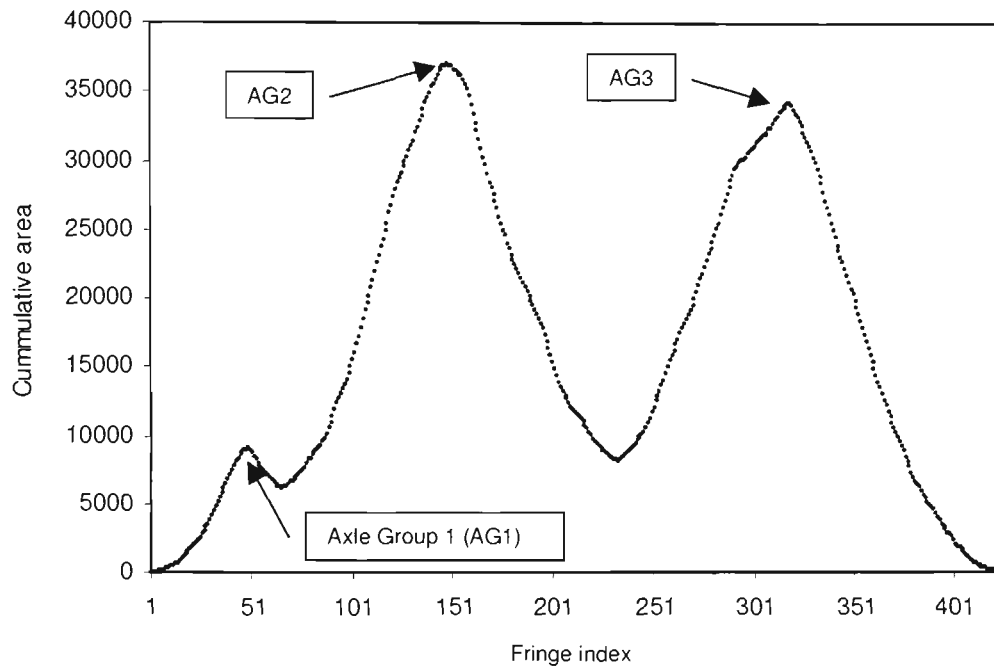


Figure 5-20: Typical cumulative area plot for 1-2-3 axle configuration obtained by processing fringe frequency plots.

The cumulative area plots were calculated from the trucks with 1-2-3 axle configurations. These plots represent pavement deformation as a function of the number of fringes. The cumulative area (Y-axis) can be calibrated by knowing the weight of each axle. Each cumulative area plot consists of a total of 6 axles with each axle governed by a weight function proportional to the fringe counts. The first axle was initially chosen for determining the axle deformation function¹⁵⁹. Previous investigation of a fibre optic weight-in-motion sensor based on polarimetric fringes¹⁴⁴ suggested a peak function profile for a single axle passing over the sensing region. Therefore, assuming a linear pavement response, the first axle data was curve-fitted for a variety of symmetric peak functions listed in Table 5-6. The peak-fitted first axle of a typical 1-2-3 truck is shown in Figure 5-21 (details are provided in Section 5.6.3).

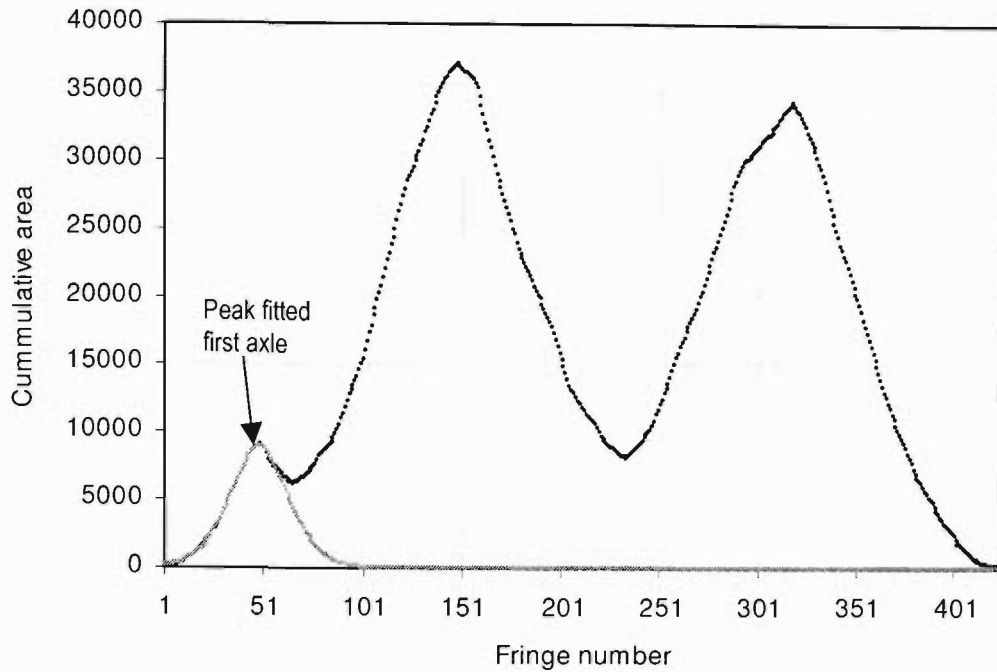


Figure 5-21: First axle curve fitted data of a typical 1-2-3 axle configuration.

5.6.3 Estimation of the Type of Single-Axle Pavement Deformation Function

The first axle curve-fitting results for 12 trucks, each with 1-2-3 axle configuration, were obtained by using the method discussed in the Section 5.6.2. It was observed that the first four functions were identical for each truck signature with variable ranking based on R^2 factor. Therefore, the first four functions were considered as the possible single-axle-function. Table 5-6 gives the correlation factor, name and the response equation of the possible single-axle-functions.

Table 5-6 : Possible single-axle pavement deformation functions.

R^2	Function name	Equation
0.999	The Lorentzian	$y=a + b/(1+((x-c)/d)^2)$
0.997	The Gaussian	$y=a + b*\exp(-0.5((x-c)/d)^2)$
0.995	The GaussMod	$y=a + b*\exp(-0.5(x-cl /d)^e)$
0.999	The Logistic	$y=a + 4bn/(1+n)^2, n=\exp(-(x-c)/d)$

The characteristics of the single-axle pavement deformation function depend on the response of the pavement structure to the vehicular loads. However for further analysis Lorentzian peak function was chosen as it provided the best fit to the experimental data.

5.7 Estimation of Fringe Count Errors based on Axle Separations and Loading Trends

This investigation has revealed the viability of a single-transducer FFPI sensor for generic structural strain or deformation sensing and WIM applications. The sensor also has potential for estimating properties of the pavement material. A variety of factors affect single-transducer WIM systems (Section 2.5.4), and in this section, an attempt has been made to modify the total number of fringes by considering the interdependent effects of the individual axle/axle-group on the FFPI responses. Section 5.7.1 discusses the typical 1-2-3 configuration and explains the observed trends of individual axle/axle-group fringe counts as a function of the weights registered by CULWAY. Sections 5.7.2 and 5.7.3 explain the possible method for estimating the modified total fringe counts by studying the distinctive features of fringe patterns.

5.7.1 Load Distribution of 1-2-3 Axle Configuration

The most common and standard axle configuration (1-2-3) was initially chosen for the analysis. This axle configuration (Figure 5-22) consists of a total of six axles (Ax_1, Ax_2, \dots, Ax_6) combined as three axle groups. Let AG_1, AG_2, AG_3 and FG_1, FG_2, FG_3 be the corresponding axle-group weights and fringe-counts as recorded by the CULWAY and FFPI systems respectively. In the 1-2-3 configuration, the first axle group consists of one axle; the second group has two axles and the third axle group consist of three axles together. The distances between the individual axles and the axle-groups are represented using letters δ and d respectively (Figure 5-22).

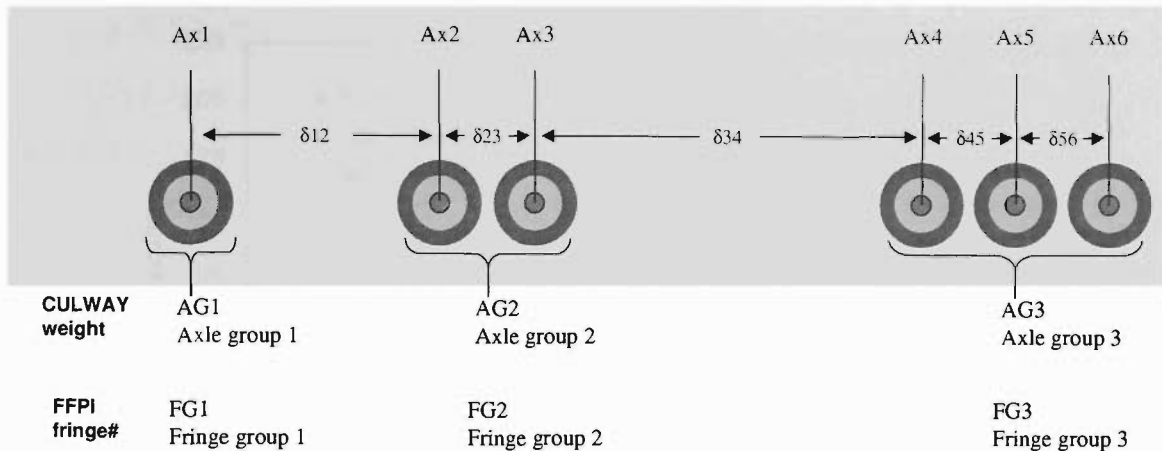


Figure 5-22: A schematic of an axle configuration for 1-2-3 axle configuration.

The gross weight of a vehicle is distributed among the total number of axles and the contribution of each axle towards sharing the gross weight depends mainly on the weight distribution and the distances between axles. Figure 5-22 shows six axles, configured in such a way that axle group AG1, AG2 and AG3 consists of one, two and three axles respectively. Distances between successive individual axles can be given as δ_{12} , δ_{23} , δ_{34} , δ_{45} and δ_{56} . The weight of the first axle in most of the conventional axle configurations such as 1-1, 1-2 and 1-2-3 is constant. Also in an axle-group, the distances between the individual axles do not vary from vehicle to vehicle. Each axle in an axle-group is placed approximately a metre apart (distances δ_{23} , δ_{45} and δ_{56}); very close to the adjacent axles as compared to the distances (δ_{12} and δ_{23}) between the consecutive axle-groups. Assuming a uniform load distribution, each axle in an axle-group should share the weight of that axle-group equally. As the number of axles increases, the contribution of each axle to the gross weight decreases. The variations in the fringe counts associated with the individual axle-groups for selected 1-2-3 trucks and their correlation with the corresponding axle-group-weights as recorded by CULWAY are plotted in Figure 5-23. It is clear from the graph that as the gross weight of the truck increases, the weight of the first axle is similar for most trucks of their own class and the actual load is shared between the axle-groups 2 and 3. It also appears that the FFPI overestimates the axle group 3 loading and underestimates the axle group 2 as discussed below.

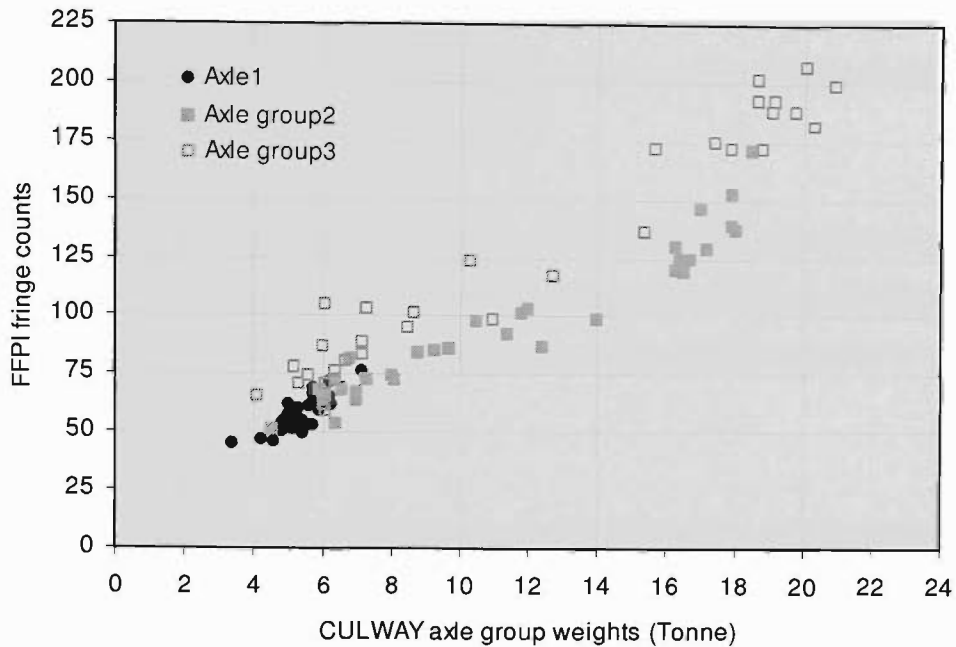


Figure 5-23: Individual FFPI fringe counts as a function of corresponding CULWAY axle weights for 1-2-3 axle configurations.

Figure 5-24 and Figure 5-25 shows the individual axle group contributions to the gross truck weight for the CULWAY and FFPI sensors respectively. For both sensors the first-axle weights do not vary significantly with increasing gross vehicular weight. However, a significant change in the relative loading of the second and third axle groups is observed with increasing gross vehicular weight. The scatter in fringe count is expected for any single-transducer WIM system. However, it is interesting to note the nonlinear trend of the total fringe counts as a function of individual CULWAY axle/axle-group weights. The CULWAY system (Figure 5-24) shows the linear response of individual axle/axle-group weights as a function of gross weight and similar trend is expected in the case of FFPI response. However, Figure 5-25 shows that as the gross vehicular weight increases, the fringe counts associated with the first axle and second axle-group have been affected. The rough trend is to underestimate axle group 2 and overestimate axle group 3, as evident in Figure 5-23.

It appears therefore that the distortion is simultaneously due to (a) the weight of the second and third axle group and (b) the distance between the three axle groups. The effect of axle separation and axle weights on the total fringe counts is discussed in

Section 5.7.3. The estimation of the error in the total fringe counts due to the variations in loading frequency has already been discussed in Section 5.4.1 and is comparable with the data.

These data recorded during this investigation demonstrate the interrelated effect of neighboring axle/axle-groups and distances and as mentioned earlier, the desirability of a more sophisticated model for processing the fringe counts to achieve a better correlation with the CULWAY records.

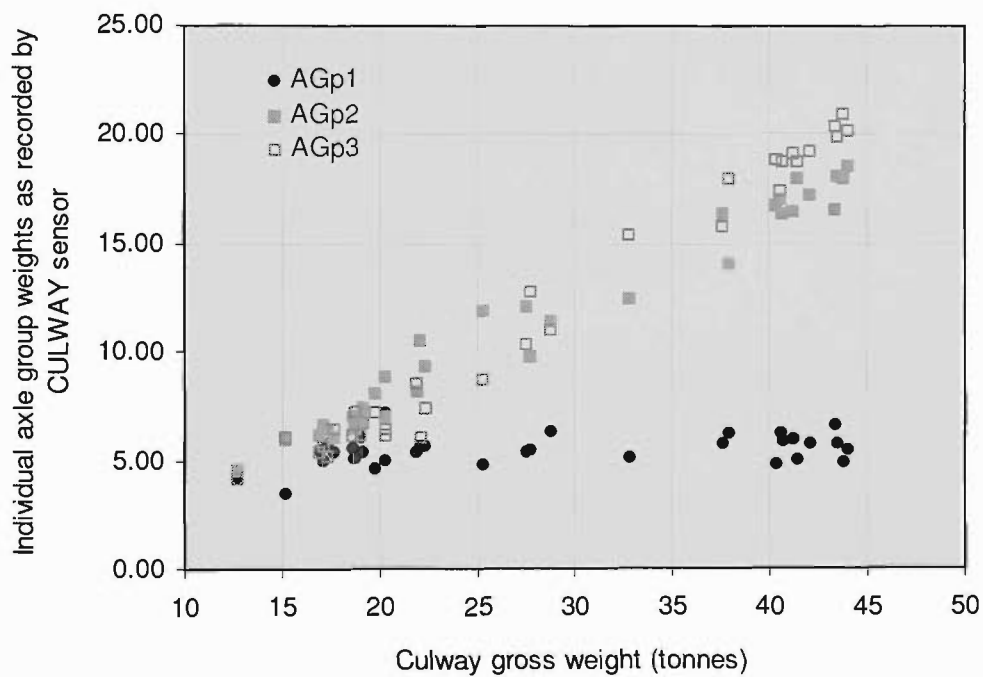


Figure 5-24: CULWAY data showing weight of an individual axle-group as a function of the gross weights.

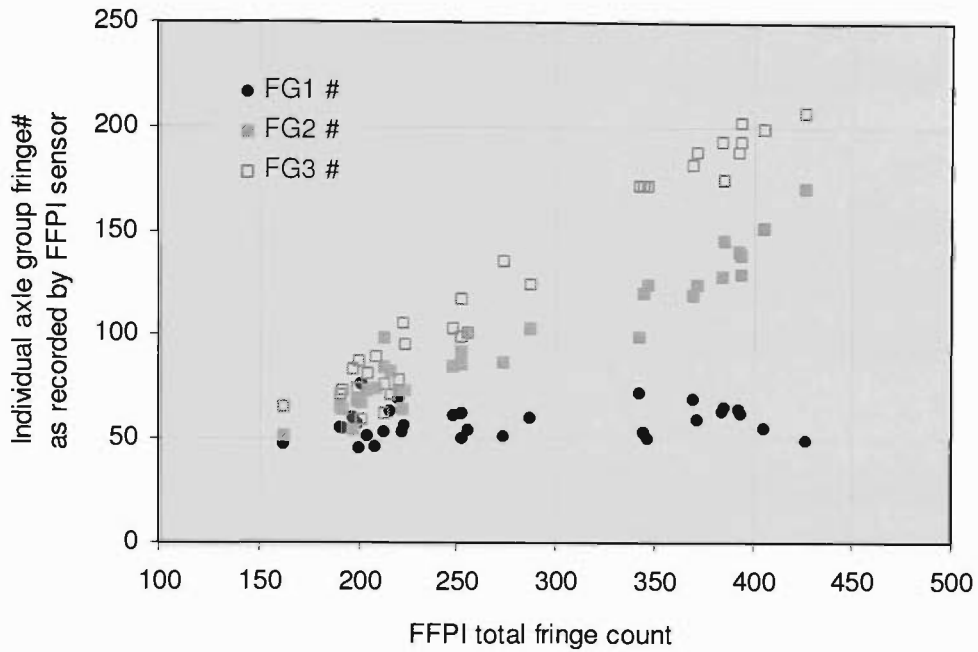


Figure 5-25: FFPI fringe count data showing the individual axle fringe counts as a function of the total fringe counts.

5.7.2 Matrix Method for Compensating Axle-Group Dependent Calibration Factor

As mentioned in Section 5.7.1, the interdependent effects of the various axle-groups for a given truck affect the individual axle-group fringe counts, and consequently the gross fringe counts. By neglecting the effect of the first axle on the third axle group and vice-versa, these interactions can be formulated for a 1-2-3 configuration as a matrix that can be defined as follows:

$$\begin{bmatrix} FG1 \\ FG2 \\ FG3 \end{bmatrix} = \begin{bmatrix} \alpha_{11} & \beta_{12} & 0 \\ \beta_{21} & \alpha_{22} & \beta_{23} \\ 0 & \beta_{32} & \alpha_{33} \end{bmatrix} \begin{bmatrix} AG1 \\ AG2 \\ AG3 \end{bmatrix} = [a] \times \begin{bmatrix} AG1 \\ AG2 \\ AG3 \end{bmatrix} \quad (5.1)$$

where

AG = Axle group weights recorded by CULWAY

FG = Corresponding fringe group counts obtained from the FFPI.

α_{11} , α_{22} , α_{33} are calibration terms (fringes/tonne) for the first, second and the third axle groups respectively, and β_{12} , β_{21} , β_{23} and β_{32} are interdependency factors quantifying the calibration terms.

Moreover, $[a]$ can be treated as a calibration matrix for a 1-2-3 axle configuration. A total of 25 trucks with 1-2-3 axle configuration were studied from the measurements. For these trucks, the spacing between axle-group 1 and 2 is ~ 4 to 5 m and between axle-group 2 and 3 is ~ 7 to 8 m.

$[a]$ was solved for the unknowns α_1 , α_2 , α_3 , β_{12} , β_{21} , β_{23} and β_{32} with MAPLE V yielding:

$$[a] = \begin{bmatrix} 10.20 & 0.79 & 0 \\ 2.94 & 8.59 & -1.38 \\ 0 & 3.97 & 6.55 \end{bmatrix} \quad (5.2)$$

Rewriting Equation (5.1) as

$$\begin{bmatrix} AG1' \\ AG2' \\ AG3' \end{bmatrix} = [a^{-1}] \times \begin{bmatrix} FG1 \\ FG2 \\ FG3 \end{bmatrix} \quad (5.3)$$

where $AG1'$, $AG2'$ and $AG3'$ are inferred CULWAY axle group weight and

$$[a^{-1}] = \begin{bmatrix} 0.095 & 0 & 0 \\ -0.026 & 0.085 & 0.038 \\ 0.029 & -0.099 & 0.161 \end{bmatrix} \quad (5.4)$$

This allows the equivalent of the CULWAY axle group weight to be calculated from the FFPI fringe counts. Using the above parameters, $AG1'$, $AG2'$ and $AG3'$ were calculated from $FG1$, $FG2$ and $FG3$ and compared with the corresponding individual axle/axle-group weights, $AG1$, $AG2$ and $AG3$, recorded by CULWAY sensor. The correlation of individual fringe groups ($FG1$, $FG2$ and $FG3$) and total fringe counts ($FG1+FG2+FG3$) with CULWAY axle/axle-group weights and gross weights respectively are tabulated in Table 5-7. The element in the second column, second row (0.77) shows the correlation factor between $FG1$ (FFPI) and $AG1$ (CULWAY) before applying the correction.

Table 5-7: Correlation summary - Comparison of raw and corrected individual axle/axle-group fringe counts with individual axle/axle-group weights recorded by CULWAY system for typical 1-2-3 axle configuration.

Correlation factor	FG1 versus AG1	FG2 versus AG2	FG3 versus AG3	Total fringe counts versus CULWAY gross
Before correction using only fringe counts	0.77	0.96	0.98	0.99
After correction using estimated weights	0.77	0.98	0.96	0.98

The correlation factor associated with estimation of the weight of second axle-group increased by 2%. However, in the case of third axle-group, the correlation factor has decreased (by 2%). This uncertainty may also depend on the number of axles in that axle group. The effect axle separation on the total fringe counts is discussed in the next section. However, results show that calculation of axle group interdependent parameters help to estimate better the individual axle weights and gross weights from the total FFPI fringe counts.

5.7.3 Fringe Count Correction

As discussed in Section 5.6.3, a Lorentzian was considered to model best the lateral subgrade deformation function induced by a single axle. This model is based on the concept (explained earlier in Section 3.7.2) of placing Lorentzian peak functions at each axle position to represent the pavement response of that axle. The amplitudes of the Lorentzians are then adjusted to fit the measured fringe frequency versus fringe indices plot. The simple fringe count scheme adopted thus far does not provide reasonable estimation with the overlapping pavement response of closely spaced axles and leads to a fringe count that underestimates the vehicle weight. By fitting Lorentzians to each axle position, the “missing” fringes associated with the overlapping of the pavement responses can be estimated.

Two Lorentzian functions with peaks separated by the axle spacing between a driving axle and the rear axle were used to model a vehicle with a 1-1 axle configuration. Figure 5-26 shows a comparison between this model and an example

of a field measurement. The two Lorentzians have peak amplitudes representing the loading of each axle. This single-axle deformation profile is similar to a typical signature that has been observed in the previous studies based on the polarimetric fibre optic weigh-in-motion sensor published in previous studies¹⁴⁴. In this particular case, axle-1 and axle-2 weigh 3.6 tonne and 5.5 tonne, respectively, with the ratio of the axle weights (1.52) determining the ratios of the amplitudes of the two Lorentzians. Also, the distance between the two axles, 6.03 m, for this vehicle, was used for the separation of the two Lorentzian peaks.

Figure 5-27 shows the frequency plot obtained using the sum of two Lorentzians from Figure 5-26 and shows a total of four frequency peaks. Ideally, each axle is characterised by two frequency peaks of the same height. As the distance between the two axle functions decreases, the overlapping of the two axle-functions affects the shape of the frequency peaks (Figure 5-27).

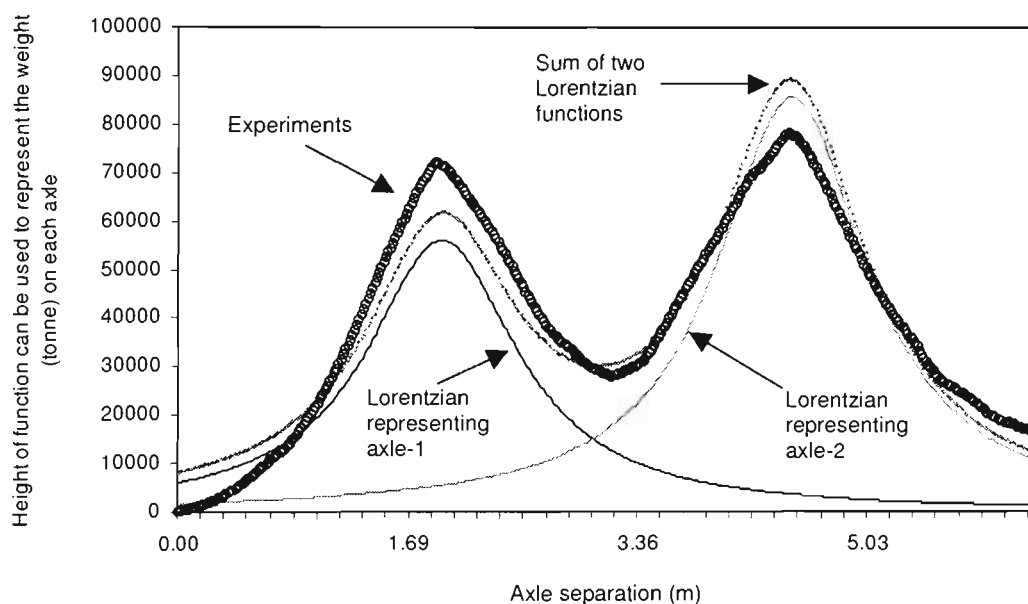


Figure 5-26: Comparison of typical 1-1 axle configuration data (Axle 1 weight = 3.6 tonnes, Axle 2 weight = 5.5 tonnes and distance between axles = 6.03 m) with mathematical model formulated by considering a Lorentzian function as a single-axle-function. The ratio of the weight of the second axle to the first axle provided the ratio of the peak amplitudes, namely 1.52 ($= 5.5 \text{ tonnes}/3.6 \text{ tonnes}$).

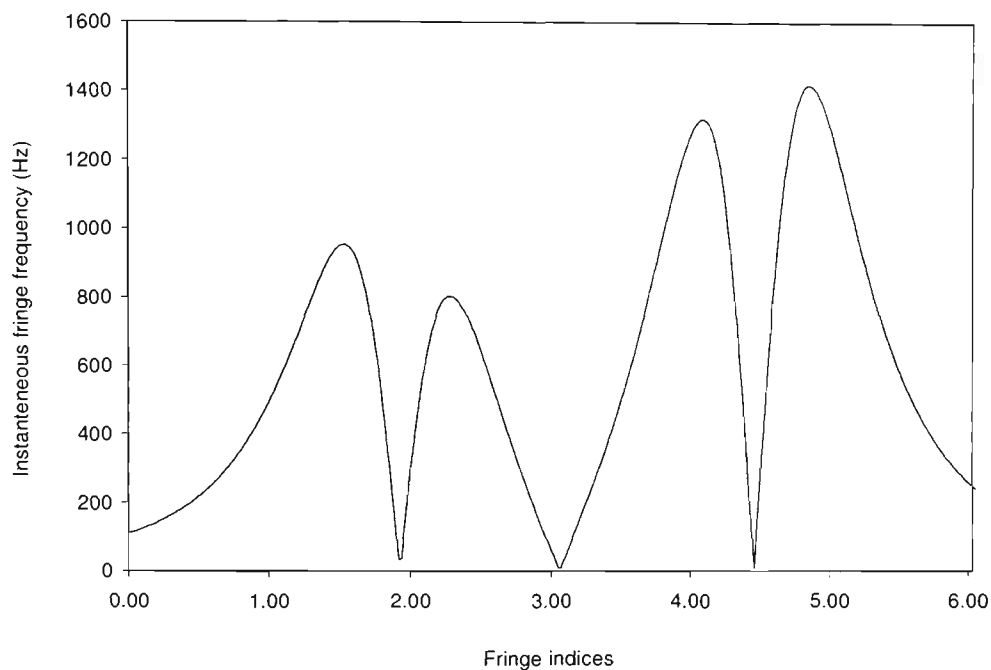


Figure 5-27: The fringe frequency plot obtained from the overlapping Lorentzian deformation functions shown in Figure 5-26. The weight of the second axle was assumed to be double the weight of the first axle for these calculations.

The total fringe counts were calculated by integrating various frequency plots obtained by varying the axle separation. Figure 5-28 shows that for 1-1 axle configuration, the maximum fringe-loss occurs at ~ 3.5 m axle separation.

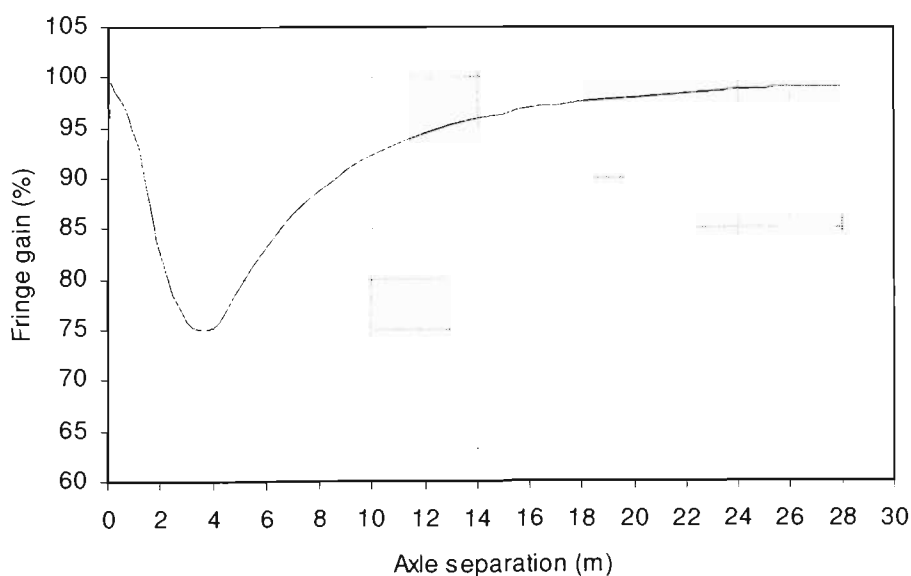


Figure 5-28: Theoretical fringe count gain calculated by using two Lorentzian axle functions. The weight of the second axle was assumed to be double the weight of the first axle for these calculations.

However, the experimental data does not show such large discrepancy in the fringe counts. This can be explained as follows:

Consider the compression and relaxation of a pavement induced by the first axle in the case of the data shown in Figure 5-29. Theoretically, the compression should be equal to the relaxation. However, the frequency peak-1 in Figure 5-29 (compression) is higher than peak-2 (relaxation) and indicates that the pavement is not completely relaxed and suggests that the time taken for relaxation is considerably longer than for compression. It is also evident in Figure 5-29, that the number of output fringes (14) obtained for relaxation (Peak 2) is less than the number (27) obtained for compression (Peak 1). Given sufficient time, the number of compression and relaxation fringes counts equalize, but in practice, for trucks traveling at speed subsequent axles arrive before the relaxation process is completed. As already discussed, this results in an underestimation of the total fringe count, and the underestimation can be obtained as follows.

The fringe loss associated with the first axle can be estimated by calculating the difference, Peak 1 - Peak 2 ($27 - 14 = 13$). This positive difference can be then added to the total fringe counts and gives the corrected fringe counts for that vehicle. Subsequently, the partially relaxed pavement from the passage of the first axle then experiences compression induced by the second axle. Therefore the relaxation signal after second axle (Peak-4) consists of relaxation from the second axle *in addition to* the remaining relaxation from the first axle. Therefore, the frequency, Peak-3, is smaller than that for Peak-4. Figure 5-29 clarifies that the frequency difference corresponding to the first axle is positive as compared with the frequency difference of the second axle. This confirms that Peak 4 of the second axle partially represents the fringe-loss from the first axle. The total frequency and fringe count correction factors can then be estimated as $[(\text{Peak 1} - \text{Peak 2}) + (\text{Peak 3} - \text{Peak 4})]$. In this particular case, (Figure 5-29), fringe-loss at the first axle is compensated by the fringe-gain produced by the frequency peaks of the second axle.

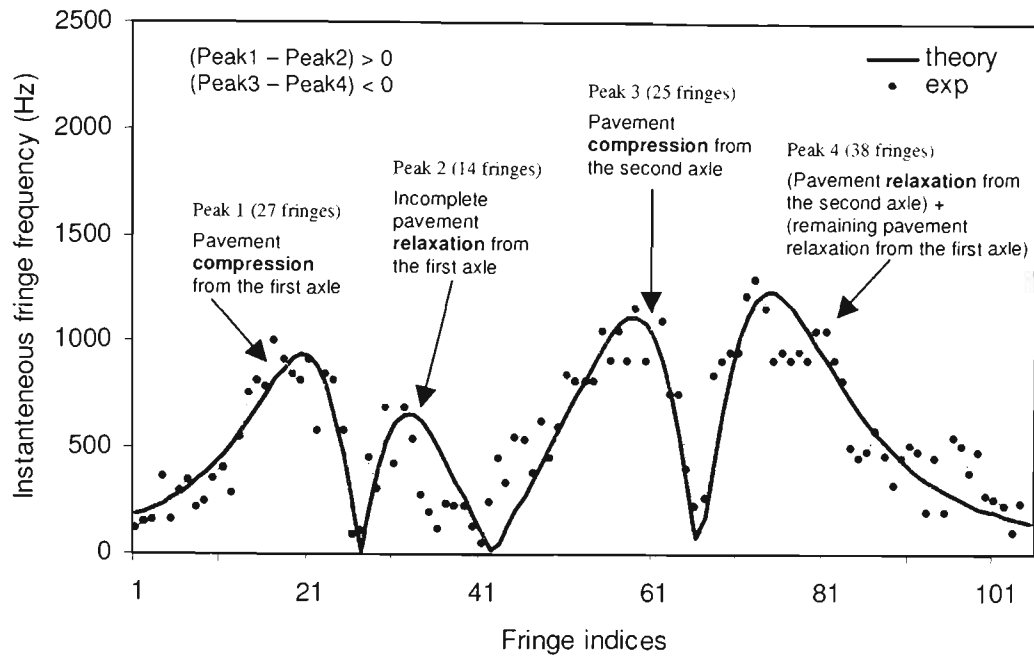


Figure 5-29: The experimental plot of an instantaneous fringe frequency for 1-1 axle configuration as fitted with a sum of two Lorentzians. The plot also shows fringe counts associated with each frequency peaks.

The calibration factor (fringes/tonne) as a function of CULWAY gross weights for various axle configurations before (Figure 5-17) and after applying the correction factor is shown in Figure 5-30. The plot of corrected calibration factor data has comparatively less scatter than the raw data and the trend approaches more towards a horizontal straight line. Also, Figure 5-31, shows that the corrected fringe counts has less scatter than the total fringe counts. The method applied to obtain the correction factor shows potential and overall result shows improved correlation (standard error improves from ± 4 fringes to ± 2 fringes) between the total (corrected) fringe counts and the CULWAY records (Figure 5-30 and Figure 5-31). This reduces the error margin range from 6 – 8% to 4 – 6%.

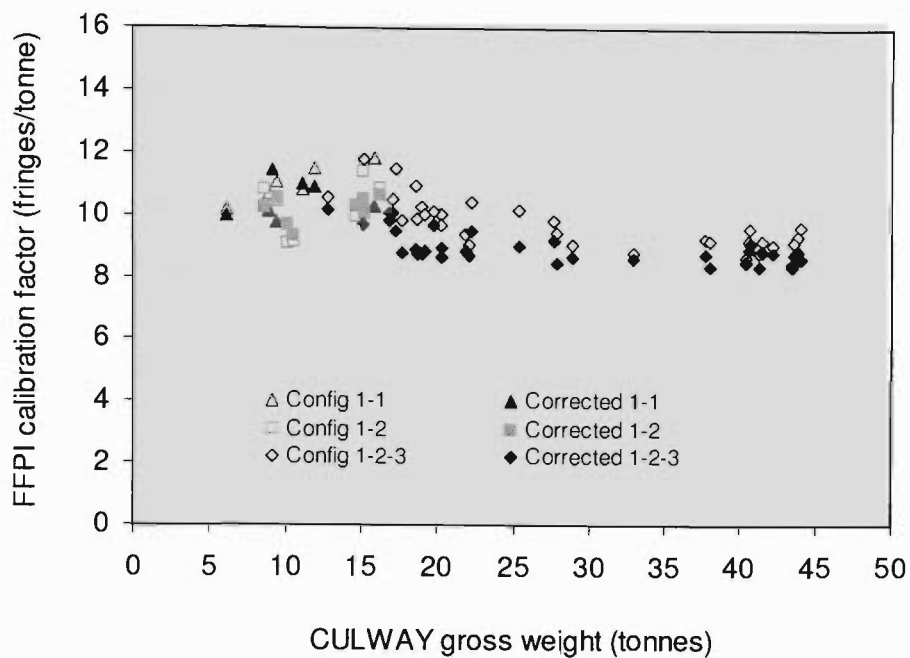


Figure 5-30: Corrected FFPI fringe counts (Figure 5-17) showing less scatter in the FFPI calibration factor.

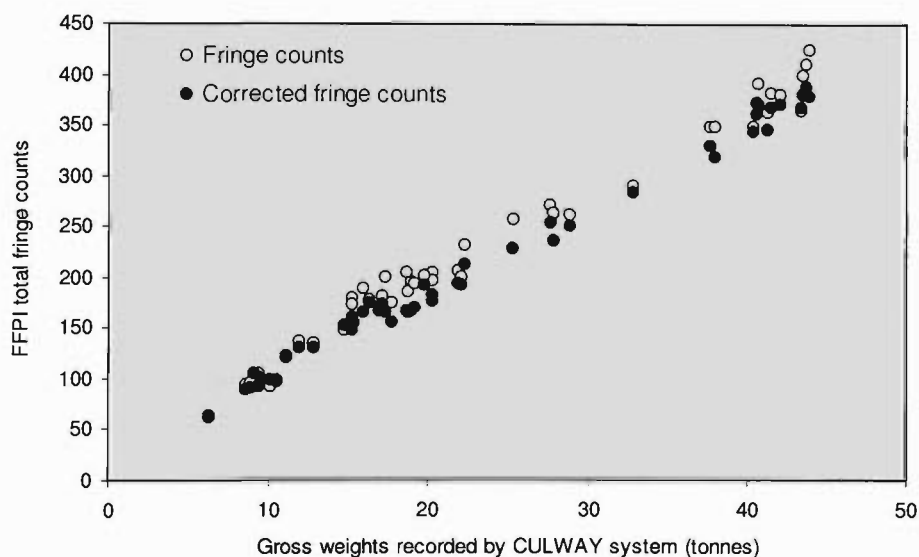


Figure 5-31: Corrections applied to the total fringe counts (from Figure 5-17) yielded better correlation with CULWAY records. Initial uncertainty of ± 4 fringes (error of 6 – 8%) was reduced to ± 3 fringes (4 – 6%).

5.8 Summary

The long gauge Fibre Fabry-Pérot Interferometric (FFPI) sensor configured to operate in the reflection mode was assessed for its viability as a single transducer weigh-in-motion system. The variations in the total number of output fringes were observed to be a linear function of the applied vehicle induced dynamic loads. This sensor is capable of estimating the vehicular gross weight within error margins of 10-15% as confirmed with the CULWAY system. This observed accuracy of the single-transducer FFPI sensor for WIM application is comparable with the results of conventional single-transducer fibre/non-fibre systems published elsewhere.

The errors in the FFPI calibration were due to the dynamic effects arising from the various axle configurations and pavement properties. Poisson's ratio of a pavement material is susceptible to the temperature and loading frequency. For a given truck configuration, variations in the loading frequency affect the total fringe counts and this effect decreases at elevated temperatures of the pavement material.

A marked improvement in performance was achieved by applying a correction to the fringe count based on a Lorentzian model of the pavement response. Forty eight vehicles were processed in accordance with that model and the error factor was reduced from 6-8% to ~ 4-6%. The calibration factor (fringes/tonne) is susceptible to variations in axle configurations and the gross weight of the truck. Trucks with a 1-1 axle configurations have a calibration factor of ~ 12 fringes/tonne. However, 1-2 and 1-2-3 configurations have calibration factors of ~ 10 fringes/tonne and ~ 9 fringes/tonne, respectively. The calibration factor increases for the vehicles with smaller gross weights and decreases for heavier vehicles. Also higher scatter was observed for the calibration factor of lightweight trucks and comparatively less scatter for heavier trucks. The scatter in lightweight trucks can be explained on the basis of random vehicular bouncing. The Lorentzian model of achieving better correlation of the total fringe counts with CULWAY records has the potential to narrow the range of uncertainty of 13 to 9 fringes/tonne. The improvements in the calibration factors for 1-1, 1-2 and 1-2-3 axle configuration is provided in Table 5-8.

The correction applied to the fringe data reduces the initial error margins of 6–8% to 4–6%.

Table 5-8: Calibration factor summary.

Vehicle configuration	Calibration factor based on the total fringe count (fringes/tonne)	Corrected calibration factor based on the total fringe count (fringes/tonne)
1-1	12	10
1-2	10	10
1-2-3	9	9

Apart from using this sensor for WIM applications, it has the potential to gather and process information which can be utilised for investigating responses of pavement materials under the action of vehicle-induced dynamic loads. A method of estimating the single-axle pavement deformation function has been described.

CHAPTER 6

CONCLUSIONS AND FUTURE DIRECTIONS

6.1. Thesis Summary

6.1.1. Introduction

The main aim of this investigation was to design, fabricate, test and calibrate a single-transducer embedded Weigh-In-Motion (WIM) sensor based on a long-gauge fibre optic Fabry-Pérot interferometer operating in the fringe counting regime. The fibre Fabry-Pérot interferometer configuration was adopted for its simplicity, sensitivity, cost effectiveness and ease of installation. Apart from WIM applications this sensor can also be implemented for monitoring real-time structural health.

During this investigation the sensors were attached to an aluminium beam and embedded in pavement structures. The applied structural strain induces a change in the length of an embedded sensing element. The FFPI sensor outputs these changes in terms of the number of optical fringes, which in turn is proportional to the applied strain.

6.1.2. Monitoring Dynamic Structural Strains

Laboratory trials were carried out by attaching 300 mm long sensing elements in grooves in an aluminium beam (length 500 × width 59 × thickness 6 mm). The sensor response was studied by subjecting the beam to various structural deformation waveforms and frequencies using a three-point bending configuration. The sensor response was linear with correlation factor of 0.99 as compared with the response of an electrical strain gauge installed on the beam surface. For various applied deformations in the range of 0 to 2 mm, the strain measured by a surface installed electrical strain gauge was in the range of ~ 0 to 208 $\mu\epsilon$ and produces FFPI fringes in the range of 0 to 36 with a calibration factor of ~ 0.17 fringe/ $\mu\epsilon$. However, as this sensor utilises a fringe counting regime, the maximum error in estimating structural strain is ± 1 fringe and limited by the fringe counting software designed for processing fringe data. This represents a resolution of ~ 6 $\mu\epsilon$ /fringe and introduces uncertainty of ~ ± 6 $\mu\epsilon$. The instrumental error associated with the electrical strain gauge is ($\pm 3\%$), and the applied deformation (± 0.01 mm) introduces an error of

1.6%. Other factors such as mechanical instabilities and input laser noise also affect the sensor output and these were allowed for. To measure the dynamic structural strains with minimum error, it is important to embed the sensing element within the structure at a reliable position and direction, which outputs maximum fringes for minute changes in the applied strain.

The results discussed in the above paragraphs were obtained by applying dynamic deformations in range of 0 to 50 Hz to the test beam. The calibration factor was observed independent of the applied deformation frequencies. Also the fringe counts observed for the compression and relaxation cycles were free of hysteresis. This sensor is capable of monitoring output fringe frequencies in the range of ~ 30 Hz to 50 kHz as imposed principally by the bandwidth of the electronic filtering circuit, which was optimised for the WIM applications.

6.1.3. Viability for WIM Sensing

The viability of the single-transducer FFPI sensor for WIM application was tested by embedding the sensing element 800 mm below a road surface. The FFPI sensor response was a linear function of the applied gross load and is capable of estimating truck weight within error margins of 10 to 15% for all type of axle configurations. This observed accuracy is a consequence of the single transducer FFPI sensor for WIM applications and is comparable with the results of other conventional single-transducer fibre/non-fibre WIM systems. Single element WIM systems will underestimate an applied load due to the slow relaxation of the pavement material as compared with the applied deformation. A method of applying fringe count correction was formulated and, based on the difference observed between the fringes, accounted for applied compression and relaxation. This method provided better correlation between the total fringe counts and measured CULWAY gross weights, reducing the initial error margins of 6–8% to 4–6%. These results can be further improved by implementing a multiple sensing element WIM system. As discussed in Section 2.5.4, commercial non-fibre WIM systems employing multiple sensing elements have reduced the range of error from ± 20 -50% to ± 5 -8%. This significant

reduction in error is due mainly to the averaging of signals acquired from various sensing elements. This is also possible in the case of this FFPI WIM system by installing various sensing elements at identical depths. The schematic of a multiple-transducer FFPI WIM configuration is shown in Figure 6-1.

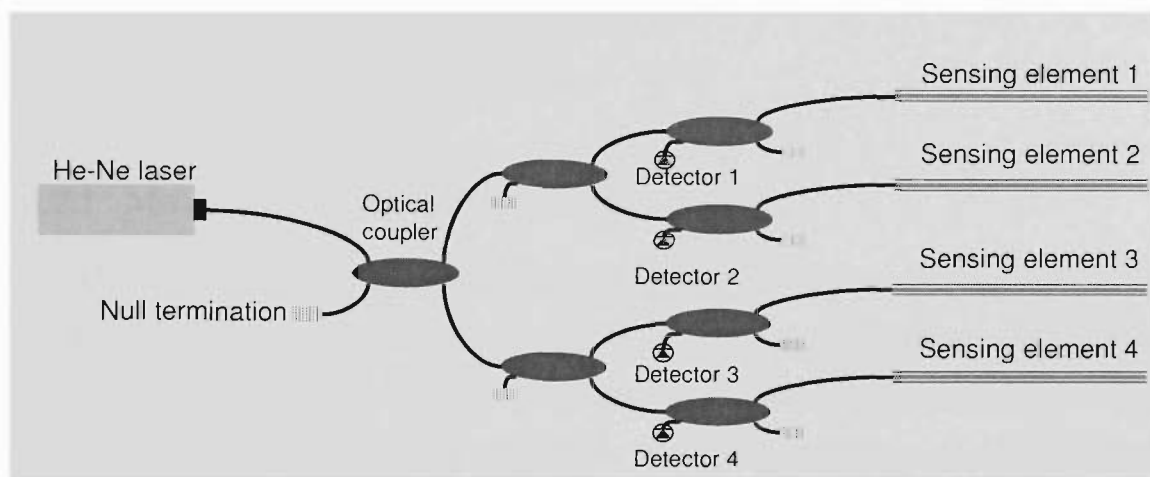


Figure 6-1: Fabry-Pérot sensor multiplexing scheme for multiple sensing elements.

6.1.4. Estimation of Pavement Deformation Profile

The recorded fringe data were processed to determine the instantaneous fringe frequencies which also enabled the estimation of the structural deformation profile. This sensor is capable of measuring the rate of structural deformation (relaxation or compression) and this provides information regarding the response of pavement materials under the action of dynamic forces.

Hence this sensor has the potential for

- (a) Studying real-time dynamic structural strain profiles
- (b) Estimating weights of vehicles moving with high speeds
- (c) Investigating material response/hysteresis or other properties such as variations in Poisson's ratio under action of dynamic forces.

To understand its full potential it is important to undertake further studies of single-transducer FFPI systems and especially multiple-transducer FFPI systems.

6.2. Future Directions

This thesis investigated a single-transducer FFPI sensor for generic structural strain sensing and WIM applications. These results will help to achieve better accuracy by (1) applying several sensors laterally to average the dynamic response of the pavement structure, and (2) applying several sensors at multiple depths within the different pavement layers.

6.2.1 Multiple Transducer FFPI WIM System

An appropriate multiplexing scheme is necessary for achieving a multiple transducer WIM system. A simple multiplexing scheme for four sensing elements is suggested (Figure 6-1) which uses a single He-Ne source. This multiplexed system was constructed during the present study, but was not investigated in detail. Once calibrated, such a sensing network could either be used for monitoring deformations in various places simultaneously, or for averaging the random structural vibrations within a single pavement structure. Moreover, this sensing scheme is important for the comparative investigation of deformations induced by the same force in various structural layers.

REFERENCES

1. Kokudo, K., (2001) "Increasing efficiency in road management," *UC Berkeley Transportation Library - PATH Database Record Number 23865*, Japan. (Web source: <http://www.its.go.jp/ITS/index/indexRoadM.html>).
2. Andrle, S., Kroeger, D., Gieseman, D., and Burdine, N., (2002) "Highway Maintenance Concept Vehicle, Phase IV," *Center for Transportation Research and Education (CTRE), Iowa State University, Ames, IA*. (Web source: <http://www.ctre.iastate.edu/reports/concept4.pdf>).
3. Maze, T., Shrock, S., VanDerHorst, K., (1999) "Traffic Management Strategies for Merge Areas in Rural Interstate Work Zones," *Center for Transportation Research and Education (CTRE), Iowa State University, Ames, IA*. (Web source: <http://www.ctre.iastate.edu/reports/traffic6.pdf>).
4. Weigh-In-Motion Conferences. Center for Transportation Research and Education (CTRE), Iowa State University, Ames, IA 50010-8632. Year 1998 in Lisbon, Portugal, Year 2002 in Orlando FL USA. (Web source: <http://www.icwim.org/>).
5. Laboratoire Central des Ponts et Chaussées (LCPC), (2000) "Weigh-in-motion of road vehicles for Europe (WAVE)," Report of work package 4, Optical WIM systems technology for the future, RDT project, RO-96-SC, 403, Paris, France. (Web source: <http://www.zag.si/wim/>).
6. Burtwell, M., Oberg, G., (2002) "COST action 344: improvements to snow and ice control on European roads and bridges," *New Challenges for Winter Road Service, XIth International Winter Road Congress, Sapporo, Japan, World Road Association - PIARC La Grande Arche, Paroi Nord, Niveau 8, F-92055 La Defense Cedex, France*.

7. Lee, C. E., and Souny-Slitine, N., (1998) "Final research findings on traffic-load forecasting using weigh-in-motion data," *Center for Transportation Research, Bureau of Engineering Research, The University of Texas, Research report no. 987-7*. Austin, TX. (Web source: http://www.utexas.edu/research/ctr/pdf_reports/987_7.pdf).
8. Lee, C. E., and Garner, J. E., (1996) "Collection and analysis of augmented weigh-in-motion data," *Center for Transportation Research, Bureau of Engineering Research, The University of Texas, Research report no. 987-8*. Austin, TX. (Web source: http://www.utexas.edu/depts/ctr/pdf_reports/987-8.pdf).
9. Cole, D. J., Cebon, D., (1996) "Truck Tires, Suspension Design and Road Damage," *International Rubber Conference (IRC'96)*, June, pp.17-21, Manchester, UK.
10. Chan, T. H. T., Law, S. S., Yung, T. H., and Yuan, X. R., (1999) "An interpretative method for moving force identification," *J Sound and Vibration* **219** 503-524.
11. Dunlop, R. J., (1999) "Managing performance of a highway system in the 21st century," *Transit NZ* (Web source: http://www.transit.govt.nz/news/content_files/ConferencePaper4_PDFFile.PDF).
12. Hajek, J. J., Kennepohl, G., and Billing, J. R., (1992) "Application of Weigh-In-Motion data in transportation and planning," *Transportation and Research Board*, Transport research record no 1364, pp.169-178, Washington, DC.
13. Huff, A., (2002) "Weighing bypass : electronic clearance at weigh stations carries significant benefits in time, safety and convenience," *Commercial Carrier Journal For Professional Fleet Managers* **159** 38-40.
14. Chou, C., and Tsai, H., (1999) "Study of applying the high speed weigh-in-motion to law enforcement," *National Research Council (U.S.), 78th Transportation Research Board Meeting*, p.17, Washington, DC.
15. Grattan, K. T. V., and Sun, T., (2000) "Fibre optic sensor technology: an overview," *Sensors and Actuators* **82** 40-61.

16. Téral, S. R., (1998) "Fibre optic weigh-in-motion: looking back and ahead," *Proc SPIE* **3326** 129-137.
17. Kosmowski, B. B., Mazikowski, A., and Wierzba, P., (1999) "Polarimetric optical fibre sensor for Weigh-In-Motion applications," *Proc SPIE* **3730** 22-26.
18. French patent no. 88 02 765 (4 April 1988), *Institute National de la Propriete Industrielle*, Paris, France.
19. de Vries, M., Arya, V., Grinder, C., Murphy, K., and Claus, R., (1994) "Civil infrastructure monitoring for IVHS using optical fibre sensors," *Proc SPIE* **2344** 297-302.
20. Inaudi, D., (2000) "Application of civil structural monitoring in Europe using fibre optic sensors," *Prog Struct Engng Mater* **2** 351-358.
21. Lee, W., Lee, J., Henderson, C., Taylor, H. F., James, R., Lee, C. E., Swenson, V., Atkins, A., and Gemeiner, W.G., (1999) "Railroad bridge instrumentation with fiber-optic sensors," *Appl Opt* **38** 1110-1114.
22. Vohra, S. T., Todd, M. D., Johnson, G. A., Chang, C. C., and Danver, B. A., (1999) "Fibre Bragg grating sensor system for civil structure monitoring: Applications and field tests," *Proc SPIE* **3746** 32-37.
23. Udd, E., (1988) Editor, *Fibre Optic Smart Structures and Skins I*, *Proc SPIE* **986**.
24. Udd, E., (1989) Editor, *Fibre Optic Smart Structures and Skins II*, *Proc SPIE* **1170**.
25. Udd, E., and Claus, R. O., (1990) Editors, *Fibre Optic Smart Structures and Skins III*, *Proc SPIE* **1370**.
26. Claus, R. O., and Udd, E., (1991) Editors, *Fibre Optic Smart Structures and Skins IV*, *Proc SPIE* **1588**.
27. Potter, T. E. C., Cebon, D., and Cole, D. J., (1997) "Assessing 'road friendliness': a review," *J Automobile Engineering* **211** 455-475.

28. Buckmaster, R. I., (1995) "The HSEMU and multi-lane CULWAY weigh-in-motion systems," Proc International Conference on Application of New Technology to Transport Systems, 1 341-358, ITS Australia, Melbourne, VIC, Australia. (Web source: <http://www.arrb.org.au/products/culway.htm>).
29. Kenna, A., (1999) "Sensor Market goes global," *Sensor Overview*, June, pp.40-43. (Web source: <http://www.isa.org/isaolp/journals/pdf/intech/990640.pdf>).
30. Fernando, G. F., Webb, D. J., and Ferdinand, P., (2002) "Optical-fiber sensors," *Materials Research Society (MRS) Bulletin* **27** 359-364. (Web source: www.mrs.org/publications/bulletin).
31. Smith, J. A., (2000) "Using telecommunication technology to develop an optical sensing infrastructure," *Proc AIP Conference* no. 509-B, 2123-2130.
32. Rao, Y. J., (1999) "Recent progress in applications of in-fibre Bragg grating sensors," *Optics & Lasers in Engineering* **31** 297-324.
33. Bergh, R. A., Kotler, G., and Shaw, H. J., (1980) "Single mode fibre optics directional coupler," *Electron Lett* **16** 260-261.
34. Dakin, J., and Culshaw, B., (1997) Editors, *Optical Fibre Sensors: Principles and Components*, Vol. 1 and 2, Artech House Inc., Norwood, MA.
35. Wade, S. A., Collins, S. F., and Baxter, G. W., (2003) "The fluorescence intensity ratio technique for optical fibre point temperature sensing," *J Appl Phys* **94** (October).
36. Ohishi, Y., and Takahashi, S., (1986) "Optical temperature sensor using Eu⁺-doped fluoride glass," *Appl Opt* **25** 720-723.
37. Muhs, J. D., Smith, D. B., and Allison, S. W., (1991) "Overview of silicon-rubber fibre-optic sensors and their applications," *Proc SPIE* **1586** 107-115.
38. Day, G. W., Deeter, M. N., and Rose, A. H., (1992) "Faraday effect sensors: a review of recent progress," *Proc SPIE* **PM07** 11-26.

39. Grattan, K. T. V., and Meggitt, B. T., (1998) "Optical Fiber Sensor Technology" Volumes 1-4 (Chapman & Hall, London & Kluwer Academic, Dordrecht Netherlands).
40. Katzir, A., (1990) Editor, "Proceedings of optical fibers in medicine: progress in biomedical optics," *Proc SPIE* **1201**.
41. Wolfbeis, O. S., (1989) "Novel techniques and materials for fibre optic chemical sensing," *Springer Proc Phys - Optical Fibre Sensors*, **44** 416-424.
42. Dakin, J. P., (1989) "Optical fiber environmental sensors," *Springer Proc Phys - Optical Fibre Sensors* **44** 186-193.
43. Lequime, M., Lecot, C., Jouve, P., and Pouleau, J., (1991) "Fibre optic pressure and temperature sensor for down-hole applications," *Proc SPIE* **1511** 244-249.
44. Bergh, R. A., Lefevre, H. C., and Shaw, H. J., (1984) "An overview of fiber-optic gyroscopes," *J Lightwave Tech* **LT-2** 91-107.
45. Kyuma, K., Tai, S., Nunoshita, M., Mikami, N., and Ida, Y., (1983) "Fibre optic current and voltage sensors using a Bi₁₂GeO₂₀ single crystal," *J Lightwave Tech* **LT-1** 93-97.
46. Udd, E., (1989) "Fibre sensors for smart structures," *Springer Proc Phys - Optical Fibre Sensors* **44** 329-399.
47. Culshaw, B., Gardiner, P.T., and McDonach, A., (1992) Editors, *First European Conference on Smart Structures and Smart Materials, Proc SPIE* **1777**.
48. Green, A. K., Zaidman, M., Shafir, E., Tur, M., and Gali, S., (2000) "Infrastructure development for incorporating fibre-optic sensors in composite materials," *Smart Mater Struct* **9** 316-321.
49. Kalamkarov, A. L., Fitzgerald, S. B., MacDonald, D. O., and Georgiades, A. V., (2000) "The mechanical performance of pultruded composite rods with embedded fiber-optic sensors," *Composites Science & Technology* **60** 1161-1169.
50. Uttamchandani, D., (1994) "Fibre optic sensors and smart structures: developments and prospects," *Electronics and Communication Engineering Journal*, October, 237-246.

51. Holst, A., and Lessing, R., (1992) "Fibre optic intensity modulated sensors for continuous observation of concrete and rock-filled dams," *Proc SPIE* **1777** 223-227.
52. Udd, E., Michal, R. J., Higley, S. E., Theriault, J. P., LeCong, P., Jolin, D. A., and Markus, A. M., (1987) "Fibre optic sensor systems for aerospace applications," *Proc SPIE* **838** 162-168.
53. Dakin, J. P., (1983) "Optical fibre sensors - principles and applications," *Proc SPIE* **374** 172-182.
54. Ning, Y. N., Grattan, K. T. V., Wang, W. M., and Palmer, A. W., (1991) "A systematic classification and identification of optical fibre sensors," *Sensors and Actuators* **29** (A) 21-36.
55. Kao, T. W., and Taylor, H. F., (1996) "High-sensitivity intrinsic fiber-optic Fabry-Perot pressure sensor," *Opt Lett* **21** 615-617.
56. Kist, R., (1989) "Point sensor multiplexing principles," *Optical Fibre Sensors: Systems and Applications*, Vol. 2, pp.511-574, Editors, Dakin, J., and Culshaw, B., Artech House Inc., Norwood, MA.
57. Barnoski, M. K., and Jensen, S. M., (1976) "Fibre waveguides: a novel technique for investigating attenuation characteristics," *Appl Opt* **15** 2112-2115.
58. Fields, J. N., Asawa, C. K., Ramer, O. G., and Barnoski, M. K., (1980) "Fibre optic pressure sensor," *J Acoust Soc Am* **67** 816-818.
59. Born, M., and Wolf, E., (1999) "Principles of Optics: Electromagnetic theory of propagation, interference and diffraction of light," 7th Edition, Pergamon Press, London.
60. Hecht, E., (2001) "Optics," 4th Edition, Addison-Wesley Publishing, Boston, MA.
61. Culshaw, B., and Giles, I. P., (1983) "Fibre optic gyroscopes," *J Phys E: Scientific Instruments* **16** 5-15.
62. Kanada, T., and Nawata, K., (1979) "Injection laser characteristics due to reflected optical power," *IEEE J Quantum Electron* **QE-15** 559-565.

63. Stowe, D. W., Moore, D. R., and Priest, R. G., (1982) "Polarisation fading in fiber interferometric sensors," *J Quantum Electron* **QE-18B** 1644-1647.
64. Jackson, D. A., Preist, R., Dandridge, A., and Tveten, A. A., (1980) "Elimination of drift in a single mode optical fiber interferometer using piezoelectrically stretched coiled fiber," *Appl Opt* **19** 2926-2929.
65. Dandridge, A., Tveten, A. B., and Giallorenzi, T. G., (1982) "Homodyne demodulation scheme for fibre optic sensors using phase generated carrier," *IEEE J Quantum Electron* **QE-18** 1647-1651.
66. Sheem, S. K., Giallorenzi, T. G., and Koo, K. P., (1982) "Optical techniques to solve the fading problem in fibre interferometers," *Appl Opt* **21** 689-695.
67. Tatam, R. P., (1995) "Optical fibre modulation techniques for single mode fibre sensors," *Optical Fibre Sensor Technology*, vol.2 pp.239-241, Editors, K. T. V. Grattan and B. T. Meggitt, Chapman & Hall, London.
68. Cole, J. H., Danver, B. A., and Bucaro, J. A., (1982) "Synthetic heterodyne interferometric demodulation," *IEEE J Quantum Electron* **QE-18** 694-697.
69. Jackson, D. A., Kersey, A. D., Corke, M., and Jones, J. D. C., (1982) "Pseudo-heterodyne detection scheme for optical interferometers," *Electron Lett* **18** 1081-1083.
70. Kersey, A. D., Corke, M., and Jackson, D. A., (1984) "Linearised polarimetric optical sensor using a 'heterodyne-type' signal recovery scheme," *Electron Lett* **20** 209-211.
71. Moss, G. E., Miller, L. R., and Forward, R. L., (1971) "Photon-noise limited laser transducer for gravitational antenna," *Appl Opt* **10** 2495-2498.
72. Jackson, D. A., Dandridge, A. and Sheem, S. K., (1980) "Measurements of small phase shifts using single-mode optical fibre interferometer," *Opt Lett* **5** 139-141.
73. Petuchowski, S. J., Giallorenzi, T. G., and Sheem, S. K., (1981) "A sensitive fiber optic Fabry-Perot interferometer," *IEEE J Quantum Electron* **QE-17** 2168-2170.

74. Yoshino, T., Kurosawa, K., Itoh, K., and Ose, T., (1982) "Fiber optic Fabry Perot interferometer and its sensor applications," *IEEE J Quantum Electron* **QE-18** 1624-1633.
75. Valis, T., Hogg, D., and Measures, R. M., (1990) "Fiber optic Fabry-Perot strain gauge," *IEEE Photon Technol Lett* **2** 227-228.
76. Lee, C. E., Atkins, R. A., and Taylor, H. F., (1987) "Reflectively tapped optical fibre transversal filters," *Electron Lett* **23** 596-598.
77. Lee, C. E., and Taylor, H. F., (1988) "Interferometric optical fibre sensors using internal mirrors," *Electron Lett* **24** 193-194.
78. Morey, W. W., Melz, G., and Glen, W. H., (1989) "Fibre optic Bragg grating sensors," *Proc SPIE* **1169** 98-107.
79. Lee, C. E., Gibler, W. N., Atkins, R. A., and Taylor, H. F., (1992) "In line Fibre Fabry Perot interferometer with high reflectance internal mirrors," *IEEE J Lightwave Technol* **LT-10** 1376.
80. Lee, C. E., and Taylor, H. F., (1995) "Sensors for smart structures based on the Fabry-Perot interferometer," *Fibre Optic Smart Structures*, pp.249-269, Editor, Eric Udd, John Wiley & Sons IN.
81. Leilabady, P. A., and Corke, M., (1988) "All-fibre-optic remote sensing of temperature employing interferometric techniques," *Opt Lett* **12** 772-774.
82. Murphy, K. A., Gunther, M. F., Vengsarkar, A. M., and Claus, R. O., (1992) "Fabry-Perot fibre-optic sensors in full-scale fatigue testing on an F-15 aircraft," *Appl Opt* **31** 431-433.
83. Mitchell, G. L., (1988) "A review of Fabry-Perot interferometric sensors," *Springer Proc - Phys Optical Fibre Sensors* **44** 450-457.
84. Murphy, K. A., Kobb, C. E., Plante, A. J., Desu, S., and Claus, R. O., (1991) "High temperature applications of silica and sapphire optical fibres," *Proc SPIE* **1370** 169-172.

85. Sirkis, J., Berkoff, T. A., Jones, R. T., Singh, H., Kersey, A. D., Friebele, E. J., and Putnam, M. A., (1995) "In-line fiber etalon (ILFE) fiber-optic strain sensors," *J Lightwave Technol* **LT-13** 1256-1263.
86. Lee, C. E., Atkins, R. A., and Taylor, H. F., (1988) "Performance of the fibre optic temperature sensor from 200 to 1050°C," *Opt Lett* **13** 1038-1043.
87. Ja, Y. H., (1995) "Optical Vernier Filter with Fiber Grating Fabry-Perot Resonators," *Appl Opt* **34** 6164-6167.
88. Ribeiro, A. B. L., Rao, Y. J., Zhang, L., Bennion, I., and Jackson, D. A., (1996) "Time-and-spatial-multiplexing tree topology for fiber-optic Bragg-grating sensors with interferometric wavelength-shift detection," *Appl Opt* **35** 2267-2273.
89. Hill, K. O., Fujii, Y., Johnson, D. C., and Kawasaki, B. S., (1978) "Photo-sensitivity in optical fibre waveguides: application to reflection filter fabrication," *Appl Phys Lett* **32** 647-649.
90. Kawasaki, B. S., Hill, K. O., Johnson, D. C., and Fujii, Y., (1978) "Narrow-band Bragg reflectors in optical fibres," *Opt Lett* **3** 66-68.
91. Meltz, G., Morey, W. W., and Glenn, W. H., (1989) "Formation of Bragg gratings in optical fibres by a transverse holographic method," *Opt Lett* **14** 823-825.
92. Armitage, J. R., (1993) "Fibre Bragg reflectors written at 262 nm using a frequency quadrupled diode-pumped Nd³⁺: YLF laser," *Electron Lett* **29** 1181-1183.
93. Zang, Q., Brown, D. A., Reinhart, L., and Morse, T. F., (1994) "Simple prism-based scheme for fabricating Bragg gratings in optical fibres," *Opt Lett* **19** 2030-2032.
94. Garchev, D. D., Vasiliev, M., and Booth, D. J., (1998) "Wavelength tunable chirped in-fibre Bragg gratings produced with a prism interferometer," *Opt Comm* **148** 254-258.
95. Chao, L., Reekie, L., and Ibsen, M., (1999), "Grating writing through fibre coating at 244 and 248 nm," *Electron Lett* **35** 924-926.

96. Lemaire, P. J., Atkins, R. M., Mizrahi, V., and Reed, W. A., (1993) "High pressure H₂ loading as a technique for achieving ultrahigh UV photosensitivity and thermal sensitivity in GeO₂ doped optical fibres," *Electron Lett* **29** 1191-1193.
97. Rao, Y. J., (1997) "In-fibre Bragg grating sensors [Review]," *Measurement Science & Technology* **8** 355-375.
98. Shulian, Z., Lee, S. B., Fang, X., and Choi, S. S., (1999) "In-fibre grating sensors," *Optics & Lasers in Engineering* **32** 405-418.
99. Cole, D. J., and Cebon, D., (1992) "Performance and application of a capacitive strip tyre force sensor," *6th International Conference on Road Traffic Monitoring and Control* pp.123-127, Institution of Electrical Engineers, London.
100. Garner, J. E., Lee, C. E., and Huang, L., (1990) "Infrared sensors for counting, classifying, and weighing vehicles," *Texas Transportation Institute Research Report*. No.1162-1F, VII, 51, Texas Transportation Institute, College Station, TX.
101. Marsh, J. G., and Jewell, R. J., (1994) "Instrumentation for a Weigh In Motion system using pavement strain," *Geological Testing Journal* **17** 497-504.
102. Hajek, J. J., (1994) "Use of weigh-in-motion scale data for safety-related traffic analysis," 73rd annual meeting of the Transportation Research Board, Paper no. 940608, pp.13-18 [6], Transportation Research Board, Washington, DC.
103. Hardy, M. S. A., and Cebon, D., (1994) "Importance of speed and frequency in flexible pavement response," *ASCE J Eng Mech* **130** 463-482.
104. Collop, A. C., and Cebon, D., (1993) "A theoretical analysis of fatigue cracking in flexible pavements," *Cambridge University Engineering Department, CUED/C-MECH/TR Technical Report no 56*, Cambridge, UK.
105. Potter, T. E. C., Collop, A. C. C., Cole, D. J., and Cebon, D., (1994) "A34 Mat tests: results and analysis," *Cambridge University Engineering Department, CUED/C-MECH/TR Technical Report no 61*, Cambridge, UK.

106. Oda, T., (1995) "UTMS demonstration using infrared vehicle detectors," *Proc 28th International Symposium on Automotive Technology and Automation* (Stuttgart, Germany), pp.409-416, Automotive Automation Ltd., Croydon, UK.
107. Oda, T., Takeuchi, K., and Niikura, S., (1996) "Travel time measurement using infrared vehicle detectors," *8th International Conference on Road Traffic Monitoring and Control*, pp.178-182, Institution of Electrical Engineers, London.
108. Garner, J. E., and Lee, C. E., (1995) "Augmented weigh-in-motion system for traffic data collection and analysis," *Transportation Research Record* **1501** 81-86.
109. Koniditsiotis, B. E., (1988) "Evaluation of the Golden River capacitive pad weigh-in-motion system," *14th Proc Australian Road Research Board* **6** 70-85.
110. Cole, D. J., and Cebon, D., (1989) "A capacitive strip sensor for measuring dynamic tyre forces," *2nd International Conference on Road Traffic Monitoring*, pp.38-42, Institution of Electrical Engineers, London.
111. Cunagin, W. D., Majdi, S. O., and Yeom, H. Y., (1991) "Development of low cost piezoelectric film WIM system," *Texas Transportation Institute*, Report No.: TX-93/1220-1F, vi, 30, Texas A&M University System, College Station, TX.
112. Black, T. F., (1992) "Arkansas' experience piezo-electric cable weigh in motion systems in asphalt concrete pavements," *Proc National Traffic Data Acquisition Conference*, pp.155-166, California Dept. of Transportation, Sacramento, CA.
113. Stewart, P. M., (1988) "A low-cost dynamic load sensor: The Pakenham experiment," *Australian Road Research Board*, Internal report no. AIR 407-2, Melbourne, Australia.
114. Cebon, D., and Winkler, C. B., (1991) "Multiple-sensor Weigh-In-Motion: theory and experiments," *Transportation Research Board Record* **131**, *170th Annual Meeting*, January, pp.13-17, Cambridge, UK..
115. Barbour, I. A., and Newton, W. H., (1992) "Improving the accuracy of weigh-in-motion systems," *Transportation Research Laboratory*, *3rd International Symposium on Heavy Vehicle Weights and Dimensions*, pp.381-386, T. Telford, Cambridge, UK.

116. LeBlanc, P. A., and Woodrooffe, J., (1995) "Spatial correlation of dynamic wheel loads," *Proc 7th Int Symp in Heavy Vehicle Weights and Dimensions* **4** 281-290.
117. Streit, D. A., Kulakowski, B. T., and Wollyung, R. J., (1995) "Dynamic vehicle forces on pavements," *Report On Fhwa Contract No. DTFH 61 - 90-C-00084*, Fed. Hwy. Admin., Transp. Res. Board, Washington, DC.
118. Pont, J., and Steven, B., (1998) "Suspension dynamics and pavement wear," *Tranzit NZ ACPTIF research facility Report CAPIF research facility*, Wellington, New Zaland. (Web source: http://www.transit.govt.nz/about_transit/content_files/CAPTIF3_PDFFile.PDF).
119. Hjelmstad, K. D., and Taciroglu, E., (1997) "A coupled hyper elastic constitutive model for resilient response of granular materials," *Proc Aircraft/Pavement Technology: In the Midst of Change*, pp.178-189, ASCE Airfield Pavement Conference in Seattle, Washington DC. (Web source - <http://uiairpave.ce.uiuc.edu/publication/ACoupledHyper.pdf>).
120. Scullion, T., Uzan, J., Nazarian, S., and Briggs, B., (2000) "Future directions in characterising strength and deformation properties of pavement layers," *Transportation Research Board (TRB) Publications Sales & Affiliate Services*, Washington, DC. (Web source -<http://www.nas.edu/trb/publications/millennium/00017.pdf>).
121. Thompson, M. R., (1996) "Mechanistic-empirical flexible pavement design: An overview," *Transp Res Rec 1539*, pp.1-5, Transp Res Board, Washington DC.
122. Green, E. K., and Waicekauskas, J., (1992) "Technical problems related to equipment installation for weigh-in motion systems," *Proc National Traffic Data Acquisition Conference*, pp.517-534, California Dept. of Transportation, Sacramento, CA.
123. Muhs, J. D., Jordan, J. K., Scudiere, M. B., and Tobin Jr., K. W., (1991) "Results of a portable fibre optic weigh-in-motion system," *Proc SPIE* **1584** 374-386.

124. Slavik, M. M., and Visser, A. T., (1990) "Development of weigh-in-motion network in South Africa," *Transp Res Record no. 1272*, Transportation Research Board, Washington DC.
125. Mamlouk, M. S., (1996) "Effect of vehicle-pavement interaction on weigh-in-motion equipment design," *Heavy Vehicle Systems, Int J Vehicle Design* **3** 1-4.
126. Ali, N., Trogdon, J., and Bergan, A. T., (1994) "Evaluation of piezoelectric weigh-in-motion system," *Can J Civ Eng* **21** 156-160.
127. Bernard, A., Jacob. B., and O'Brien, E. J., (1996) "WAVE, a European research project on weigh-in-motion," *Proc National Traffic Data Acquisition Conference (NATDAC'96)*, **2** pp.660-668, New Mexico State Highway and Transportation Dept., Santa Fe, NM.
128. Méndez, A., Morse, T.F., Méndez, F., (1989) "Applications of embedded optical fibre sensors in reinforced concrete buildings and structures," *Proc SPIE* **1170** 60-69.
129. Téral, S., (1992) "Vehicle weigh in motion with fibre optic sensors," *Proc SPIE* **1777** 139-142.
130. Navarrete, M. C., and Bernabeu, E., (1994) "Fibre optic weigh in motion sensor," *Sensors and Actuators* **A41-42** 110-113.
131. Ahmed, S., Jones, G. R., Spindlow, J. R., and Stevens, A., (1991) "Intrinsic optical fibre sensors for axle detection," *Traffic Engineering and Control*, Nov, 527-530.
132. Murphy, K. A., Gunther, M. F., Vengsarkar, and Claus, R. O., (1991) "Quadrature phase-shifted extrinsic Fabry-Perot optical fibre sensors," *Opt Lett* **16** 273-275.
133. Zabaronik, N., Ghoreishian, I., Allison, J., Arya, V., de Vries, M. J., and Claus, R. O., (1997) "Performance of fibre optic vehicle sensors for highway axle detection," *Proc SPIE* **2902** 168-174.
134. Butter, C. D., and Hocker, G. D., (1978) "Fibre optic strain gauge," *Appl Opt* **17** 2867-2869.

135. Keck, D.B., "Fundamentals of optical fibre communications," (1976) *Academic, New York*.
136. Melles Griot, Stabilized He-Ne laser system Operator's manual (models 05 STP 901 and 05 STP 903) p.8.
137. Lee, C. E., Taylor, H. F., Markus, A. M., and Udd, E., (1989) "Optical fibre Fabry-Perot embedded sensor," *Opt Lett* **14** 1225-1227.
138. Seki, Y., and Noda, K. I., (1987) "Linearity stabilized fibre-optic thermometer using pseudo-heterodyne phase detection," *IEEE J Lightwave Technol* **LT-5** 961-966.
139. The Concise Macleod' written by Thin Film Center Inc, Phoenix, AZ.
140. Harding, R. D., "Fourier Series and Transforms," (1985) *Hilger, Bristol, UK*.
141. Inoue, A., Shigehara, M., Ito, M., Inai M., Hattori, Y., and Mizunami, T., (1995) "Fabrication and application of fibre Bragg grating - A review," *Optoelectronics – Devices and Technologies* **10** 119-130.
142. Shigly, J. E., (1977) "McGraw-Hill Series in Mechanical Engineering" 3rd Edition International Student Edition, NY.
143. Young, W. C., (1989) "Roark's Formulas for Stress and Strain," 6th Edition, General Engineering Series, McGraw-Hill International, NY.
144. Téral, S., (1996) "Fibre optic weigh-in-motion sensor: correlation between modeling and practical characterisation," *Proc SPIE* **2718** 417-426.
145. Streit, D. A., Kulakowski, B. T., and Wollyung, R. J. (1995) "Dynamic vehicle forces on pavements," *Report On Fhwa Contract No. DTFH 61 – 90-C-00084*, Fed. Hwy. Admin., Transp. Res. Board, Washington, DC.

146. "Geometric pavement model for computer aided design of pavement maintenance actions," (1999) *Engineering Division, Vägverket*, Publisher: National Road Management Department Vägverket Printing house, Borlänge, Sweden. (Web source - http://www.vv.se/for_lang/english/publications/1999_100e.pdf.)
147. Timm, D.H., Newcomb, D.E., (2003) "Calibration of flexible pavement performance equations for Mn/road," *Transportation Research Board Annual Meeting Report*, TRB Paper #03-2012, Auburn, AL. (Web source - http://www.wsdot.wa.gov/ppsc/research/TRB_Special/TRB2003-000012.pdf.)
148. Olsson, J., Zeng, L., and Wiberg, N.E., (2000) "Finite element analysis of road rutting," *Proc European Congress On Computational Methods In Applied Sciences*, Barcelona, Spain.
149. El Hussein, M., and Nofal, M., (1997) "Structural design of urban roads," *APWA International public works congress NRCC/CPWA seminar series "Innovations in urban structures"* Ottawa, Canada. 135-150. (Web source- <http://irc.nrc-cnrc.gc.ca/fulltext/nrcc42667.pdf>.)
150. Siddharthan, R., Yao, J., and Sebaaly, P., (1998) "Pavement strain from moving dynamic 3D load distribution," *J Transportation Engineering* **124** 557-566.
151. Zafir, Z., Siddharthan, R., and Sebaaly, P., (1994) "Dynamic pavement-strain histories from moving traffic load," *J Traffic Engineering* **120** 821-842.
152. Sousa, J. B., and Monismith, C. L., (1987) "Dynamic response of paving materials," *Transportation Research Record* no.1136, pp.57-68, Trans Res Board, Washington, DC.
153. Mamlouk, M. S., (1997) "General outlook of pavement and vehicle dynamics," *J Transportation Engineering* **123** 515-517.
154. Perry, M., (1995) "Wavelets help resolve uncertainties associated with FFTs," *Personal Engineering, Expert column* 51-53.
155. Hong. C. S., Park, J. W., Ryu, C. Y., and Kang, H. K., (1999) "Signal characterisation of EFPI in the delaminated composites," *Proc SPIE* **3746** 192-195.

156. Lesco, J. J., Carman, G. P., Fogg, B. R., Miller, W. V., Vengsarkar, A. M., Reifsnider, K. L., and Claus, R. O., (1992) "Embedded fibre Fabry-Perot fibre optic strain sensors in the macromodel composites," *Opt Eng* **31** 13-20.
157. Yuan, L., and Zhou L., (1998) "1×N star coupler as a distributed fibre-optic strain sensor in a white-light interferometer," *Appl Opt* **37** 4168-4172.
158. Scott, G., (1987) "Weigh-In-motion technology: status of CULWAY in Australia," *Seminar on Road Traffic Data Acquisition Using Weigh-In-Motion*, Program and Papers, pp.25-45, Australian Road Research Board, Melbourne.
159. Marsh, J. G., and Jewell, R. J., (1994) "Vertical pavement strain as means of weighing vehicles," *J Transportation Engineering* **120** 617-631.

PUBLICATION

1. Surve S, Stevenson A J and Collins S F, 2000. "Intrinsic-fibre optic sensor for dynamic structural sensing". 14th National Congress of the Australian Institute of Physics incorporating the 13th Conference of the Australian Optical Society, Adelaide, Abstracts p. MT9.

LIST OF SYMBOLS

λ	Wavelength.
λ_B	Bragg wavelength.
λ_{UV}	Wavelength of the ultraviolet laser light.
ϕ	Phase.
ϕ_i	The incident angle of the UV radiation on the prism surface.
θ	Writing angle of grating.
Λ	Grating periodicity.
β	Propagation constant.
k_0	Free space propagation constant.
ε	Strain.
ν	Poisson's ratio.
ν_o	Frequency.
ρ	Photoelastic constant.